LBNL-40384
UC-000

ERNEST ORLANDO LAWRENCE
BERKELEY NATIONAL LABORATORY

Spin Polarization and Magnetic Dichroism in Core-Level Photoemission from Ferromagnets

Jose G. Menchero
Materials Sciences Division

May 1997
Ph.D. Thesis

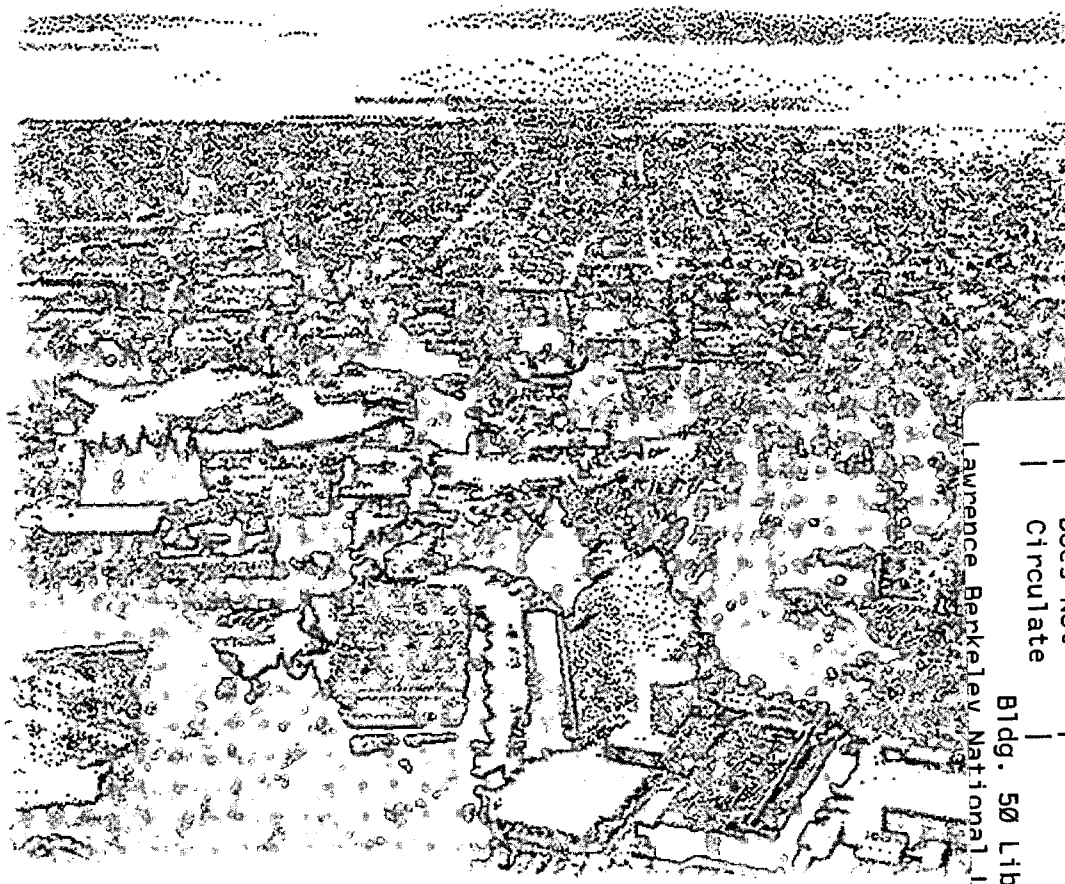

REFERENCE COPY
Does Not
Circulate
Bldg. 50 Library - Ref.
Lawrence Berkeley National Laboratory
LBNL-40384
Copy 1

DISCLAIMER

This document was prepared as an account of work sponsored by the United States Government. While this document is believed to contain correct information, neither the United States Government nor any agency thereof, nor the Regents of the University of California, nor any of their employees, makes any warranty, express or implied, or assumes any legal responsibility for the accuracy, completeness, or usefulness of any information, apparatus, product, or process disclosed, or represents that its use would not infringe privately owned rights. Reference herein to any specific commercial product, process, or service by its trade name, trademark, manufacturer, or otherwise, does not necessarily constitute or imply its endorsement, recommendation, or favoring by the United States Government or any agency thereof, or the Regents of the University of California. The views and opinions of authors expressed herein do not necessarily state or reflect those of the United States Government or any agency thereof or the Regents of the University of California.

LBNL-40384
UC-000

Spin Polarization and Magnetic Dichroism in Core-Level Photoemission from Ferromagnets

Jose Gabriel Menchero

Department of Physics
University of California, Berkeley

and

Materials Sciences Division
Ernest Orlando Lawrence Berkeley National Laboratory
University of California
Berkeley, California 94720

May 1997

This work was supported by the Director, Office of Energy Research, Office of Basic Energy Sciences, Materials Sciences Division, of the U.S. Department of Energy under Contract No. DE-AC03-76SF00098.

LBNL-40384

SPIN POLARIZATION AND MAGNETIC DICHROISM IN CORE-LEVEL PHOTOEMISSION FROM FERROMAGNETS

by

Jose Gabriel Menchero

B.S. (University of Colorado, Boulder) 1986

M.A. (University of California, Berkeley) 1991

A dissertation submitted in partial satisfaction of the

requirements for the degree of

Doctor of Philosophy

in

Physics

in the

GRADUATE DIVISION

of the

UNIVERSITY of CALIFORNIA at BERKELEY

Committee in charge:

Professor Charles S. Fadley, co-chair

Professor Steven G. Louie, co-chair

Professor Paul McEuen

Professor Gabor Somorjai

Spring 1997

Abstract

SPIN POLARIZATION AND MAGNETIC DICHROISM IN CORE-LEVEL PHOTOEMISSION FROM FERROMAGNETS

by

Jose Gabriel Menchero

Doctor of Philosophy in Physics

University of California at Berkeley

Professor Charles S. Fadley, co-chair

Professor Steven G. Louie, co-chair

In this thesis we present a theoretical investigation of angle- and spin-resolved core-level photoemission from ferromagnetic Fe and Ni. We also consider magneto-dichroic effects due to reversal of the photon helicity or reversal of the sample magnetization direction.

In chapter 1, we provide a brief outline of the history of photoemission, and show how it has played an important role in the development of modern physics. We then review the basic elements of the theory of core-level photoemission, and discuss the validity of the some of the commonly-used approximations.

In chapter 2, we present a one-electron theory to calculate spin- and angle-resolved photoemission spectra for an arbitrary photon polarization. The Hamiltonian includes both spin-orbit and exchange interactions. As test cases for the theory, we calculate the spin polarization and magnetic dichroism for the Fe $2p$ core level, and find that agreement with experiment is very good.

In chapter 3 we present a many-body theory based on a small-cluster model to describe and analyze photoemission from the Ni $2p$ core-level. The model treats same-site hole-hole Coulomb interactions and extra-atomic core-hole screening on an equal footing. Theoretical spectra are found to be in excellent agreement with experiment. Also, by considering various limiting cases, we are able to disentangle the effects of spin-orbit, exchange, and extra-atomic screening, and thereby gain considerable insight into the physical problem. In chapter 4, we apply the same model to the Ni $3p$ core level, and again find that the theoretical results agree very favorably with experiment.

In chapter 5 we consider the question of the Ni surface orbital moment. Our findings do not support an earlier analysis that required a large enhancement this moment. Using our model, we are able to explain the experimental observations without invoking such an enhancement.

In chapter 6 we consider photoelectron diffraction effects in photoemission spectra. In particular, we discuss an important new effect in which the magnetic dichroism about a forward-scattering peak is found to exhibit a characteristic chessboard pattern. We provide a simple intuitive explanation of the effect. We also present theoretical results based on a finite-cluster multiple-scattering calculation, and find that they are in excellent agreement with experiment.

In chapter 7, conclusions are given and the prospects for future work are dicussed. We also include an appendix which provides details on utilizing group theory to symmetrize the basis functions and thereby greatly reduce the computational effort.

To my dearest Lisa,

and our little Marina

Acknowledgements

My graduate work was funded in large part by generous support from the National Science Foundation, the Department of Education, and during my final year, by a Dean's Dissertation Writing Fellowship. This support was greatly appreciated. In addition, this thesis would not have been possible without the help of many others.

First of all, I would like to express my deep gratitude to my former advisor, Leo M. Falicov. Leo had a great physical intuition and always gave his students well-posed problems full of interesting physics. The core ideas in this thesis originated with him. Unfortunately, Leo passed away after I had been in his group for two years, and his illness and death were a very difficult period. I will fondly remember our group lunches at the faculty club and the many interesting stories Leo had to tell.

I would also like to express my great appreciation to my current advisor, Chuck Fadley, for taking me on when I was desperately seeking a new advisor. I benefited greatly from his extensive knowledge of both theoretical and experimental photoemission. Through Chuck, I also met Giorgio Rossi and Erhard Kisker, from which two very fruitful collaborations resulted. I also benefited greatly from collaborations with Ajith Kaduwela and Michel Van Hove. Working in Chuck's group was not only a great learning experience, but also a pleasure.

I would also like to thank my old friend Mike Harvanek for his support and encouragement during the difficult period of Leo's illness. Ever since the Boulder days, Mike would always come through in a clutch.

On a lighter note, I thank my good friend Angel Rubio, who not only taught me a good amount of physics, but also served as living proof that one could be a good physicist and have plenty of fun too. His parties will be fondly remembered by all.

I also wish to thank the many other people who helped me along the way. In particular, it was a pleasure to meet Lennie Klebanoff, who measured all of the spin-resolved spectra presented in this thesis. Lennie and I shared many stimulating discussions, and he kindly provided me with his experimental data. Antonio da Silva was very helpful in getting me started in the right direction with my research, and we also had fun following Brazil win the 1994 world cup. Sadi Turgut was also very helpful, and I enjoyed his company those nights I worked late at Birge. At LBL, I benefited greatly from collaborations and discussions with Reinhard Denecke, Jonder Morais, and Ramon Ynzunza. No list would be complete without mention of Anne Takizawa, who was an invaluable help to all the graduate students.

To my mother and father especially I express my deepest gratitude. This day would certainly not have been possible without all of their sacrifices and guidance. My father may also have been responsible for first kindling my interest in science. I will never forget my first telescope, nor the time – armed only with a burning candle and a couple of oranges – that he turned off the lights to demonstrate eclipses to me.

I would also like to thank my mother-in-law Eliko. She sacrificed her lovely apartment in Stockholm and moved to Berkeley, just so that she could be nearby to help with our little Marina. Eliko was a big help and it was fun having her too.

Most of all, I wish to thank my dear wife Lisa for making the final phase of my Ph.D. such a wonderful one. Lisa has been a loving and patient mother and a great support to her family. She always gave me the space I needed to finish my Ph.D., even though she had her own work to do. In addition, she made many excellent suggestions for my work, several of which are contained in this thesis. More than anything, she made the difficult task of writing this dissertation a very happy one.

Contents

Acknowledgements i

1 Introduction 1

1.1 Historical Development 1

1.2 Basic Theory of Core-Level Photoemission 10

1.3 Thesis Overview 14

2 One-Electron Theory of Core-Level Photoemission from Ferromagnets 17

2.1 Introduction 17

2.2 Theory 20

2.3 Results and Discussion 26

2.4 Conclusions 33

3 Many-Body Theory of Ni $2p$ Photoemission 42

3.1 Introduction 42

3.2 Model and Calculation 45

3.3 Results and Discussion 51

4 Many-Body Theory of Ni $3p$ Photoemission 86

4.1 Introduction 86

4.2 Results 88

4.3 Discussion 91

4.4 Conclusions 103

5 On the Enhancement of the Ni Surface Orbital Moment 114

5.1 Introduction 114

5.2 Results 116

6 Photoelectron Diffraction Effects in Magnetic Dichroism 124

6.1 Introduction 124

6.2 Results 126

7 Conclusion 136

7.1 Thesis Summary 136

7.2 Prospects for Future Work 138

A Group Theory: Symmetrization of Basis Functions 140

List of Figures

2.1 Geometric sign convention 37

2.2 Schematic diagram of level positions 38

2.3 Fe $2p$ SRXPS, experiment and theory 39

2.4 Fe $2p$ MUDAD, experiment and theory 40

2.5 MCDAD due to reversal of magnetization and helicity 41

3.1 The small-cluster model 70

3.2 Photoemission geometry 71

3.3 Limiting cases for Ni $2p$ SRXPS 72

3.4 Ni $2p$ SRXPS, experiment and theory 73

3.5 Spin-resolved spectra for RCP excitation 74

3.6 Ni $2p$ MCDAD, theory 75

3.7 Angle-resolved spin polarization 76

3.8 SRXPS in zero bandwidth limit using p-polarized light 77

3.9 SRXPS for Ni metal using p-polarized light 78

3.10 Ni $2p$ MLDAD, theory 79

3.11 Ni $2p$ MUDAD, theory 80

3.12 SRXPS in a chiral geometry for both magnetic orientations 81

3.13 Ni $2p$ spectra for $U_{pd} = 2, 3, 4, 5$ eV 82

3.14 Satellite intensity as function of U_{pd} 83

3.15 Real-space final-state configuration 84

3.16 k-space final-state configuration 85

4.1 Ni $3p$ SRXPS, experiment and theory 106

4.2 Limiting cases for Ni $3p$ SRXPS 107

4.3 Theoretical Ni $3p$ MCDAD, Menchero 108

4.4 Experimental Ni $3p$ MCDAD, van der Laan 109

4.5 Theoretical Ni $3p$ MCDAD, van der Laan 110

4.6 Limiting cases for Ni $3p$ MCDAD 111

4.7 Ni $3p$ satellite intensities 112

4.8 Ni $3p$ final-state configuration 113

5.1 Experimental Ni $3p$ MLDAD 122

5.2 Theoretical Ni $3p$ MLDAD 123

6.1 Photoelectron scattering geometry 132

6.2 Fe $2p$ MUDAD spectra 133

6.3 Angle and energy dependence of Fe $2p$ MUDAD 134

6.4 Theoretical Fe $2p$ MUDAD using 79-atom cluster 135

A.1 Small-cluster sign convention 155

List of Tables

2.1 Dipole Operator Matrix Elements, $\tilde{T}_\epsilon = rY_1^1$. 35

2.2 Dipole Operator Matrix Elements, $\tilde{T}_\epsilon = rY_1^{-1}$. 35

2.3 Dipole Operator Matrix Elements, $\tilde{T}_\epsilon = rY_1^0$. 36

3.1 Ni $2p$ Slater integrals and band energies 69

4.1 Ni $3p$ Slater integrals and band energies 104

4.2 Final states and binding energies, LS limit 104

4.3 Final states and binding energies, including spin orbit 105

A.1 Point-group character table, Group O. 150

A.2 Transformation of sites and coordinates, point-group O 151

A.3 Transformation of basis functions, point-group O 152

A.4 Space-group character table. 153

A.5 Compatibility relations. 153

A.6 Fully-symmetrized one-electron basis functions 154

Chapter 1

Introduction

1.1 Historical Development

The photoelectric effect – also known more recently as photoemission or photoelectron spectroscopy – has played a central role in the development of physics for more than a century [1, 2]. In 1879, the Berlin Academy of Sciences offered a prize "to establish experimentally any relation between electromagnetic forces and the dielectric polarization of insulators." Originally, the question had been posed to confirm Maxwell's theory of electromagnetic waves. In one of the great ironies of science, however, it ultimately led to the particle description of light.

Heinrich Hertz took up the challenge posed by the Berlin Academy of Sciences, and conducted a series of experiments which led, by accident, to the discovery of the photoelectric effect [3]. His apparatus consisted of a primary and a secondary spark-gap circuit, separated by a dielectric medium. A spark in the primary circuit would induce a weak spark in the secondary circuit. The weakness of the secondary spark, however, prompted Hertz to enclose it in a dark chamber to facilitate its observation. The unexpected result was that shielding the secondary circuit from the light dramatically decreased the maximum spark length. By systematically varying the dielectric materials, and performing a series of refraction experiments, Hertz was able to deduce that ultraviolet light from the primary spark was responsible for inducing the spark in the secondary circuit.

Today, of course, we know that what Hertz was observing was the light-induced

emission of electrons. It was not until 1897, however, with the discovery of the electron by J.J. Thomson [4], that the second half of the picture could begin to be understood; within two years of his discovery, Thomson was also able to show that the particles emitted by ultraviolet radiation were indeed electrons.

In a parallel set of experiments, P. Lenard added a few crucial pieces to the puzzle. To carry out his investigations, he built what was perhaps the world's first electron spectrometer. It consisted of a cathode, which was excited by ultraviolet radiation, and an anode with a small aperture, through which photoelectrons would pass. On the other side of the anode was a bending magnet which would deflect the electrons. By analyzing these trajectories, Lenard was able to measure e/m, and thereby independently confirm that the emitted particles were electrons [5]. Furthermore, by applying a voltage across the cathode and anode, he was able to show that there existed a stopping potential above which no electrons could pass: i.e., the photoelectrons possessed a maximum kinetic energy. Moreover, this stopping potential was found to be *independent* of the intensity of the incident light (although the total photocurrent did, of course, depend on it). Lenard's remarkable findings baffled the scientific community of the day: classically, increasing the rate at which electromagnetic energy impinged on the electrons would be expected to increase their kinetic energy as well.

Meanwhile, in a seemingly unrelated development, Max Planck was struggling to interpret experimental data on the spectral distributions of blackbodies. Reluctantly, he made the radical hypothesis that the energies of the modes were quantized. In doing so, he was able to derive an expression, known today as Planck's law, that fit the experimental results. However, this revolutionary step required the introduction of a new fundamental constant, $\hbar$. By fitting Planck's law to the experimental blackbody curves, Planck was able to estimate the value of $\hbar$.

It took a physicist of Einstein's genius to make the connection between the work of

Lenard and the work of Planck. In doing so, Einstein placed the photoelectric effect on a firm theoretical foundation, and for this work was awarded the 1921 Nobel prize in physics. Einstein made the assumption that the energy quantization proposed by Planck also applied to light [6]. These light quanta, called *photons*, deliver all their energy to the electrons when absorbed. If ω is the frequency of the light, the quantum of energy is $\hbar\omega$. Thus, if ϕ is the energy required to remove an electron from the surface (i.e., the work function), then conservation of energy says that the maximum kinetic energy of the photoelectrons is given by $T_{max} = \hbar\omega - \phi$ – a result which immediately explained Lenard's findings. Furthermore, the kinetic energy could be simply related to the stopping potential V_0 via $T_{max} = eV_0$. Therefore, Einstein's theory made the powerful prediction that a plot of V_0 versus ω would yield a straight line with slope $\hbar/e$.

R.A. Millikan, who in his celebrated "oil drop" experiment of 1909 had made the first accurate determination of e, now set about to test Einstein's photoelectric equation. By 1916, careful experiments by Millikan [7] had shown conclusively that V_0 was indeed linear in ω. Furthermore, the value of $\hbar$ obtained from these slopes agreed with that obtained by Planck previously. It was an amazing triumph for theoretical physics that blackbody radiation and the photoelectric effect – two seemingly unrelated phenomena – could be related by Planck's new fundamental constant.

With the development of modern quantum mechanics in the mid 1920s, there were additional advances in the theory of photoemission. For instance, in his theory of metals [8], Sommerfeld was able to relate the work function ϕ to other experimentally measurable quantities such as the thermionic emission current [9] and the contact potential [10]. Another success of this period was the theory of work functions for alkali metals, published in 1935 by Wigner and Bardeen [11]. The alkali metals attracted early theoretical interest due to their nearly free-electron-like nature, which made them tractable problems given the computational methods of the day. These theoretical advances all

dealt with photoemission from the outer or valence electrons.

While progress was thus being made on the theoretical front, the inter-war years proved to be a low point for experimental advances in photoemission. The most notable contributions during these years were made by Maurice de Broglie (brother of Nobel prize winner Louis de Broglie) and H. Robinson, both of whose work involved emission from the inner or core electrons. M. de Broglie, who had discovered the L_3 ($2p_{3/2}$) edge using the technique of *x-ray absorption*, did succeed in measuring several of the K ($1s$) and L ($2s+2p_{1/2}+2p_{3/2}$) photoemission lines for silver and copper [12]. However, he was not able to resolve the L fine structure due to the three levels involved. Disappointed with the poor energy resolution in his photoemission experiments, de Broglie turned his attention back to x-ray absorption and x-ray emission – techniques which, at the time, offered far better energy resolution. Robinson, on the other hand, continued his work on photoemission up until the second world war. He extended measurements to a wide variety of systems, and was able to see lines over a large range of core-level energies. Despite his efforts, however, Robinson was never able to adequately overcome the energy resolution problems, and photoemission as an experimental method fell into a period of inactivity.

Another problem which hindered the development of photoemission, although it was not appreciated for many years, was surface contamination. The escape depth of a typical photoelectron ranges from 5-50 Å, depending on the kinetic energy and the particular material. Therefore, even one monolayer of contaminant can have an adverse effect on the photoemission spectrum. For reactive metals, at a pressure of 10^{-9} torr, this coverage can be achieved in less than one hour. It was not until ultrahigh vacuum technology became commercially available, therefore, that photoemission could emerge as a fully controllable and viable spectroscopy.

By the early 1950s, the prerequisite improvements in vacuum technology had been

secured, and the stage was set for dramatic advances in experimental photoemission. The use of core-level spectra for chemical analysis had been discussed, but with spectra of not much better resolution than Robinson's [13]. The man most responsible for turning x-ray photoelectron spectroscopy (XPS) into a powerful and reliable experimental tool was Kai Siegbahn, professor of physics at the University of Uppsala, Sweden. Siegbahn's initial training was in the area of high-resolution β-ray spectroscopy, and he deftly applied many of these ideas and methods to the field of XPS. After years of extensive experimental development, Siegbahn constructed a magnetic spectrometer that could finally match the resolution of x-ray absorption. The first spectra were measured in 1954, and the sharpness of the lines allowed Siegbahn and his group to make accurate measurements of the core-level binding energies for a large number of elements. In the course of their investigations, they realized that the local chemical environment (e.g., surface atoms versus bulk atoms, local chemical bonds, surface contamination, etc.) could shift the energetic positions of the core levels. Measuring these "chemical shifts" soon became the primary focus of the group, and led to another name for core-level XPS: *Electron Spectroscopy for Chemical Analysis (ESCA)* [14]. Throughout the 1960s, Siegbahn and his group systematically measured these chemical shifts for a wide variety of atomic, molecular, and solid-state systems, and were able to extract an unprecedented wealth of information. In 1965, similar XPS studies were begun in the U.S. by Shirley and co-workers [15]. The success of this work, for which Siegbahn was awarded the Nobel prize in physics, led to a surge of interest in photoelectron spectroscopy.

Ultraviolet photoelectron spectroscopy (UPS), the low-energy counterpart of XPS, also benefitted during this period from advances in instrumentation. For example, electron spectrometers based on electrostatic rather than magnetic principles, and improved photon sources, such as the 21.2 eV helium lamp, both led to increased energy resolution. The most important early applications of UPS to solids were by Spicer and co-workers

at Stanford [16].

Another great experimental advance was the advent of synchrotron radiation in the 1970s. This form of light, produced by accelerating relativistic electrons, is characterized by high brightness and well-defined photon polarization over a wide range of energies (typically ultraviolet to hard x-ray). Synchrotron radiation offers many powerful advantages over conventional photon sources. For instance, the high intensity of the synchrotron beam means that experiments may be performed with unprecedented energy resolution. Furthermore, entire new classes of experiments, such as time-resolved photoemission, are made possible due to the high count rates.

An even more desirable characteristic of synchrotron radiation is the continuous distribution of photon energies; whereas a conventional photon source (e.g., x-ray lamp) is capable of only certain discrete excitation energies, a synchrotron source is *tunable*. Since the photoelectron escape depth depends on the kinetic energy, varying the incident photon energy is equivalent to sampling at different penetration depths. In this way, the photon energy can be tuned to act either as a surface-sensitive probe or as a bulk-sensitive probe. Another example which deserves special mention is the case of resonant photoemission. In 1977, a group at the Orsay synchrotron source reported that, as the photon energy exciting the $3d$ valence bands of Ni passed through the threshold of exciting the Ni $3p$ core level, a resonant enhancement of the 6-eV valence satellite occurred [17]. This measurement, which would not have been possible without synchrotron radiation, proved the two-hole nature of the satellite and the inherently many-electron nature of such resonances, and also gave birth to the new field of resonant photoemission.

Another extremely important application of synchrotron radiation is in the determination of electronic band structure. Knowledge of the electron dispersion relations, in principle, allows one to derive many other experimentally measurable quantitities (e.g., optical properties, transport properties, etc.). Although band structures have been cal-

culated since the 1930s, it was not until the 1970s that experimentalists were able to measure them. This requires angle-resolved photoelectron spectroscopy (ARPES) in order to extract the k-dependence of the initial state. As first demonstrated by Smith [18], the k conservation law involved requires that the component of k parallel to the surface is conserved, but not the perpendicular component. By varying the polar angle of emission, one can scan this parallel component. By properly tuning the photon energy, one can also scan the component of the wavevector normal to the surface and thereby map out the complete bulk band structure.

When used in conjunction with spin detection, this method (known as spin-polarized ARPES, or SPARPES) can be used to map out the band structures of ferromagnetic systems. In a ferromagnet, the spin degeneracy is broken, and the energy dispersion curves split into majority and minority bands. In 1985, Kisker *et al.* [19] used this technique to measure the exchange splitting (i.e., the energy separation between peak positions of the majority and minority bands) of the valence band in ferromagnetic Fe. Furthermore, by performing the experiment at different temperatures, they obtained important insight into the nature of the ferromagnetic-to-paramagnetic phase transition.

The polarization of the photon beam is another aspect of synchrotron radiation that is extremely useful for magnetism studies. In the orbital plane, the light is linearly polarized, but it acquires a large degree of circular polarization above or below the plane. This property of the light can be exploited in core-level photoemission studies via the technique of *magnetic dichroism.* The photon polarization, which acts *directly* only on the electron orbital wavefunction (characterized by quantum numbers l and m_l), can couple *indirectly* to the electron spin (characterized by quantum numbers $m_s = \pm\frac{1}{2}$) via core-level spin-orbit interaction. The spin of the core electron, in turn, couples to the spin of the valence electrons through the intra-atomic exchange interaction, leading to what can be very large ($\sim$ several eV) multiplet splittings in core-level spectra from

magnetic atoms [20]. In this way, the light is indirectly coupled to the spin-polarized valence band. As a result, the core-level photoemission spectrum depends on the relative orientation between the photon polarization vector and the sample magnetization. The first study to utilize synchrotron radiation as a magnetic probe in a core-level photoemission experiment was performed by Baumgarten *et al.* [21] in 1990 . They used circularly polarized light to estimate the exchange splitting of the Fe $2p$ core electrons, and their success has prompted a flurry of activity in magnetic dichroism. For instance, it was soon realized that, in an angle-resolved photoemission experiment with the proper geometry, magnetic properties and exchange splittings could also be measured with linearly polarized excitation. In 1993, Roth *et al.* [22] used this approach to probe the magnetic structure of the higher-lying Fe $3p$ core level. Even more remarkable was the discovery by Hillebrecht *et al.* of magnetic dichroism in photoemission with the sort of *unpolarized* radiation available in a typical laboratory XPS system [23]. This result has opened the possibility of also using conventional x-ray sources as a probe of magnetic materials.

An alternative approach, which can be carried out with either synchrotron radiation or conventional x-ray sources, is to directly measure the spin of the outgoing photoelectron. Due to extremely low signals, spin-resolved measurements typically require an additional four orders of magnitude in data acquisition time, as compared to conventional measurements. Given the relatively low photon fluxes of prior-generation synchrotron radiation sources and conventional x-ray sources, and the weak signals inherent in spin-resolution, initially it was not even clear that the spin polarization of the core levels could be experimentally resolved. By now, however, such measurements have been successfully carried out in both shallow core levels [24] and deep core levels [25, 26, 27]. The first such studies on the deep core levels of the itinerant ferromagnets were carried out beginning in 1993 by the Klebanoff group at Lehigh University. They

used a conventional source and measured the spin-resolved core-level spectra for Fe [25], Co [26], and Ni [27] with sufficient resolution to reveal a rich and fascinating structure. This work demonstrated conclusively that spin-polarized core-level photoemission was a viable probe of magnetic systems.

Photoelectron diffraction is another area of photoemission that has led to important advances in surface physics and magnetism [28]. The basic idea is that an outgoing core photoelectron will scatter off other atoms on the way out, and that these scattered waves will interfere with the primary wave. In a single-crystal sample, such diffraction will give rise to intensity modulations. The two basic ways for measuring these modulations are to either vary the photoelectron takeoff direction (scanned angle method), or to vary the incident photon energy (scanned energy method).

By now it is well understood that for high kinetic energies (above several hundred eV), the scattered intensity is strongly peaked in the forward direction. This feature can be exploited, for example, to deduce the orientations of adsorbed molecules on surfaces [29], or to characterize epitaxial overlayers [30].

Imaging of atomic positions via holographic inversion of photoelectron diffraction patterns is another promising development in photoemission studies. Barton [31], pursuing a suggestion first made by Szöke [32], was the first to demonstrate that, in principle, diffraction data could be used to deduce atomic positions relative to the emitter. Theoretical studies suggest that this method can also be extended to study short-range magnetic order [33].

Photoelectron diffraction has also been found to have important consequences in the analyis and interpretation of magnetic dichrosim experiments. Until now, most theoretical work on magnetic dichroism has completely neglected diffraction effects. Very recently, however, Fanelsa *et al.* [34] conducted an experiment which directly probed such effects. They discovered that photoelectron diffraction can indeed be the

dominant effect, and must be taken into account in any theoretical analysis of data from single-crystal samples.

1.2 Basic Theory of Core-Level Photoemission

In a typical photoemission experiment, light of a definite energy and polarization impinges upon a sample, exciting the electrons into free electron states far above the Fermi level. The kinetic energy, wavevector, and perhaps also the spin of these photoelectrons are then measured. Our objective here is to outline how such an angle- and spin-resolved spectrum can be calculated, and to briefly discuss some of the assumptions that are commonly employed.

The effect of the electromagnetic radiation is to induce a perturbation Hamiltonian,

$$H' = \frac{e}{2mc}(\vec{p}\cdot\vec{A} + \vec{A}\cdot\vec{p}) \ , \tag{1.1}$$

where $\vec{p} = -i\hbar\vec{\nabla}$ and $\vec{A} = \vec{A}(\vec{r},t)$ is the vector potential. It is always possible to choose a gauge such that $\vec{\nabla}\cdot\vec{A} = 0$, in which case $[\vec{p},\vec{A}] = 0$, so that H' reduces to

$$H' = \frac{e}{mc}\vec{A}\cdot\vec{p} \ . \tag{1.2}$$

We assume that the vector potential can be written in the following form

$$\vec{A}(\vec{r},t) = \hat{\epsilon}A_0 \exp[i(\vec{q}\cdot\vec{r} - \omega t)] \ , \tag{1.3}$$

which gives

$$H' = \frac{e}{mc}A_0 \exp[i(\vec{q}\cdot\vec{r} - \omega t)]\hat{\epsilon}\cdot\vec{p} \ . \tag{1.4}$$

The transition rate $R_{i\to f}$ (i.e., photoemission intensity) between the initial state $|\Psi_i\rangle$ which contains the core electron, and the final state $|\Psi_f(\vec{k})\rangle$ which contains a core hole and an outgoing photoelectron with wavevector $\vec{k}$ is now calculated from time-dependent perturbation theory via Fermi's golden rule:

$$R_{i\to f} = \frac{2\pi}{\hbar}|M_{if}|^2\rho(E) \ , \tag{1.5}$$

where $\rho(E) \propto E^{1/2}$ is the photoelectron density of states at energy E and

$$\begin{aligned} |M_{if}|^2 &= |\langle \Psi_f(\vec{k})|\vec{A}\cdot\vec{p}|\Psi_i\rangle|^2 \\ &= \hbar^2 A_0^2 |\langle \Psi_f(\vec{k})|\exp(i\vec{q}\cdot\vec{r})\hat{\epsilon}\cdot\vec{\nabla}|\Psi_i\rangle|^2 \ . \end{aligned} \tag{1.6}$$

At this point one usually makes the electric dipole approximation. That is, we approximate $\exp(i\vec{q}\cdot\vec{r}) \approx 1$. This is equivalent to saying that the wavelength of the light is much larger than the spatial extent of the core wavefunction. The wavelength of a 2 KeV x-ray is ~ 6Å, whereas the spatial extent of a highly localized core electron is ~ 0.5Å. Therefore, the electric dipole approximation remains a very good one well into the soft x-ray regime.

By utilizing the dipole approximation and the commutation relations, the matrix elements M_{if} of Eq. (1.6) can be rewritten as

$$M_{if} = C\langle \Psi_f(\vec{k})|\hat{\epsilon}\cdot\vec{r}|\Psi_i\rangle \ , \tag{1.7}$$

where C is a product of fundamental constants and A_0. If the core electron is characterized by orbital quantum numbers l and m_l and spin m_s, and the photoelectron by l^f, m_l^f, and m_s^f, then the dipole selection rules require that

$$\begin{aligned} \Delta l &= l^f - l = \pm 1 \\ \Delta m_l &= m_l^f - m_l = 0,\ \pm 1 \\ \Delta m_s &= m_s^f - m_s = 0 \ . \end{aligned} \tag{1.8}$$

This gives rise to two photoemission channels: $l+1$ and $l-1$. In subsequent chapters, we will investigate important effects that result from interference between these two channels.

The initial state $|\Psi_i\rangle$ is given by the ground state of the N-electron system prior to excitation. For weakly correlated systems, $|\Psi_i\rangle$ may be written as a single-particle

wavefunction corresponding to the core electron. More generally, however, the many-body nature of $|\Psi_i\rangle$ must be included, for example, by using a configuration interaction (CI) approach and writing it as a linear combination of Slater determinants.

The final state $|\Psi_f(\vec{k})\rangle$, which contains a core hole and an outgoing photoelectron with wavevector $\vec{k}$ must also, in general, be described by an N-electron many-body wavefunction. Usually, the coupling between the photoelectron and the $(N-1)$-electron state left behind is considered negligible. Therefore, $|\Psi_f(\vec{k})\rangle$ consists of two parts, and can be written formally as

$$|\Psi_f(\vec{k})\rangle = |\Psi_f^+(N-1); \phi_f(\vec{k})\rangle \ . \tag{1.9}$$

Here, $|\Psi_f^+(N-1)\rangle$ is a many-body eigenstate of the system in the presence of a core hole, and $|\phi_f(\vec{k})\rangle$ is the one-electron wavefunction for the outgoing photoelectron. Thus, the wavefunction $|\Psi_f(\vec{k})\rangle$ contains much interesting physics. This gives rise to phenomena that are appropriately called "final-state effects", and of which we may distinguish between two distinct types, one involving $|\Psi_f^+(N-1)\rangle$ and the other involving $|\phi_f(\vec{k})\rangle$.

The first type of final-state effect is strictly of a many-body nature and is the result of the many-electron response to the sudden creation of a core hole. Upon photoemission, the valence electrons feel the attractive potential of the core hole and rush in to screen it. The energy of the final state then depends on the Coulomb interaction energy between the core hole and the valence electrons. Energy conservation therefore implies that the spectral density does not occur as a single sharp peak, but rather is distributed in energy. This is the origin of multiplet splittings and satellite structures in photoemission spectra. Also, because the energy depends on the spin orientation of the core hole due to exchange, the satellite structures can have a large spin polarization. The strength of the satellite peaks is determined by the many-body overlap integral between the $(N-1)$ electrons in the ground state $|\Psi_i\rangle$ excluding the core hole involved in the photoemission,

and the orbitals in the $(N-1)$ final state $|\Psi_f^+(N-1)\rangle$.

To calculate this overlap integral, one typically employs the sudden approximation. This is equivalent to saying that the ground state charge density does not change much within the time it takes for the photoelectron to escape. We now estimate the validity of the sudden approximation. Let t_1 be the characteristic time for the valence electrons to rearrange. Then $t_1 \sim \frac{\hbar}{\tau}$, where τ is the valence bandwidth. Let t_2 be the time required for the photoelectron to escape. Thus, $t_2 \sim \frac{d}{v}$, where d is the size of the atom and v is the speed of the photoelectron. For the sudden approximation to be valid requires that $t_1 >> t_2$, or $v >> \frac{\tau d}{\hbar}$. Typically, $\tau \sim 5$ eV and $d \sim 2$ Å, so that we require $v >> .01c$. This indicates that the sudden approximation is valid for photoelectrons with kinetic energy above several tens of eV, as is the case for all systems treated here.

The second type of final-state effect is due to the photoelectron scattering off of the lattice on the way out of the crystal, and may be treated within the one-electron approximation. The scattered waves can interfere constructively or destructively with the direct (unscattered) wave, thus producing intensity modulations in energy and/or angle. The scattered waves, in principle, can themselves be scattered off the lattice, thereby leading to a multiple scattering description. The basic effect, however, can be understood within the single scattering approach.

Let $|\phi_0(\vec{k})\rangle$ be the direct or unscattered photoelectron wave in the direction $\vec{k}$. Let $|\phi_j(\vec{k})\rangle$ be the singly-scattered wave with wavevector $\vec{k}$ that results from scattering of the direct wave $|\phi_0\rangle$ from an atom j. The total wavefunction, which is just the superposition of the direct wave plus all singly-scattered waves, can be written

$$|\phi_f(\vec{k})\rangle = |\phi_0(\vec{k})\rangle + \sum_j |\phi_j(\vec{k})\rangle \ . \tag{1.10}$$

The scattering process that gives rise to the $|\phi_j(\vec{k})\rangle$ can be described most simply

by means of the complex plane-wave scattering factor

$$f(\theta) = |f(\theta)| \exp[i\delta(\theta)] \ , \tag{1.11}$$

where $|f(\theta)|$ gives the magnitude of the scattered wave, $\delta(\theta)$ gives the scattering phase shift, and θ is the scattering angle. The simplest way to calculate $f(\theta)$ is to assume an incident plane wave and then use the partial-wave phase shifts δ_l,

$$f(\theta) = \frac{1}{k} \sum_{l=0}^{\infty} (2l+1) e^{i\delta_l} \sin(\delta_l) P_l(\cos\theta) \ , \tag{1.12}$$

where k is the magnitude of the photoelectron wavevector and P_l is the Legendre polynomial [35]. For large kinetic energies, above say a few hundred eV, the function $|f(\theta)|$ becomes strongly peaked around $\theta \approx 0$, so that the forward scattering is strongly enhanced.

The complex plane-wave approach to the scattering process implicitly assumes that the curvature of the scattering wave is sufficiently small compared to the dimensions of the scattering potential. A more realistic treatment should take into account the spherical nature of the outgoing waves, and all of the calculations reported in this thesis have made use of this more accurate approach. Comparisons between the plane-wave scattering and the more accurate spherical-wave scattering can be found in the literature [36].

1.3 Thesis Overview

In this thesis, we present a theoretical investigation of core-level photoemission from ferromagnetic Fe and Ni. The inspiration and experimental basis for this work lies in the spin-resolved studies of Klebanoff. Good results are obtained for Fe within a phenomenological one-electron theory. The primary theoretical effort, however, is aimed at Ni. Due to its pronounced satellite structures, Ni is a particularly intriguing system to

examine, and requires an accurate many-body approach. Emphasis is placed on understanding and disentangling the subtle and competing effects of spin-orbit interaction, extra-atomic screening, and many-body exchange and correlation. The effects of photon polarization and spin resolution are also investigated. Although ferromagnetic Co is not explicitly considered, the data suggest [26] that Co may be treated in a way analogous to Fe.

In Chapter 2, we present a one-electron theory which describes angle-resolved photoemission from a core level in the presence of spin-orbit and exchange interaction. The theory is applied to the case of Fe $2p$, and the resulting spectra agree well with both experimental spin-resolved measurements as well as magnetic dichroism studies. However, this one-electron approach is not adequate for describing Ni due to strong many-body interactions.

In Chapter 3 we present a theoretical model to describe photoemission from ferromagnetic Ni. Theoretical spin-resolved spectra are calculated for Ni $2p$ and found to be in excellent agreement with experiment. Magnetic dichroism due to circular- and linear-polarized excitation is also discussed. In this chapter, we also carry out the first quantitative investigation of the nature of the final state, and the various peaks in the spectrum are assigned physical meaning. As an appendix to Chapter 3, we discuss the group-theoretical analysis employed in diagonalizing the Hamiltonian.

In Chapter 4 we present theoretical spin-resolved spectra for photoemission from the Ni $3p$ core level, and these results also agree very well with experiment. In addition, we present spectra for magnetic dichroism with circular-polarized excitation. Again, we provide the first quantitative analysis of the Ni $3p$ final state, and physically interpret all features of the spectrum. Moreover, by considering a simple 2x2 model, we derive an analytic expression for the satellite intensity. This analysis provides important insight into the question of spectral weight transfer.

In Chapter 5 we treat the case of magnetic dichroism from Ni $3p$ using linear-polarized excitation, and the theoretical results agree very favorably with experiment. This case merits special attention because it represents the best experimental data available for Ni magnetic dichroism, and because it relates to the controversy regarding the Ni surface orbital magnetic moment.

In Chapter 6 we describe the recent magnetic dichroism experiment by Fanelsa *et al.* [34] which proved the importance of photoelectron diffraction in the analysis of such data. We also present theoretical simulations based on a multiple-scattering finite-cluster approach. The calculated results are found to be in very good agreement with experiment. Finally, we use a simple physical argument to derive an analytic expression for the observed dichroism.

In Chapter 7, conclusions and prospects for future work are given.

Chapter 2

One-Electron Theory of Core-Level Photoemission from Ferromagnets

2.1 Introduction

In recent years there has been great interest in utilizing core-level photoelectron spectroscopy to probe the local electronic and magnetic structure of the itinerant ferromagnets. In the shallow $3p$ core levels, the spin-orbit and exchange interaction are roughly equal in magnitude, leading to heavy hybridization between the $3p_{3/2}$ and $3p_{1/2}$ lines. This is in contrast to the deep $2p$ core levels, where the spin-orbit interaction is much larger than the exchange interaction. As a consequence, the $2p_{3/2}$ and $2p_{1/2}$ main lines are well separated in energy, and experience little mixing. These characteristics help simplify the spectroscopic interpretation, and therefore make the $2p$ core levels particularly instructive to examine.

One approach to using photoemission as a probe of magnetic systems is to directly measure the spin of the outgoing photoelectron, a method known as spin-resolved x-ray photoelectron spectroscopy (SRXPS). Due to the Pauli principle and the resulting exchange interaction, core electrons with spin parallel to the majority in the valence band will have their binding energy increased relative to electrons with spin anti-parallel. This effect appears as a shift in spectral weight to higher binding energy for the majority photoelectrons. Spin-resolved studies have by now been carried out on the ferromagnetic transition metals for both the shallow core levels [24] as well as the deep core levels [25, 26, 27]. The core-level spectra for Ni exhibit prominent satellite structures with

complex spin polarizations, a proper description of which requires an accurate many-body approach [37, 38, 39]. Core-level spectra of Fe and Co, on the other hand, do not exhibit such pronounced satellite structures, and one-electron theories have been used with success to describe these systems [40, 41].

An alternative to SRXPS – which does not require photoelectron spin resolution – is magnetic dichroism. The first observation of magnetic dichroism in core-level photoemission was by Baumgarten *et al.*, who performed angle-resolved measurements using circularly polarized light – a technique known as magnetic circular dichroism in the angular distribution, or MCDAD – to deduce an effective exchange splitting of the Fe $2p$ main lines [21]. In MCDAD studies, two distinct methods of measurement have been employed: fixing the magnetization and reversing the photon helicity, or fixing the photon helicity and reversing the magnetization. If linear-polarized excitation is used, then dichroism can only be observed by reversal of the magnetization, and Hillebrecht *et al.* used this approach to probe the Fe $2p$ core level [42]. This method also requires angular resolution of photoelectrons, and is therefore known as magnetic linear dichroism in the angular distributions, or MLDAD. It is possible to observe dichroism even with unpolarized light, an effect which can be termed MUDAD, and such studies have been carried out for several itinerant ferromagnetic systems [23, 34, 43].

In this chapter we present a one-electron theory to describe angle- and spin-resolved photoemission from a core level under the spin-orbit and exchange interactions. We do not include final-state photoelectron scattering and diffraction effects, although these are by now recognized to be important when studying single-crystal samples in certain geometries [34]. Our formulation treats an oriented atom for which the only effect of the magnetic solid is to induce an exchange splitting of the different sublevels, and it allows in a simple way to treat a general photon incidence direction and polarization. Cherepkov has also used a similar model to theoretically describe angle-resolved photoemission

from oriented atoms [44, 45]. He calculates the photoemission intensity in terms of the partial photoionization cross section, the state multipoles, and a somewhat complicated set of terms that describe the coupling of the various angular momenta. Cherepkov's formalism, though quite powerful and general, has the disadvantage of being rather difficult to interpret in an intuitive way. In our approach, the only parameters that enter have an immediate and obvious physical meaning (e.g., photoelectron takeoff angle, photon polarization, spin-orbit and exchange strengths, etc.). We believe, therefore, that the present formulation is more transparent, and may be useful for workers in need of a more straightforward method of calculating spin polarization and magnetic dichroism in photoemission from a p core level. Another important difference between our approach and Cherepkov's is that we allow for mixing between the $j = l+1/2$ and $j = l-1/2$ levels by explicitly including the exchange interaction in our Hamiltonian. Such an approach is necessary to correctly describe the spin-resolved transfer of spectral weight across the levels. In other words, Cherepkov assumes that jm_j are good quantum numbers for the core hole, whereas in our model only m_j is a good quantum number.

As examples, we apply our theory to Fe $2p$ SRXPS and MUDAD experimental spectra. The theory correctly reproduces the main features of the spectra, although it does not account for some details. We attribute these discrepancies to many-body effects not describable within the one-electron model considered here. In particular, we show that the experimental results indicate the existence of weak satellite structures in Fe $2p$ photoemission spectra. Finally, we discuss an example which illustrates the differences between the magnetic dichroism arising from reversal of magnetization with that arising from reversal of photon helicity.

2.2 Theory

The electric dipole operator is defined as

$$T_\epsilon = \vec{r} \cdot \vec{\epsilon} = x\epsilon_x + y\epsilon_y + z\epsilon_z \ , \tag{2.1}$$

where $\vec{r}$ is the electron coordinate vector,

$$\vec{r} = r\hat{r} = r\left[\left(\frac{x}{r}\right)\hat{e}_x + \left(\frac{y}{r}\right)\hat{e}_y + \left(\frac{z}{r}\right)\hat{e}_z\right], \tag{2.2}$$

and $\vec{\epsilon}$ is the electric field polarization

$$\vec{\epsilon} = \epsilon_x\hat{e}_x + \epsilon_y\hat{e}_y + \epsilon_z\hat{e}_z. \tag{2.3}$$

To describe the most general photon polarization, the expansion coefficients ϵ_i must be complex. Using the usual relations for the spherical harmonics,

$$\frac{x}{r} = \sqrt{\frac{4\pi}{3}}\left(\frac{Y_1^{-1} - Y_1^1}{\sqrt{2}}\right), \qquad \frac{y}{r} = i\sqrt{\frac{4\pi}{3}}\left(\frac{Y_1^1 + Y_1^{-1}}{\sqrt{2}}\right), \qquad \frac{z}{r} = \sqrt{\frac{4\pi}{3}}Y_1^0, \tag{2.4}$$

we can rewrite the electron coordinate unit vector as

$$\hat{r} = \sqrt{\frac{4\pi}{3}}\left[\left(\frac{Y_1^{-1} - Y_1^1}{\sqrt{2}}\right)\hat{e}_x + i\left(\frac{Y_1^1 + Y_1^{-1}}{\sqrt{2}}\right)\hat{e}_y + Y_1^0\hat{e}_z\right] \tag{2.5}$$

$$= \sqrt{\frac{4\pi}{3}}\left(Y_1^{-1}\hat{e}_+ - Y_1^1\hat{e}_- + Y_1^0\hat{e}_z\right) \ , \tag{2.6}$$

where we have introduced the circular-polarized basis vectors

$$\hat{e}_+ = \frac{\hat{e}_x + i\hat{e}_y}{\sqrt{2}}, \qquad \hat{e}_- = \frac{\hat{e}_x - i\hat{e}_y}{\sqrt{2}}. \tag{2.7}$$

In terms of this new basis, the photon polarization vector can be rewritten

$$\vec{\epsilon} = \epsilon_+ \hat{e}_+ + \epsilon_- \hat{e}_- + \epsilon_z \hat{e}_z, \tag{2.8}$$

where

$$\epsilon_+ = \frac{\epsilon_x - i\epsilon_y}{\sqrt{2}}, \qquad \epsilon_- = \frac{\epsilon_x + i\epsilon_y}{\sqrt{2}}. \tag{2.9}$$

The dipole operator is then given by:

$$T_\epsilon = \vec{r} \cdot \vec{\epsilon} = r\sqrt{\frac{4\pi}{3}} \left(-Y_1^1 \epsilon_+ + Y_1^{-1} \epsilon_- + Y_1^0 \epsilon_z \right) \quad . \tag{2.10}$$

This is a convenient basis for circular-polarized light propagating in the z direction, or for z-polarized light propagating along an arbitrary direction in the xy plane. However, such an expression is not immediately useful for a general polarization and geometry, as depicted schematically in Fig. 2.1 for an oriented atom. Here, $\mathbf{k}$ is the photoelectron wavevector, and $\mathbf{q}$ is the photon wavevector. We now proceed to generalize our development for this geometry.

The dipole operator as written in Eq. (2.10) is defined by six real (three complex) numbers. One of these can be related to an overall phase factor, and another can be related to a normalization condition, neither of which are important for present purposes. This leaves four remaining independent numbers to define the polarization. Due to the transverse nature of the electric field, two of these are defined by the photon propagation direction, which is given in Fig. 2.1 by (θ_q, ϕ_q). The other two are defined by the relative magnitude and phase difference between the two orthogonal components of the electric field. For a normalized polarization vector $\hat{\epsilon}$, this can be written in spherical coordinates in terms of two angles α and δ as

$$\hat{\epsilon} = \cos\alpha \hat{e}_\theta + \sin\alpha e^{i\delta} \hat{e}_\phi \quad . \tag{2.11}$$

For Eq. (2.10) to be useful for a general photon polarization and propagation direction,

we need to express the polarization coefficients ϵ_+, ϵ_-, and ϵ_z in terms of the four new parameters θ_q, ϕ_q, α, and δ. For a general propagation direction, the normalized dipole operator is

$$\vec{r}\cdot\hat{\epsilon} = r\sqrt{\frac{4\pi}{3}}\left(Y_1^{-1}\hat{e}_+ - Y_1^1\hat{e}_- + Y_1^0\hat{e}_z\right)\cdot\left(\cos\alpha\hat{e}_\theta + \sin\alpha e^{i\delta}\hat{e}_\phi\right) , \tag{2.12}$$

where

$$\begin{aligned} \hat{e}_\theta &= \cos\theta_q\cos\phi_q\hat{e}_x + \cos\theta_q\sin\phi_q\hat{e}_y - \sin\theta_q\hat{e}_z, \\ \hat{e}_\phi &= -\sin\phi_q\hat{e}_x + \cos\phi_q\hat{e}_y . \end{aligned} \tag{2.13}$$

Now using

$$(\hat{e}_\pm)^*\cdot\hat{e}_\theta = \frac{e^{\mp i\phi_q}}{\sqrt{2}}\cos\theta_q, \qquad (\hat{e}_\pm)^*\cdot\hat{e}_\phi = \frac{\mp ie^{\mp i\phi_q}}{\sqrt{2}} , \tag{2.14}$$

we obtain the desired result:

$$\begin{aligned} \epsilon_+ &= \frac{e^{-i\phi_q}}{\sqrt{2}}\left[\cos\alpha\cos\theta_q - i\sin\alpha e^{i\delta}\right] , \\ \epsilon_- &= \frac{e^{i\phi_q}}{\sqrt{2}}\left[\cos\alpha\cos\theta_q + i\sin\alpha e^{i\delta}\right] , \\ \epsilon_z &= -\cos\alpha\sin\theta_q. \end{aligned} \tag{2.15}$$

To illustrate the use of these relations, consider right circularly polarized (RCP) light propagating along the $+z$ direction, so that $\theta_q = 0°$. We here define RCP light to have positive helicity, which means that $\alpha = 45°$ and $\delta = 90°$, and therefore we arrive at $|\epsilon_+| = 1$. From Eq. (2.10), we see this corresponds to $T_\epsilon \sim Y_1^1$, i.e., the photon angular momentum is parallel to the wavevector $\mathbf{q}$. As another example, let $\theta_q = 90°$

and $\phi_q = 0°$, so that the photon is propagating along the $+x$ direction (see Fig. 2.1). Suppose $\alpha = 90°$ and $\delta = 0°$, so that $\hat{\epsilon} = \hat{e}_\phi = \hat{e}_y$. Then Eq. (2.15) gives $\epsilon_+ = -i/\sqrt{2}$ and $\epsilon_- = i/\sqrt{2}$, so that we recover $T_\epsilon \sim i(Y_1^1 + Y_1^{-1}) \sim y$.

The α and δ defined here can also be related to the very commonly used Stokes parameters [46] by

$$\begin{aligned} s_1 &= \cos 2\alpha \\ s_2 &= \sin 2\alpha \cos \delta \\ s_3 &= \sin 2\alpha \sin \delta \ , \end{aligned} \tag{2.16}$$

which gives $s_0 = \sqrt{s_1^2 + s_2^2 + s_3^2} = 1$. For a surface normal given by $\hat{n} = \hat{z}$, s_1 gives the preponderance of p-linear polarization ($\hat{\epsilon} = \hat{e}_\theta$) over s-linear polarization ($\hat{\epsilon} = \hat{e}_\phi$), with $s_1 = +1$ corresponding to p-polarization and $s_1 = -1$ corresponding to s-polarization. The Stokes parameter s_3 gives the preponderance of RCP over LCP light, with $s_3 = +1$ corresponding to RCP, and $s_3 = -1$ corresponding to LCP.

Let $|\Psi_{k\sigma}\rangle$ be the wavefunction for the outgoing photoelectron with wavevector $\mathbf{k}$ and spin σ, and let $|\Psi_{core}\rangle$ be the wave function for the core electron in the initial state. The intensity is then given by

$$I_{k\sigma}^{\epsilon} = |\langle \Psi_{k\sigma} | T_\epsilon | \Psi_{core} \rangle|^2 \, \delta(E_B + E_k - \hbar\omega) \ , \tag{2.17}$$

where E_B is the binding energy of the core electron, E_k is the kinetic energy of the photoelectron, and $\hbar\omega$ is the photon energy.

The final state, for emission into a general direction $\mathbf{k}$, is given by a superposition of spherical waves [47],

$$\Psi_{k\sigma}(r,\theta,\phi) = 4\pi \sum_{lm} i^l e^{-i\delta_l} Y^*_{lm}(\theta_k,\phi_k) Y_{lm}(\theta,\phi) f_{kl}(r)\sigma \ , \tag{2.18}$$

where δ_l are the partial wave phase shifts, and $f_{kl}(r)$ are the radial wavefunctions at kinetic energy $E_k = \hbar^2 k^2/2m$. The special case of a plane wave is recovered by setting all $\delta_l = 0$ and $f_{kl}(r) = j_l(kr)$, where $j_l(kr)$ is the spherical Bessel function of order l. In this work, we do not consider photoelectron diffraction effects in the final-state wavefunction, which would modify $\Psi_{k\sigma}$ further by scattering from neighboring atoms.

The initial state Ψ_{core} is given by

$$|\Psi_{core}\rangle = |f_{nl}(r);\ \Phi_\sigma(\theta,\phi)\rangle \ , \tag{2.19}$$

where $f_{nl}(r)$ is the radial wavefunction and $\Phi_\sigma(\theta,\phi)$ is the part depending on angle and spin. To determine $\Phi_\sigma(\theta,\phi)$, we follow the approach discussed by van der Laan [48]. We include the spin-orbit interaction and treat the exchange interaction by means of a spin field. The Hamiltonian is therefore given by

$$H = \lambda \vec{l}\cdot\vec{s} + \xi s_z \ . \tag{2.20}$$

As our basis states, we choose the $|j,\ m_j\rangle$ spin-orbit states, which can be constructed directly from the Clebsch-Gordan coefficients:

$$\begin{aligned}
|3/2 \quad 3/2\rangle &= |Y_1^1 \uparrow\rangle \\
|3/2 \quad 1/2\rangle &= \sqrt{2/3}\,|Y_1^0 \uparrow\rangle + \sqrt{1/3}\,|Y_1^1 \downarrow\rangle \\
|3/2 - 1/2\rangle &= \sqrt{1/3}\,|Y_1^{-1} \uparrow\rangle + \sqrt{2/3}\,|Y_1^0 \downarrow\rangle \\
|3/2 - 3/2\rangle &= |Y_1^{-1} \downarrow\rangle \ . \\
|1/2 \quad 1/2\rangle &= \sqrt{1/3}\,|Y_1^0 \uparrow\rangle - \sqrt{2/3}\,|Y_1^1 \downarrow\rangle \\
|1/2 - 1/2\rangle &= \sqrt{2/3}\,|Y_1^{-1} \uparrow\rangle - \sqrt{1/3}\,|Y_1^0 \downarrow\rangle \ .
\end{aligned} \tag{2.21}$$

The Hamiltonian in this basis then becomes:

$$H = \frac{1}{6}\begin{pmatrix} 3\lambda+3\xi & 0 & 0 & 0 & 0 & 0 \\ 0 & 3\lambda+\xi & 0 & 0 & \sqrt{8}\xi & 0 \\ 0 & 0 & 3\lambda-\xi & 0 & 0 & \sqrt{8}\xi \\ 0 & 0 & 0 & 3\lambda-3\xi & 0 & 0 \\ 0 & \sqrt{8}\xi & 0 & 0 & -6\lambda-\xi & 0 \\ 0 & 0 & \sqrt{8}\xi & 0 & 0 & -6\lambda+\xi \end{pmatrix} . \tag{2.22}$$

The introduction of a spin field breaks the rotational symmetry, and so $j = 3/2$ and $j = 1/2$ levels are allowed to mix, as evidenced by the off-diagonal terms. About the magnetization axis, however, rotational symmetry is preserved, and so m_j is still a good quantum number. In the limit $\lambda >> \xi$ – which is closely realized for a $2p$ core level – the $p_{3/2}$ and $p_{1/2}$ levels are shifted energetically by $+\lambda/2$ and $-\lambda$, respectively, leading to a spin-orbit splitting of 1.5λ, and an exchange splitting of $\xi/3$ appears between adjacent m_j sublevels. The level scheme for this limit is shown in Fig. 2.2.

For general λ and ξ, Eq. (2.22) can be easily diagonalized to obtain the angular eigenstates $\Phi_\sigma(\theta,\phi)$. To calculate the matrix elements of Eq. (2.17) for a general initial state Ψ_{core}, it is thus sufficient to know the matrix elements for the $|j,\ m_j\rangle$ basis states. These have been computed for the three basic photon polarizations $\tilde{T}_\epsilon = rY_1^1$, rY_1^{-1}, and rY_1^0, and are presented in Tables 1, 2, and 3, respectively. In these tables, θ_k and ϕ_k define the photoelectron wavevector. The $\tilde{R}_l$ are defined as $\tilde{R}_l = R_l e^{i\delta_l}$, where R_l are the radial matrix elements for the two dipole-allowed final state channels,

$$R_l = \int_0^\infty f_{kl}(r) r^3 f_{nl}(r) dr \ , \tag{2.23}$$

and the δ_l are the respective phase shifts. These matrix elements and phase shifts have been calculated and tabulated by Goldberg, Fadley, and Kono [47], for several elements

and energies.

To summarize, we assume that we have an oriented atom magnetized in the z direction, as shown in Fig. 2.1. The photon incidence direction (θ_q, ϕ_q) and polarization (α, δ) defines the dipole operator via Eq. (2.15) and Eq. (2.10). Dipole matrix elements between the $|j,\ m_j\rangle$ basis states and the outgoing photoelectron can now be determined using Tables 1-3. The appropriate linear combinations of these can be formed by diagonalizing the Hamiltonian in Eq. (2.22), which also determines the energies of the states. Finally, Eq. (2.17) can be used to calculate the spin-resolved intensities of each line.

2.3 Results and Discussion

2.3.1 Spin-resolved spectra

In Fig. 2.3(a) we present experimental spin-resolved spectra due to Van Campen *et al.* [25] Data were smoothed by one cycle of equal weight three-point averaging. The polycrystalline Fe sample was magnetized in-plane along what we take to be the $+z$ direction (see Fig. 2.1) and irradiated with a Mg Kα ($\hbar\omega$ = 1253.6 eV) x-ray source. Photoelectrons were collected normal to the surface plane ($\mathbf{k} \sim \hat{e}_x$) and their spin measured along the magnetization axis. The photon $\mathbf{q}$ was defined by $\theta_q = 117°$ and $\phi_q = 142.5°$, which is a chiral geometry. To eliminate spin-orbit-induced spin polarization due to chirality, spin-resolved spectra were averaged over both magnetic orientations. In Fig. 2.3(a), photoelectrons with spin parallel to the majority in the valence band are given by the solid line, and the corresponding minority spectrum is given by the dashed line. For both levels, an exchange splitting is clearly evident; i.e., the peak of the majority spectrum is shifted to higher binding energy. Except for the leading edge of the $2p_{3/2}$ main line, the experimental spectra show a strong majority spin polarization throughout. Part of this is due to the spin polarization of the secondaries. To permit a more meaningful

comparison with theoretical results, we subtract from the experimental results a simple linear background that eliminates the spin polarization at the leading and trailing edges. The resulting spectra are presented in Fig. 2.3(b). In Fig. 2.3(c) we present theoretical spin-resolved spectra calculated for the same experimental geometry described above, and also averaged over both magnetic orientations to eliminate spurious spin polarizations. We use a spin-orbit splitting of 13 eV ($\lambda = 8.67$ eV) and a spin field of $\xi = 1.20$ eV, and the resulting lines were convoluted using a Doniach-Sunjic lineshape with singularity index $\alpha = 0.35$ and Lorentz broadening 1.2 eV FWHM. These values were chosen to best fit the experimental lineshapes and peak positions. Overall, the theoretical results are in good agreement with the background-subtracted experimental results. In Fig. 2.3(d), the theoretical and experimental spin polarizations are plotted. These difference spectra were normalized to the peak height of the spin-integrated intensity. The theoretical difference spectra also agree well with the main features of the experimental results, which are characterized by plus/minus features at both levels.

A more careful comparison yields the following observations:

(1) Experimentally, the main line for the majority spectrum is shifted ~ 0.5 eV to higher binding energy (relative to the minority position) for both $2p_{3/2}$ and $2p_{1/2}$. In our calculation, it is approximately 0.85 eV for $2p_{3/2}$ and 0.30 eV for $2p_{1/2}$. A more realistic treatment of the many-body interactions may account for this discrepancy. For instance, by including many-body terms in an accurate way, it was found theoretically that the energetic splittings of the $2p_{3/2}$ and $2p_{1/2}$ main lines in Ni $2p$ are approximately equal [38].

(2) In both theory and experiment, the minority peak intensity is enhanced at the $2p_{3/2}$ main line, and majority peak intensity is enhanced at $2p_{1/2}$. This result is a consequence of the off-diagonal terms in Eq. (2.22), which lead to mixing between the $2p_{3/2}$ and $2p_{1/2}$ levels. Without such mixing, the majority and minority peak intensities

would be equal, even though the peaks would occur at different binding energies due to exchange.

(3) Experimentally, the lineshapes are spin dependent, with the lineshapes for the majority photoelectrons being more asymmetrical. In other words, the majority spectrum exhibits greater strength in the high-binding-energy tail, and correspondingly less in the main line. This is especially evident for the $2p_{3/2}$ main line. Such intensity profiles are indicative of satellite structures. In Ni, such spin-dependent lineshapes are also found, both experimentally [27] and theoretically [38, 39], and are a consequence of well-known satellite structures. Theoretically, the satellite is expected to have a majority spin polarization because the mean majority satellite position is shifted to higher binding energy, and the high-binding-energy side of the satellite transfers less spectral weight to the main lines [38, 39].

2.3.2 Magnetic dichroism

In a magnetic dichroism experiment, light with a definite polarization impinges upon a magnetic sample, and the photoemission spectrum with a definite magnetization ($M\uparrow$ or $M\downarrow$) is measured as $I_{M\uparrow}$ or $I_{M\downarrow}$. In one way of measuring the dichroism, the magnetization direction is simply reversed, and the difference spectrum $I_{M\uparrow} - I_{M\downarrow}$ gives the magnetic dichroism. It is instructive to consider the limit $\lambda >> \xi$, which is approximated by a $2p$ core level in Fe. For this limit, to first order, the core eigenstates are given simply by the $|j,\ m_j\rangle$ spin-orbit eigenstates, and the energy separation between adjacent m_j sublevels is $\xi/3$. In this case, reversing the magnetization will not change the intensities of the states, but will merely interchange the energetic positions of $|j,\ m_j\rangle$ and $|j,\ -m_j\rangle$. Such a situation is shown schematically in Fig. 2.2. Therefore, in this limit, the magnetic dichroism for a given line is calculated simply by considering a single magnetic orientation and taking $I_{|j,\ m_j\rangle} - I_{|j,\ -m_j\rangle}$.

For RCP excitation, and the special case of photon $\mathbf{q}$ parallel to the magnetization $\mathbf{M}$, this intensity difference is

$$\begin{aligned} 2p_{3/2}: \quad I_{|3/2,\,3/2\rangle} - I_{|3/2,\,-3/2\rangle} &= 3\Delta_{MCDAD} \\ I_{|3/2,\,1/2\rangle} - I_{|3/2,\,-1/2\rangle} &= \Delta_{MCDAD} \\ 2p_{1/2}: \quad I_{|1/2,\,1/2\rangle} - I_{|1/2,\,-1/2\rangle} &= 2\Delta_{MCDAD}\ , \end{aligned} \tag{2.24}$$

where Δ_{MCDAD} gives the angular distribution of the dichroism:

$$\Delta_{MCDAD} = \frac{1}{3}\left(3R_2^2\sin^2\theta_k - R_0^2 - R_2^2 - R_0R_2\left(3\cos^2\theta_k - 1\right)\cos(\delta_0 - \delta_2)\right)\ . \tag{2.25}$$

MCDAD can be qualitatively explained as a result of the spin polarization induced by circular-polarized excitation. At certain takeoff directions, there may be strong preferential emission of a given spin component – say spin up – at one of the levels. If the magnetization direction is also up, then this peak is primarily minority in character, and so is shifted to lower binding energy. When the magnetization is reversed, the spin polarization does not change (still spin up), but the peak is now majority in character and so shifts to higher binding energy, thereby leading to different spectra upon magnetic reversal.

With linear-polarized excitation, there can also be an induced spin polarization, which in turn leads to an angular-dependent magnetic linear dichroism (MLDAD). For example, let the dipole operator be given by $T_\epsilon \sim y$ (i.e., $\mathbf{q} \sim \hat{e}_x$ and $\alpha = 90°$). The induced spin polarization is then

$$\begin{aligned} 2p_{3/2}: \quad I_\uparrow - I_\downarrow &= 2R_0R_2\sin^2\theta_k\sin 2\phi_k\sin(\delta_0 - \delta_2) \\ 2p_{1/2}: \quad I_\uparrow - I_\downarrow &= -2R_0R_2\sin^2\theta_k\sin 2\phi_k\sin(\delta_0 - \delta_2)\ . \end{aligned} \tag{2.26}$$

The magnetic dichroism is calculated in the same way as before,

$$2p_{3/2}: \quad I_{|3/2,\,3/2\rangle} - I_{|3/2,\,-3/2\rangle} = 3\Delta_{MLDAD} \tag{2.27}$$

$$
\begin{aligned}
I_{|3/2,\,1/2\rangle} - I_{|3/2,\,-1/2\rangle} &= \Delta_{MLDAD} \\
2p_{1/2}: \quad I_{|1/2,\,1/2\rangle} - I_{|1/2,\,-1/2\rangle} &= 2\Delta_{MLDAD}\ ,
\end{aligned}
$$

where now

$$\Delta_{MLDAD} = R_0 R_2 \sin^2\theta_k \sin 2\phi_k \sin(\delta_0 - \delta_2). \tag{2.28}$$

Therefore, except for an angular-dependent scaling factor, the MLDAD is equal to the MCDAD, as discussed by previous workers [49]. Although this result was derived here for a one-electron model in the limit $\lambda >> \xi$, it holds more generally for any values of spin orbit and exchange, and is even valid for the many-body case [49]. In other words, the lineshapes for both types of dichroism are identical, as shown schematically in Fig. 2.2.

Magnetic dichroism can also be observed with unpolarized light, which is an incoherent superposition of s and p components. Although the s component is non-dichroic, the p component leads to the same dichroism as before. In Fig. 2.4(a) we present experimental photoemission spectra, due to Fanelsa *et al.*, for the $2p$ core of Fe (001) excited by a Mg Kα x-ray source [34]. The sample was magnetized in the surface plane, and both the photon and photoelectron wavevectors were in the plane normal to the magnetization. Photoelectron takeoff was normal to the surface and made an angle of 45° with respect to the photon incidence direction. $I_{M\uparrow}$ and $I_{M\downarrow}$ are the spin-integrated spectra for magnetization in the up and down directions, respectively. The theoretical spectra are shown in Fig. 2.4(b), and the difference spectra (normalized to peak intensity) are plotted in Fig. 2.4(c). These spectra were calculated again using $\lambda = 8.67$ eV, and $\xi = 1.2$ eV, and the lines were convoluted with the same Doniach-Sunjic lineshape as before. Overall, the theoretical results agree well with experiment, and are characterized by a plus/minus feature at $2p_{1/2}$ and a minus/plus feature at $2p_{3/2}$.

However, there are discrepancies between experiment and theory. For instance, at

the $2p_{3/2}$ main line, $I_{M\uparrow}$ has a greater intensity than $I_{M\downarrow}$, whereas in the theoretical calculation they are equal. Also, the experimental dichroic signal in the interval between the main lines is much larger than in the theoretical calculation. Both of these discrepancies may be attributed to many-body effects not accurately described within the present model. For instance, $I_{M\downarrow}$ has a majority spin polarization at $2p_{3/2}$. The effect of satellite structures is to shift majority spectral weight to the satellite region, and away from the main line, which then acquires minority spin polarization. This effect would explain the shape of the magnetic dichroism curve, although it cannot be modeled within the exchange-split main line approach considered here.

A direct comparison of the *magnitude* of the dichroism is not meaningful here because the experimental data were taken from a single-crystal sample. It was recently shown by Fanelsa *et al.* that photoelectron diffraction can have a strong effect on the magnitude of the dichroic asymmetry for such cases [34].

As a final illustration of the usefulness of the model, we compare the MCDAD which results from reversal of the sample magnetization to the MCDAD which results from reversal of the photon helicity. For simplicity, we again consider the limit $\lambda >> \xi$, so that the picture of Fig. 2.2 applies. If the magnetization $\mathbf{M}$, photon $\mathbf{q}$, and photoelectron $\mathbf{k}$ all lie in the same plane, then it can be easily verified (e.g., using the present model) that both dichroisms are equivalent. However, for a more general geometry this is not true.

More specifically, suppose that the system is magnetized in the surface plane with $\mathbf{M}$ as usual along the $+z$ direction and with a surface normal given by $\hat{n} = \hat{e}_x$. Let the photon $\mathbf{q}$ be incident in the xz plane with $\theta_q = 45°$ and $\phi_q = 180°$ (see Fig. 2.1), and consider normal emission ($\theta_k = 90°$, $\phi_k = 0°$). For convenience, we define an energy-integrated dichroic asymmetry A. If the magnetization is reversed, then A is given

by

$$A = (I)^{-1} \sum_n S_n (I_n(M \uparrow) - I_n(M \downarrow)) \,, \tag{2.29}$$

where the sum is over all six lines n, and the normalization is simply the total intensity for both magnetizations

$$I = \sum_n (I_n(M \uparrow) + I_n(M \downarrow)) \,. \tag{2.30}$$

Here, $S_n = \pm 1$, depending on the sign of the dichroism for a given line. More explicitly, we use $S_n = +1$ for the three lines that exhibit positive dichroism in Fig. 2.2, and $S_n = -1$ for the other three lines. Such a definition is necessary in order to ensure that the dichroisms of the various lines *add* rather than *cancel*. In this way, the asymmetry is simply the net area of the difference spectrum divided by the area of the sum.

Alternatively, the dichroism could be measured by reversing the helicity of the light. Suppose that the helicity is switched from RCP to LCP. In this case, we define the dichroic asymmetry as

$$\tilde{A} = (\tilde{I})^{-1} \sum_n S_n (I_n(RCP) - I_n(LCP)) \,, \tag{2.31}$$

where again the sum is over all six lines n, S_n is defined the same as before, and the normalization is given by

$$\tilde{I} = \sum_n (I_n(RCP) + I_n(LCP)) \,. \tag{2.32}$$

For M along $+z$, and with **k** and **q** as described above, by symmetry both definitions give the same result. However, if the magnetization is now rotated by an angle β about the surface normal, so that M remains in the yz plane, while keeping **k** and **q** fixed, then the two definitions are not equivalent. In Fig. 2.5 we present the theoretical dichroic asymmetry due to reversal of magnetization, calculated as a function of β according to Eq. (2.29). The curves shown are for RCP, LCP, s-, and p-polarized excitation, using

as an example a radial matrix element ratio of $R_2/R_0 = 3.0$ and a phase shift difference of $\delta_2 - \delta_0 = 1.0$ (57.3°).

The dichroism A_s for s-polarized light is always zero. For p-polarized light, the dichroism A_p is nonzero and reaches a maximum magnitude at $\beta = 90°$. Observe that $\beta = 90°$ corresponds to the standard MLDAD geometry. In this model, which does not include photoelectron diffraction, the dichroism resulting from p-polarized excitation is due entirely to cross-channel interference. In other words, A_p is proportional to the sine of the phase difference, as indicated in Eq. (2.28).

Another result evident from Fig. 2.5 is that, for a general rotation angle β, $A_{RCP} \neq -A_{LCP}$. This can also be seen as a consequence of cross-channel interference. If A_{RCP} and A_{LCP} were equal and opposite, then the dichroism resulting from unpolarized light would vanish. Since $A_s = 0$, this would imply A_p must also vanish. However, for the general case, we have seen that A_p does not vanish due to cross-channel interference. Therefore, for the general case, A_{RCP} and A_{LCP} cannot be equal and opposite. The correct relationship is given by

$$A_{RCP}(90° + \eta) = A_{LCP}(90° - \eta) \ , \tag{2.33}$$

where η is the rotation angle away from $\beta = 90°$.

For comparison, we now show the dichroic asymmetry $\tilde{A}_{RCP}$ due to switching the photon helicity from RCP to LCP, calculated according to Eq. (2.31). At $\beta = 0°$ and 180°, the two dichroisms are identical, but they deviate from each other for β in between. At $\beta = 90°$, $\tilde{A}_{RCP}$ vanishes by symmetry, i.e., the spectra due to RCP and LCP are identical.

2.4 Conclusions

We have presented a one-electron theory to describe spin- and angle-resolved photoe-

mission spectra from a p core level of a ferromagnetic system, and for a general photon polarization. We have applied the model to calculate spin-resolved Fe $2p$ spectra as well as magnetic dichroism. Agreement with experiment is generally very good. The discrepancies can be attributed to many-body effects. The spin-dependent lineshapes are particularly interesting, because they are indicative of satellite structures. Finally, we have used the model to compare the magnetic dichroism arising from reversal of sample magnetization to that obtained from reversal of photon helicity, and showed that the two definitions are equivalent only for special geometries.

Table 2.1: Dipole Operator Matrix Elements, $\tilde{T}_\epsilon = rY_1^1$.

$\langle\Psi_{k\uparrow}\|$	$\langle\Psi_{k\downarrow}\|$	$\|j,\ m_j\rangle$
$-\frac{3}{2}\tilde{R}_2 \sin^2\theta_k e^{2i\phi_k}$	0	$\|\frac{3}{2}\ \ \frac{3}{2}\rangle$
$\sqrt{3}\tilde{R}_2 \sin\theta_k \cos\theta_k e^{i\phi_k}$	$-\sqrt{\frac{3}{4}}\tilde{R}_2 \sin^2\theta_k e^{2i\phi_k}$	$\|\frac{3}{2}\ \ \frac{1}{2}\rangle$
$-\sqrt{\frac{1}{3}}\left(\tilde{R}_0 + \frac{1}{2}\tilde{R}_2(3\cos^2\theta_k - 1)\right)$	$\sqrt{3}\tilde{R}_2 \sin\theta_k \cos\theta_k e^{i\phi_k}$	$\|\frac{3}{2}\ -\frac{1}{2}\rangle$
0	$-\left(\tilde{R}_0 + \frac{1}{2}\tilde{R}_2(3\cos^2\theta_k - 1)\right)$	$\|\frac{3}{2}\ -\frac{3}{2}\rangle$
$\sqrt{\frac{3}{2}}\tilde{R}_2 \sin\theta_k \cos\theta_k e^{i\phi_k}$	$\sqrt{\frac{3}{2}}\tilde{R}_2 \sin^2\theta_k e^{2i\phi_k}$	$\|\frac{1}{2}\ \ \frac{1}{2}\rangle$
$-\sqrt{\frac{2}{3}}\left(\tilde{R}_0 + \frac{1}{2}\tilde{R}_2(3\cos^2\theta_k - 1)\right)$	$-\sqrt{\frac{3}{2}}\tilde{R}_2 \sin\theta_k \cos\theta_k e^{i\phi_k}$	$\|\frac{1}{2}\ -\frac{1}{2}\rangle$

Table 2.2: Dipole Operator Matrix Elements, $\tilde{T}_\epsilon = rY_1^{-1}$.

$\langle\Psi_{k\uparrow}\|$	$\langle\Psi_{k\downarrow}\|$	$\|j,\ m_j\rangle$
$-\left(\tilde{R}_0 + \frac{1}{2}\tilde{R}_2(3\cos^2\theta_k - 1)\right)$	0	$\|\frac{3}{2}\ \ \frac{3}{2}\rangle$
$-\sqrt{3}\tilde{R}_2 \sin\theta_k \cos\theta_k e^{-i\phi_k}$	$-\sqrt{\frac{1}{3}}\left(\tilde{R}_0 + \frac{1}{2}\tilde{R}_2(3\cos^2\theta_k - 1)\right)$	$\|\frac{3}{2}\ \ \frac{1}{2}\rangle$
$-\sqrt{\frac{3}{4}}\tilde{R}_2 \sin^2\theta_k e^{-2i\phi_k}$	$-\sqrt{3}\tilde{R}_2 \sin\theta_k \cos\theta_k e^{-i\phi_k}$	$\|\frac{3}{2}\ -\frac{1}{2}\rangle$
0	$-\frac{3}{2}\tilde{R}_2 \sin^2\theta_k e^{-2i\phi_k}$	$\|\frac{3}{2}\ -\frac{3}{2}\rangle$
$-\sqrt{\frac{3}{2}}\tilde{R}_2 \sin\theta_k \cos\theta_k e^{-i\phi_k}$	$\sqrt{\frac{2}{3}}\left(\tilde{R}_0 + \frac{1}{2}\tilde{R}_2(3\cos^2\theta_k - 1)\right)$	$\|\frac{1}{2}\ \ \frac{1}{2}\rangle$
$-\sqrt{\frac{3}{2}}\tilde{R}_2 \sin^2\theta_k e^{-2i\phi_k}$	$\sqrt{\frac{3}{2}}\tilde{R}_2 \sin\theta_k \cos\theta_k e^{-i\phi_k}$	$\|\frac{1}{2}\ -\frac{1}{2}\rangle$

Table 2.3: Dipole Operator Matrix Elements, $\tilde{T}_\epsilon = rY_1^0$.

$\langle\Psi_{k\uparrow}\|$	$\langle\Psi_{k\downarrow}\|$	$\|j,\ m_j\rangle$
$\sqrt{\frac{9}{2}}\tilde{R}_2 \sin\theta_k \cos\theta_k e^{i\phi_k}$	0	$\|\frac{3}{2}\ \ \frac{3}{2}\rangle$
$\sqrt{\frac{2}{3}}\left(\tilde{R}_0 - \tilde{R}_2(3\cos^2\theta_k - 1)\right)$	$\sqrt{\frac{3}{2}}\tilde{R}_2 \sin\theta_k \cos\theta_k e^{i\phi_k}$	$\|\frac{3}{2}\ \ \frac{1}{2}\rangle$
$-\sqrt{\frac{3}{2}}\tilde{R}_2 \sin\theta_k \cos\theta_k e^{-i\phi_k}$	$\sqrt{\frac{2}{3}}\left(\tilde{R}_0 - \tilde{R}_2(3\cos^2\theta_k - 1)\right)$	$\|\frac{3}{2}\ -\frac{1}{2}\rangle$
0	$-\sqrt{\frac{9}{2}}\tilde{R}_2 \sin\theta_k \cos\theta_k e^{-i\phi_k}$	$\|\frac{3}{2}\ -\frac{3}{2}\rangle$
$\sqrt{\frac{1}{3}}\left(\tilde{R}_0 - \tilde{R}_2(3\cos^2\theta_k - 1)\right)$	$-\sqrt{3}\tilde{R}_2 \sin\theta_k \cos\theta_k e^{i\phi_k}$	$\|\frac{1}{2}\ \ \frac{1}{2}\rangle$
$-\sqrt{3}\tilde{R}_2 \sin\theta_k \cos\theta_k e^{-i\phi_k}$	$-\sqrt{\frac{1}{3}}\left(\tilde{R}_0 - \tilde{R}_2(3\cos^2\theta_k - 1)\right)$	$\|\frac{1}{2}\ -\frac{1}{2}\rangle$

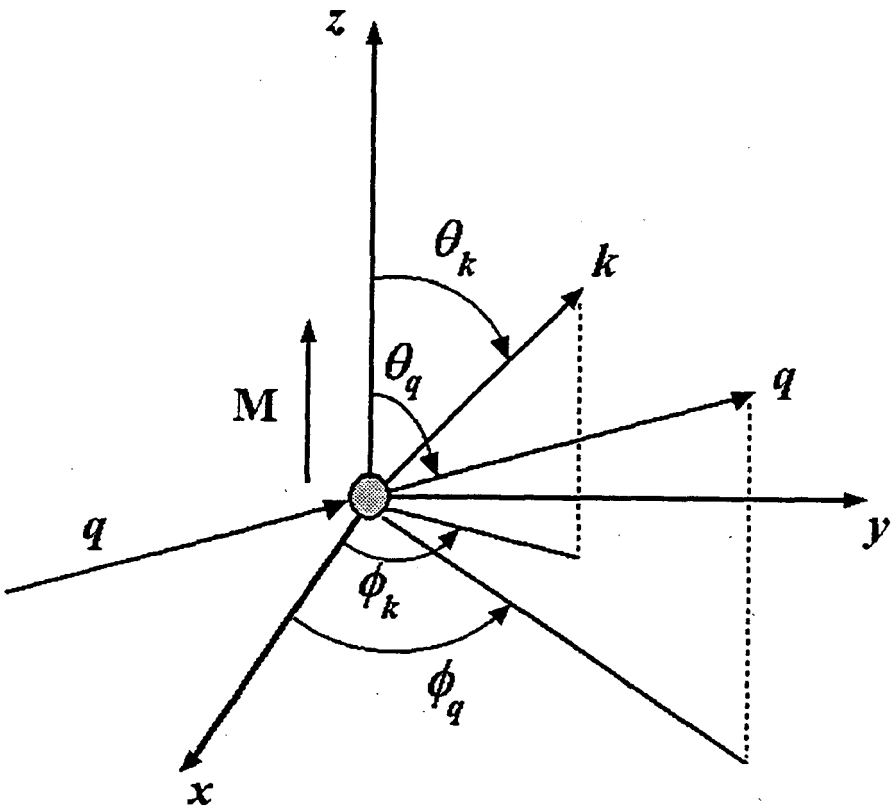

Figure 2.1: General geometry. Magnetization is along the $+z$ direction. **k** and **q** are the photoelectron and photon wavevectors, respectively.

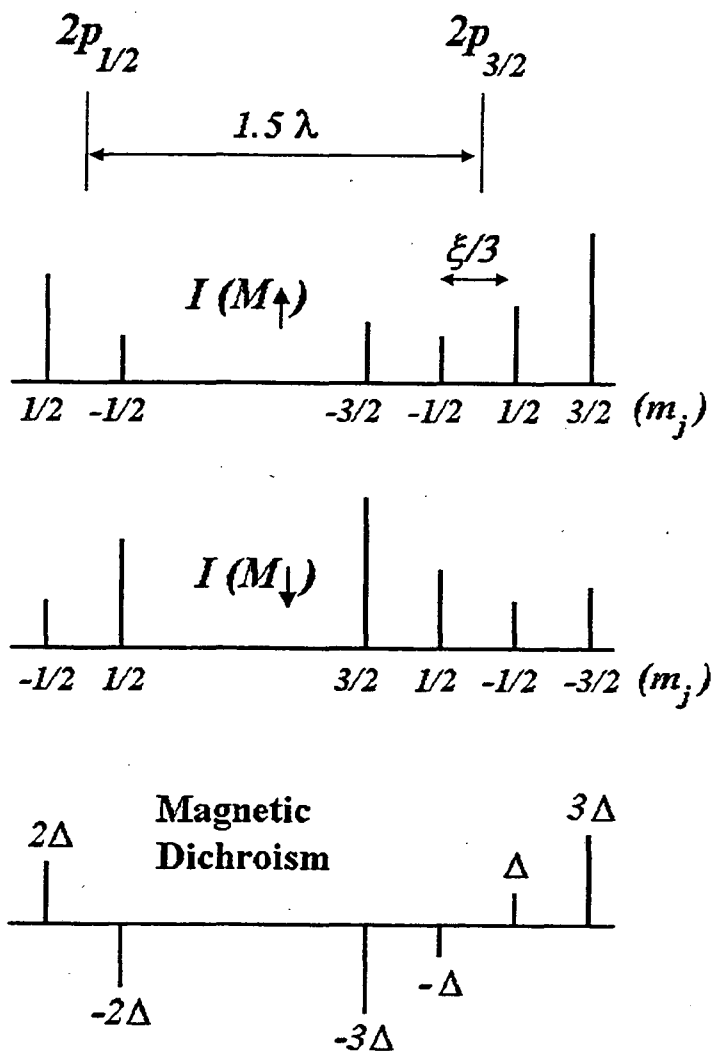

Figure 2.2: Schematic diagram showing energetic positions of $|j,\ m_j\rangle$ core states, for both magnetic orientations, and the resulting magnetic dichroism. Such a situation is realized when the spin-orbit parameter λ is much larger than the exchange energy ξ.

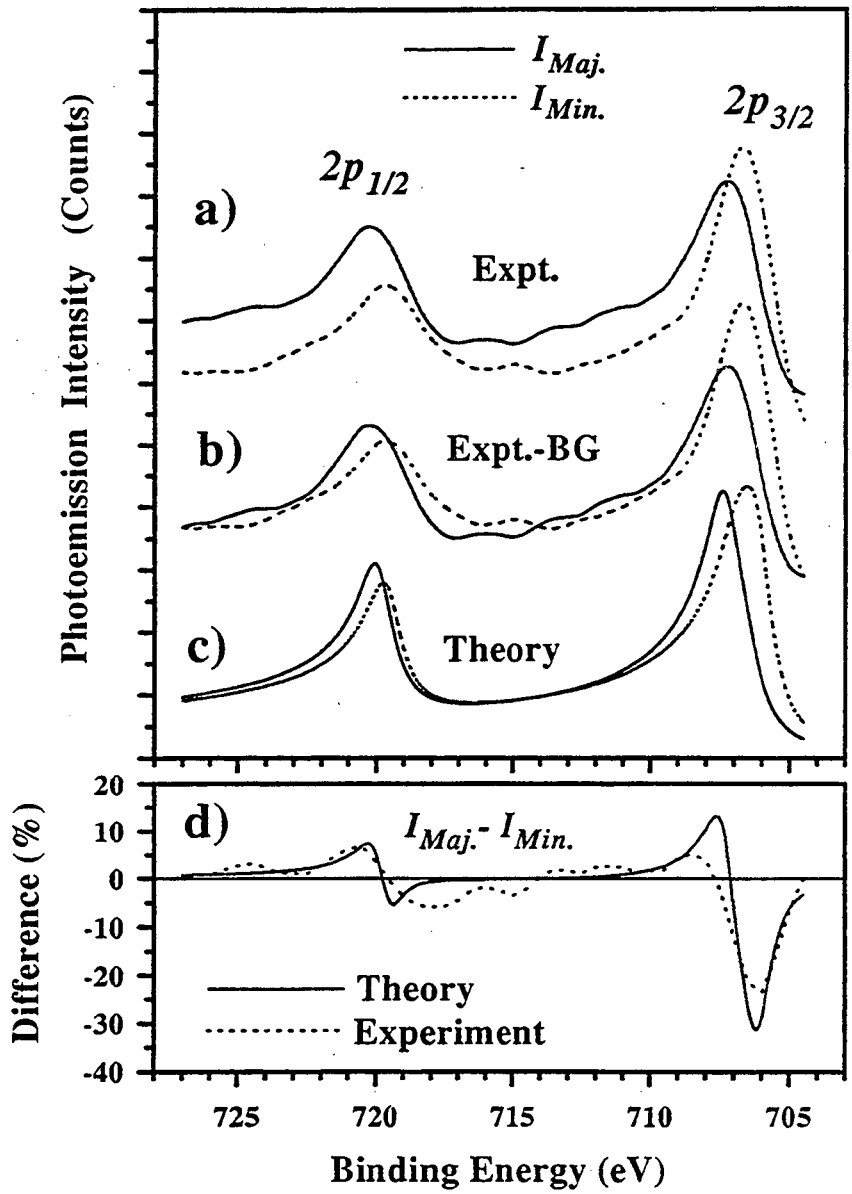

Figure 2.3: Spin-resolved Fe $2p$ photoemission spectra. (a) Experimental results due to Van Campen *et al.* [2]. Data were smoothed with one cycle of three-point averaging. (b) Background-subtracted experimental spectra. (c) Theoretical results. Lines were convoluted with a Doniach-Sunjic lineshape. (d) Spin polarization, normalized to the peak intensity.

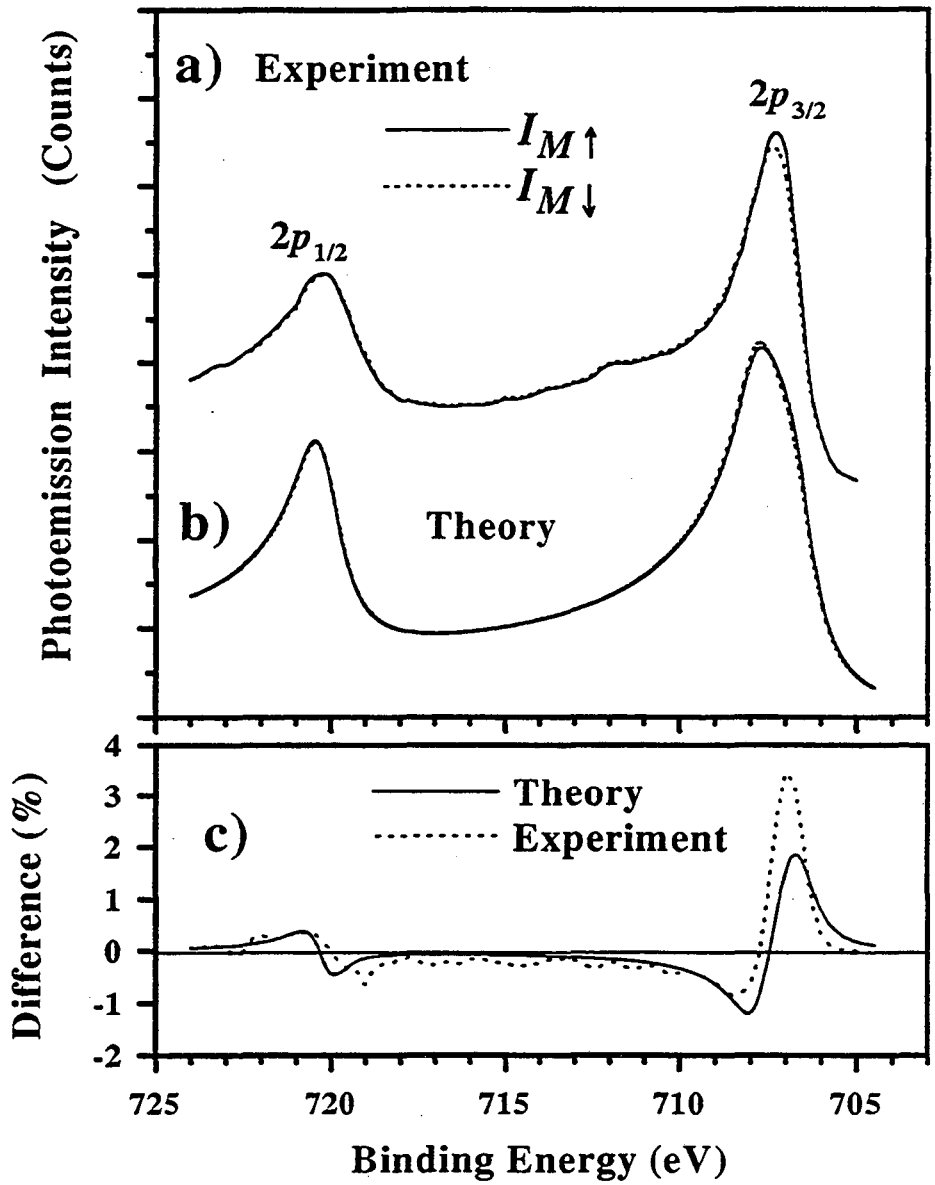

Figure 2.4: Fe $2p$ magnetic unpolarized dichroism. (a) Experimental results due to Fanelsa *et al.* [13] with spin-integrated spectra for both magnetic orientations. The small peak at 712 eV is due to satellite x-rays. (b) Theoretical results. Lines were convoluted with a Doniach-Sunjic lineshape with singularity index $\alpha = 0.35$ and Lorentz broadening 1.2 eV FWHM. (c) Difference spectrum for theory and experiment, normalized to the peak intensity.

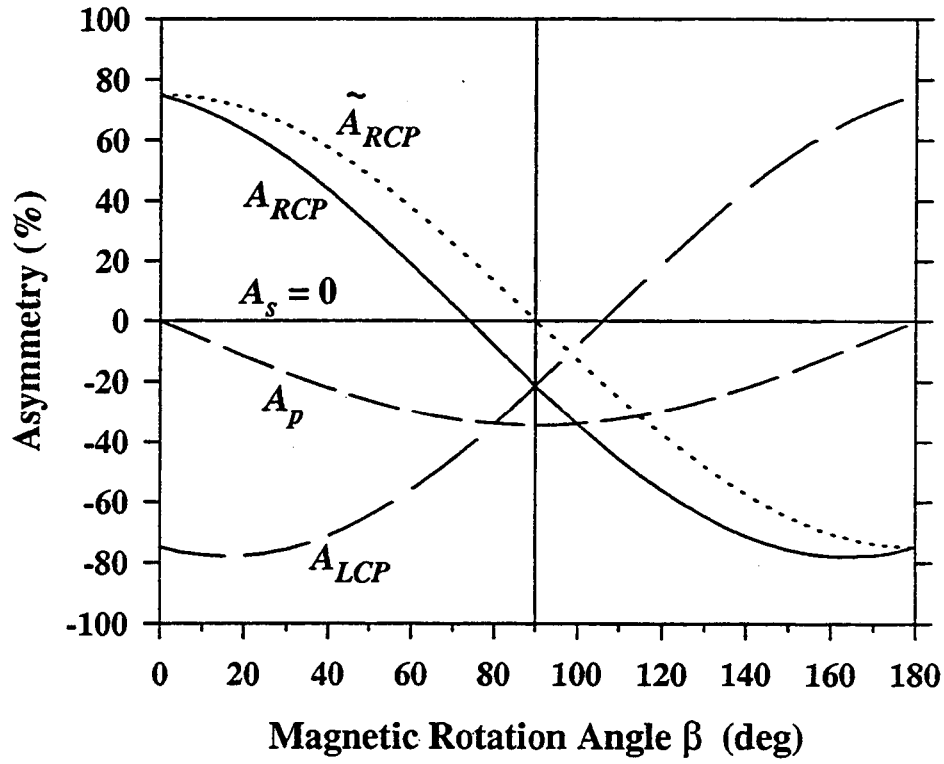

Figure 2.5: Dichroic asymmetry A due to reversal of sample magnetization for RCP, LCP, s-, and p-polarized excitation, for geometry described in text. The dichroic asymmetry $\tilde{A}_{RCP}$, due to switching photon helicity from RCP to LCP, is also shown for comparison.

Chapter 3

Many-Body Theory of Ni $2p$ Photoemission

3.1 Introduction

Photoemission from Ni metal has attracted much attention over the years [27, 38, 50, 51, 52, 53, 54, 55]. Ni is a classic itinerant ferromagnet, with a valence bandwidth roughly equal to the intrasite Coulomb repulsion. This results in an intermediate coupling regime in which both the one-electron picture and the purely localized viewpoint begin to breakdown: satellite structures cannot be explained in the former approach, whereas extra-atomic screening effects cannot be described by the latter. Thus, Ni presents a particularly interesting and challenging many-body problem for the theorist.

Photoemission from ferromagnetic Ni displays several intriguing effects:

(1) Angle-resolved photoemission studies [50] of the valence band showed a much smaller dispersion than that predicted from theoretical band structure calculations[56]. This "narrowing of the band" has been attributed to correlation effects among the valence electrons[51, 52, 53].

(2) The valence band photoemission spectrum exhibits satellites approximately 6 eV to the left (higher binding energy) of the main lines[54]. These satellites, a many-body effect, correspond to final states with a high probability of finding two valence holes on the same site[53].

(3) Core-level spectra for Ni are also known to exhibit satellites approximately 6 eV to the left of the main lines[54]. These satellites were attributed to final states involving one core and one valence hole on the same site–also a two-hole final state.

Due to the exchange interaction between the core level and the spin-polarized valence band, core spectra may depend on the spin orientation of the outgoing photoelectrons. Measuring the spin of the outgoing photoelectron in spin-resolved x-ray photoelectron spectroscopy (SRXPS) is a direct way to probe the spin character of the core levels, and thus the local magnetic environment. Until recently, however, the spin polarizations of the spectra of deep core levels were not known. See and Klebanoff used unpolarized Mg $K\alpha$ X-rays to conduct the first comprehensive spin-resolved study of *all* accessible core levels, revealing a rich and interesting structure[27, 55]. For instance, the Ni $3s$ 6-eV satellite displayed an apparent 100% majority spin polarization, in contrast to the mixed spin polarization expected for a $3s^1 3d^9$ final-state configuration. The Ni $2p$ spectra also exhibit an interesting spin polarization, which we address below.

The ability to excite core levels with polarized synchrotron radiation has opened a new avenue in the study of core-level photoemission. For circular-polarized excitation, the photoemission spectrum depends on the relative orientation of the photon helicity and the sample magnetization. The photon couples indirectly to the core electron spin through the spin-orbit interaction. The core electron spin, in turn, couples to the spin polarized valence band via intra-atomic exchange. Thus, the photon couples indirectly to the sample magnetization, leading to distinct spectra for the two helicities. Measuring such intensity differences in photoemission is known as magnetic circular dichroism (MCD). Baumgarten *et al.* [21] used this technique to measure the exchange splittings of the Fe $2p$ core electrons, proving that polarized excitation sources could also be used as a probe the local magnetic environment.

Magnetic dichroism can also be observed with linear p-polarized light. The exchange interaction induces a spin polarization which reverses upon reversal of the magnetization direction. The spin-orbit interaction on the other hand, in a chiral geometry, induces a spin polarization which is independent of magnetization [57]. Therefore, the

spin-integrated spectrum may change upon reversal of the sample magnetization. Such dichroism was first observed by Roth, Hillebrecht, Rose, and Kisker in photoemission from the Fe $3p$ core level [22]. These effects result from cross-channel interference and are only observable in angle-resolved measurements, vanishing with integration over emission angle [48, 58]. Accordingly, this effect has been referred to as magnetic linear dichroism in the angular distribution (MLDAD). Roth and the same coworkers also observed another kind of dichroism using linear s-polarized light [59]. This type of dichroism, as discussed by van der Laan [48], does not depend on cross-channel interference and is also observable in angle-integrated photoemission. Such dichroism, which will not be considered in this work, has been termed magnetic linear dichroism (MLD) to distinguish it from MLDAD.

By symmetry, MLDAD cannot be observed with linear s-polarized light [48]. Unpolarized light, on the other hand, is an incoherent superposition of s and p components, and therefore may also exhibit dichroic effects. Such magnetic unpolarized dichroism in the angular distributions (MUDAD) was first observed by Hillebrecht and Herberg [23] in Fe $3p$ core-level photoemission, thereby showing that even standard unpolarized x-ray sources could be used to probe the magnetic structure of the core levels.

With these recent experimental advances, core-level photemission is rapidly becoming a powerful tool in the investigation of magnetic materials. The need thus arises for a detailed description of the core-level photoemission problem, especially regarding the nature and origin of the spin polarization and the subtle interplay between single-particle and many-body effects. Ni, due to its intermediate coupling nature, is a particularly instructive example to consider, and many of the results here can be extended to the other itinerant ferromagnets.

In this chapter, we elaborate much more fully on our previous work [38], which considered only spin-resolution with unpolarized excitation and spin-integration with

circular-polarized excitation. We describe in greater detail our model and calculational details, and extend the analysis to consider spin-resolved and spin-integrated Ni $2p$ spectra for circular, linear, and unpolarized light. Many-body effects and extra-atomic screening are discussed. Finally, a detailed analysis of the final-state configurations is presented, allowing one to assign a precise physical interpretation to the various features in the spectrum.

3.2 Model and Calculation

The small-cluster model used by Victora and Falicov [53] to successfully describe the Ni *valence* band photoemission spectrum is extended here to the case of core-level photoemission. The model consists of a small tetrahedral cluster of four atoms, with periodic-boundary conditions imposed to generate the full *fcc* lattice, as shown in Fig. 3.1. Each atom in the crystal can be labeled by an index 1-4, and is surrounded by twelve nearest neighbors of a different index. Therefore, this model treats same-site and nearest-neighbor interactions very accurately, and due to the highly localized nature of the core and valence electrons, these are expected to give the dominant effects.

Rotational and translational symmetries of the *fcc* lattice are fully preserved in this scheme [60]. Neglecting inversion, there are 96 symmetry operations in our system: the 24 proper rotations of a cube (point group O) coupled to the four translations $\vec{0}$, $\vec{\tau_2}$,$\vec{\tau_3}$, and $\vec{\tau_4}$, as shown in Fig. 3.1. Such periodicity dictates that all Bloch states in this system transform according to either Γ (the center) or X (the centers of the square faces) in the Brillouin zone.

Atomic Ni has an outer electron configuration $4s^2 3d^8$. When these atoms join together to form a solid, the tightly-bound $3d$ states form a narrow band, and are crossed by a widely dispersive $4s$ band. A four-atom cluster can accommodate 40 $3d$ electrons and eight $4s$ electrons. The two $4s$ states at Γ are well below E_F and are fully occupied,

whereas the six $4s$ states at X are far above E_F and remain empty. Thus, within the four-atom cluster, the six $4s$ electrons at X "drop into" the lower lying $3d$ band, leaving a total of 38 $3d$ electrons in our system, or equivalently, two d holes on four sites.

While the $4s$ electrons certainly play an important role in the screening process, the $4s$ band is not spin polarized and therefore does not add magnetic structure to the problem. In this work, the $4s$ electrons are not explicitly treated, but are taken into account by renormalizing the direct Coulomb repulsion. The basic idea is that the cost of placing two holes on the same site is reduced by the presence of the $4s$ electrons [61]. For instance, $s^1d^9 + s^1d^9 \rightarrow s^2d^8 + s^0d^{10}$ is energetically more favorable than placing two d holes on the same site in the absence of the highly mobile $4s$ electrons.

As our basis set we use ten $3d$ spin-orbitals per site for the valence states, and six $2p$ spin-orbitals for the core electrons on the photoexcited site. Due to the nearly fully occupied valence band, it is more convenient to express the Hamiltonian in terms of holes:

$$H = \sum_k E_k v_k^\dagger v_k + \lambda_c \sum_{ij} \langle p_i | \vec{l} \cdot \vec{s} | p_j \rangle c_{p_i}^\dagger c_{p_j} + \frac{1}{2} \sum_{klmn} U^{klmn} c_k^\dagger c_l^\dagger c_n c_m, \tag{3.1}$$

where $v_k^\dagger$ and v_k create and destroy valence holes in Bloch states of energy E_k, $c_{p_i}^\dagger$ and c_{p_j} create and destroy holes in core states p_i and p_j respectively, and λ_c is the core-level spin-orbit-splitting parameter. The creation and destruction operators in the last sum create and destroy holes in both the core level and the valence band. Therefore, the U^{klmn} describe the Coulomb repulsion between two valence holes and/or one valence hole and one core hole.

The Hamiltonian contains three kinds of terms:

(a) The terms in the first sum define the electronic band structure, and allow for the valence-band hopping that gives rise to extra-atomic screening effects. One particle in the valence band can occupy any of 20 spatial $3d$ orbitals. These states decompose with

the following space-group symmetries:

$$\Gamma_{12} \oplus \Gamma'_{25} \oplus X_1 \oplus X_2 \oplus X_3 \oplus X_5. \tag{3.2}$$

These symmetrized states can be explicitly constructed using the complete projection operators [62]. The energies of the resulting Bloch states are taken from the spin-averaged band structure calculations of Wang and Callaway [56], and are shown in Table 3.1.

(b) The second sum describes the spin-orbit interaction for the core states. For Ni $2p$ the splitting is approximately 17.26 eV, leading to well resolved $2p_{1/2}$ and $2p_{3/2}$ levels. Valence-level spin-orbit coupling is very small and is neglected in this work.

(c) The terms in the last sum describe the Coulomb interaction, which we calculate exactly for an intrasite repulsion. The U^{klmn} integrals are given by

$$U^{klmn} = \left\langle k(1)l(2)\left|\frac{e^2}{|\vec{r}_1 - \vec{r}_2|}\right|m(1)n(2)\right\rangle, \tag{3.3}$$

where k, l, m ,and n denote atomic spin-orbitals. For two intrasite d holes, neglecting the trivial spin integration, there are $5^4 = 625$ such integrals. Most of these vanish by symmetry. In fact, all can be expressed as linear combinations of only three Slater integrals [63]: U_{dd}, F^2_{dd} and F^4_{dd}. For a p core hole and a d valence hole on the same site, the Coulomb interaction is described by four Slater integrals: $U_{pd}, G^1_{pd}, F^2_{pd}$, and G^3_{pd}. We refer to the U_{dd} and U_{pd} as the *direct* terms, and the various F and G as the *exchange* terms. It is the exchange interaction between the core hole and the spin-polarized valence band, together with core-level spin-orbit coupling, that gives rise to all magnetic dichroism and spin polarization in the spectra. For the exchange terms, we use the values from a previous work [64] which were calculated using Cowan's code [65] and multiplied by 0.80 to account for intra-atomic screening effects. Extra-atomic screening from the delocalized $4s$ electrons precludes such an approach for the direct

terms, which must be treated as adjustable parameters. In this work, we obtain good agreement with experiment using U_{dd} = 3.0 eV and U_{pd} = 4.0 eV, which is consistent with previous estimates using an Anderson impurity model [66]. The values used for the Slater integrals in this work are given in Table 3.1.

To calculate the spectrum, we first need to find the many-body ground state. One valence hole on the four-site cluster can occupy one of 40 spin-orbitals. The second hole can occupy one of the remaining 39. The number of many-body states is thus: 40x39/2! = 780. Therefore, in principle, we need to diagonalize a 780x780 matrix. In the one-electron approximation, with 38 $3d$ electrons in our system, all single-particle Bloch states up to E_F would be occupied , and the ground state would consist of two holes in X_5. Correlation effects would in principle mix higher-energy single-particle Bloch states into the ground state. However, in this system, it is possible to place *both* holes in X_5 states with zero probability of placing both holes on the same site. Therefore, the many-body ground state is also the one-electron ground state. In other words, the ground state is perfectly correlated, and there is no energetic contribution from the electron-electron interaction. The many-body ground state has overall symmetry $^3X_2$. Choosing the magnetization direction as up, the majority electrons are *spin down.* Alternatively, in the ground state, both holes are spin up. The ground state is threefold degenerate, one of which can be written

$$|GS_1\rangle = \frac{1}{2}[c_1^\dagger(d_{xy}\uparrow)c_3^\dagger(d_{xy}\uparrow) - \cdot c_1^\dagger(d_{xy}\uparrow)c_4^\dagger(d_{xy}\uparrow) + c_2^\dagger(d_{xy}\uparrow)c_4^\dagger(d_{xy}\uparrow) - c_2^\dagger(d_{xy}\uparrow)c_3^\dagger(d_{xy}\uparrow)]|0\rangle, \tag{3.4}$$

where $c_j^\dagger(d_{xy}\uparrow)$ creates a spin-up hole on site j in orbital d_{xy}. The other two ground states can be similarly written, and involve the t_{2g} permutations d_{xz} and d_{yz}. Therefore, the ground state is ferromagnetic with 50% d^9 and 50% d^{10} character. The spin moment per atom in the ground state is thus $0.50\mu_B$, in good agreement with other theoretical

estimates of $\sim 0.53\mu_B$ [67].

Upon creation of a core hole, we have 780x6=4680 many-body states. We need to find the eigenstates of this system. Due to the tightly-bound nature of the core hole, we can treat it as being localized on a particular atom. Thus, translational symmetry is broken and the new group is the point group O. Owing to the spin-orbit interaction in the core, we must use the double-group representations [62]. The 4680 states decompose as

$$392\Gamma_6 \oplus 388\Gamma_7 \oplus 780\Gamma_8, \tag{3.5}$$

where Γ_6, Γ_7, and Γ_8 are irreducible representations of dimensions 2,2, and 4 respectively. By using the complete projection operators, we are assured that the Hamiltonian matrices associated with the different rows of an irreducible representation will be identical. This means that we can obtain *all* the final eigenstates by diagonalizing only three matrices of dimension 392, 388, and 780. Furthermore, we find that the spectra obtained by including Γ_8 are *visually indistinguishable* from those obtained by using only $\Gamma_6 + \Gamma_7$ [68]. Apparently, Γ_6 and Γ_7 span a large enough portion of the Hilbert space to accurately describe all of the eigenstates. Therefore, the complete spectrum can be calculated by diagonalizing only two matrices of dimension 392 and 388. Assuming that diagonalization time scales as $\sim n^3$, we save approximately *three orders of magnitude* by fully utilizing group theory. This enormous reduction in computational effort makes it possible to efficiently sample parameter space, and thereby gain insight into the underlying physics of the photoemission spectrum. Details of the symmetrization of the basis functions are given in Appendix A.

With the ground state and final states now defined, we employ the sudden approximation and Fermi's golden rule to calculate the transition probabilities from the ferromagnetic ground state to the final state with core hole and outgoing photoelectron. Again, it is convenient here to think exclusively in terms of holes. The initial state is

a composite wavefunction consisting of the two-hole ferromagnetic ground state Φ_{GS}, plus a third hole of spin σ and wavevector k (not to be confused with the Bloch index k) for the outgoing photoelectron $\Phi_{k\sigma}$, which is annihilated upon photoemission. Thus, the initial state is

$$|\Psi_i\rangle = |\Phi_{GS}; \Phi_{k\sigma}\rangle. \tag{3.6}$$

The final states are many-body eigenstates with two valence holes and one core hole. Final states may be written as

$$|\Psi_f\rangle = \sum_{lm} A_{lm} |\Phi_l; p_m\rangle, \tag{3.7}$$

where $l = 1, 780$ is a sum over the valence configurations, and $m = 1, 6$ is a sum over core states. For photon polarization ϵ, the dipole matrix elements between the initial and final states are

$$M^{kf}_{\epsilon\sigma} = \langle \Psi_i | \hat{T}^k_{\epsilon\sigma} | \Psi_f \rangle, \tag{3.8}$$

where the $\hat{T}^k_{\epsilon\sigma}$ are given by

$$\hat{T}^k_{\epsilon\sigma} = \sum_m \langle \Phi_{k\sigma} | \vec{\epsilon} \cdot \vec{r} | p_m \rangle c^\dagger_{\Phi_{k\sigma}} c_{p_m} = \sum_m \Gamma^{km}_{\epsilon\sigma} c^\dagger_{\Phi_{k\sigma}} c_{p_m}. \tag{3.9}$$

Here, c_{p_m} destroys a core hole p_m, and $c^\dagger_{\Phi_{k\sigma}}$ creates an outgoing photoelectron hole $\Phi_{k\sigma}$. The $\Gamma^{km}_{\epsilon\sigma}$, through k, are functions of the emission angle as well as the channel matrix elements and phase shifts for the $l \pm 1$ partial waves. In this work, we use the values given by Goldberg, Fadley, and Kono [47] calculated for Ni $2p$ emission by 1253.6 eV photons: $R_0 = 1.00$, $R_2 = 4.28$, $\delta_0 = 6.113$, and $\delta_2 = 2.611$.

With an implied sum over the threefold degenerate ground state, the angle-resolved spectrum is written as a sum over all final states:

$$I^k_{\epsilon\sigma} = \sum_f |M^{kf}_{\epsilon\sigma}|^2 \delta(E_f - E_i - \hbar\omega), \tag{3.10}$$

with additional sums over photon polarization ϵ and/or photoelectron spin σ as appropriate. Finally, the lines are Gaussian and Lorentzian broadened to obtain the final spectrum.

3.3 Results and Discussion

In the first section, we consider spin-resolution with unpolarized excitation. Such spectra are useful in understanding the spin-integrated spectra with polarized excitation we consider later. We examine a variety of limiting cases to illustrate the effects of Coulomb repulsion, exchange, and extra-atomic screening. After discussing these effects, we present the theoretical spin-resolved spectra and compare them to recent experimental results [27]. In the following section, we consider circular-polarized excitation with and without spin resolution. We examine how the spin polarization of the levels depends on emission angle and photon helicity. Next, we consider the effect of linear- polarized excitation, with and without spin resolution. We show that MLDAD can be understood as a subtle interplay between exchange and spin-orbit-induced spin polarizations. MUDAD spectra are also presented and discussed. In the last section, we describe a spectral-weight transfer effect which explains the preferential transfer of minority line strength from the satellite to the main lines. This effect, due to extra-atomic screening, is important in understanding the observed spin polarization. Finally, we consider the nature of the final states by plotting the final-state valence configuration, both in real space and in k-space. This allows for a precise description of the physical nature of all features in the spectrum.

3.3.1 Spin-resolved spectra

In Fig. 3.2 we present the spectroscopic arrangement adopted in the theory. The sample is magnetized in the $+z$ direction, meaning that the majority electrons are spin *down*. The photons $\mathbf{q}$ impinge upon the sample in the xz plane, making an angle θ_q with the z axis. Photoelectrons are measured in the xz plane at a takeoff angle θ_k with the z axis as shown.

In order to gain physical insight into the Ni $2p$ spectrum, we examine theoretical spin-resolved spectra for a variety of limiting cases, presented in Fig. 3.3. Lines were narrowly broadened for enhanced spectral detail. All spectra in Fig. 3.3 are for grazing incidence ($\theta_q = 0$) and normal emission ($\theta_k = 90°$).

As a first example, we consider spin-resolved spectra in the limit of zero valence bandwidth and zero core-valence exchange. We obtain this case by setting all the band energies and *pd* exchange terms in Table 3.1 equal to zero. The direct Coulomb term U_{pd}, as well as the *dd* Slater parameters are maintained at their values as given in Table 3.1. Although the spin-orbit interaction can induce a spin polarization even with unpolarized light and in the absence of exchange [57], in the non-chiral geometry considered here such effects are not present. Furthermore, with the *pd* exchange terms equal to zero, there can be no exchange-induced spin polarization either. Therefore the majority and minority spectra are identical for this case, as evident from Fig. 3.3(a).

With zero bandwidth, there can be no intersite valence hopping, and hence no extra-atomic screening. Because the ground state is exactly 50% d^9 and 50% d^{10}, we have equal probabilities of exciting a core electron from a site which *initially* had exactly one or zero valence holes. In addition, since there is no valence hopping, the *final* states must also have either exactly one or zero valence holes. The states with one valence hole are exactly U_{pd} higher in binding energy. Features B and D in Fig. 3.3(a) correspond to the

$2p_{1/2}$ and $2p_{3/2}$ main lines respectively, and are both 100% d^{10} in character. Features A and C are the satellites, occurring U_{pd} eV to the left of the main lines, and are 100% d^9 in character.

As a next example, we consider the limit of zero valence bandwidth as before, except now include the *pd* exchange terms as given in Table 3.1. Though there is still no spin-orbit-induced spin polarization, there can now be exchange-induced spin polarization caused by the magnetized valence band. This results in distinct spectra for minority and majority photoelectrons, as shown in Fig. 3.3(b). The satellites, denoted by A and C, now separate into their characteristic p^5d^9 multiplet structures. The $2p_{3/2}$ satellite contains exactly eight lines, the $2p_{1/2}$ exactly four, each corresponding to atomic multiplets of definite total angular momentum J. Both multiplets are spread over about 3-4 eV. Features B and D in Fig. 3.3(b) correspond to the main lines and are still pure d^{10} in character, and so exhibit no multiplets and no spin polarization. Also, the $2p_{3/2}$ main-line intensity is exactly double the $2p_{1/2}$ main-line intensity in this limit, for both majority and minority spectra. The total satellite intensity, summed over both $2p_{3/2}$ and $2p_{1/2}$ levels, is exactly equal to the total main-line intensity, due to the equal distribution of d^9 and d^{10} in the ground state. However, with *pd* exchange now included, the satellite intensities are no longer equally distributed energetically; the effect of core-valence exchange is to shift the majority (minority) spectrum to higher (lower) binding energy *both within each level and across the levels.* That the majority spectrum is shifted to higher binding *within* each level can be seen qualitatively by comparing the satellites in Fig. 3.3(b) for majority and minority spectra. That the line strength is also shifted *across* the levels is not so obvious by inspection. However, in our calculations we find that the relative intensities of the satellites for the minority spectrum in case (b) is 68% for $2p_{3/2}$ and 32% for $2p_{1/2}$, whereas for the majority spectrum it is 65% and 35% respectively. If there were no mixing between the levels, then the $2p_{3/2}$ to $2p_{1/2}$ satellite

intensity ratio would be fixed at the statistical ratio of 2:1 for both spin channels. This transfer of spectral weight across the levels – a consequence of intra-atomic exchange – is one of the keys to understanding the Ni $2p$ spectra.

This effect can also be seen in other ferromagnetic transition metals. For instance, in both Fe [25] and Co [26], the $2p_{3/2}$ level displays a strong net minority spin polarization, and the $2p_{1/2}$ level a strong net majority spin polarization. Of course, the total spin-up and spin-down intensities, when integrated over *both* levels, should be equal.

In Fig. 3.3(c) we see the effect of introducing a small valence bandwidth, thereby allowing for weak extra-atomic screening. The band energies are set to 50% of their values shown in Table 3.1. In the *initial* state, we have equal probabilities of exciting a core electron from a site which locally d^9 or d^{10}. Upon core-hole creation, a valence electron from a neighboring atom can feel the potential caused by the sudden creation of a core hole at a d^9 site, and hop into the unoccupied valence state on the photoexcited site, thereby screening the core hole and leading to a d^{10} final state. In other words, *the effect of extra-atomic screening is to transfer line strength from the d^9 satellite to the d^{10} main line.* Careful examination shows that this transfer is not uniform throughout the satellite. Rather, satellite final states closer to the main lines transfer more spectral weight than those final states at higher binding energy. This can be seen most clearly by examining the $2p_{3/2}$ majority satellite (feature C) in Fig. 3.3(b), which is dominated by two strong peaks centered about $\sim$ 854 and $\sim$ 857 eV. Both peaks are still clearly visible in Fig. 3.3(c), with weak extra-atomic screening, and now occur at about $\sim$ 855 and $\sim$ 858 eV. However, the low-binding-energy peak, which had a stronger intensity in case (b), now has a weaker intensity in case (c). Because the minority satellite intensity is naturally weighted nearer the main lines, this amounts to a preferential transfer of minority line strength from satellite to main line. This energy-dependent spectral-weight-transfer effect is considered in more detail in section C.

With valence hopping, mixing can occur between the different configurations, and the main line, which is nominally d^{10}, now has some d^9 mixed in. This results in a small exchange-induced spin polarization in the main lines, and also to a very small "exchange splitting" between peak positions for majority and minority main lines [38]. Similarly, the d^9 satellite begins to acquire some d^{10} character, and the multiplet structure, though still clearly apparent in features A and C, begins to blur due to configuration mixing.

It is well known that when a core electron is ejected from a metal, low-energy electron-hole (e/h) pairs can be excited near the Fermi level, leading to asymmetric line shapes [69]. An interesting feature of our model is that we also find such low-energy e/h-pair excitations. This is a consequence of the periodicity imposed on the four-atom cluster, which introduces a k-space and hence a band structure. The excitations can be seen as a small peak just to the left of the main lines at $\sim$ 853 eV in Fig. 3.3(c). These lines are mostly d^{10} in character, and have a high probability of finding one of the X_5 valence holes occupied by an electron from below the Fermi level. When the lines are realistically broadened, these e/h excitations also lead to asymmetric main-line shapes.

In Fig. 3.3(d) we set the one-electron Bloch energies to their full values as given in Table 3.1. As we increase the valence bandwidth, more d^9 configuration is mixed into the main-line states, and we see that the main lines shift slightly to the left. The e/h excitation peak also shifts to higher binding energy; with increasing bandwidth, the energetic cost of promoting an electron from a Bloch state below E_F to an unoccupied X_5 state increases as well. Also, the satellite loses more intensity to the main lines through the increased effectiveness of extra-atomic screening. The multiplet structure is still apparent, though extremely blurred due to increased configuration mixing.

Next we compare the theoretical spin-resolved spectra with experimental results, which were measured by See and Klebanoff [27], and are presented in Fig. 3.4(a). In the experiment, they measured the majority spectrum (e.g., spin up) for a given mag-

netization, and then reversed the magnetization and remeasured the majority spectrum (now spin down). They then averaged over both magnetizations to obtain the resultant majority spectrum. The same was done for the minority spectrum. Experimentally, a majority to minority intensity ratio of $0.93 \pm .03$ eV was found in the $2p_{3/2}$ main line, as well as a small exchange splitting of $\sim .02$ eV between the $2p_{3/2}$ main lines, with the majority spectrum being shifted to higher binding energy. This splitting , though small, proves that the main line cannot correspond to a purely d^{10} final state, which would be intrinsically nonmagnetic. In our calculation, we adopt the same experimental geometry as See and Klebanoff [70], with magnetization $\vec{M} = \pm M\hat{z}$, normal emission ($\mathbf{k} \sim \hat{x}$), and photon wavevector $\mathbf{q} \sim -\hat{x} + \cos 40°\hat{y} - \sin 40°\hat{z}$ (see Fig. 3.2). We also average majority and minority spectra over both magnetizations, and broaden the lines with Gaussian ($\Gamma = 1.6$ eV) and Lorentzian ($\sigma = 1.2$ eV for $2p_{1/2}$ and $\sigma = 0.8$ eV for $2p_{3/2}$) lineshapes [71]. The resulting theoretical spectra are presented in Fig. 3.4(b), and are seen to be in excellent overall agreement with experimental results. The theoretical ratio of majority to minority intensity at the $2p_{3/2}$ main line is found to be 0.96, in agreement with experimental observations. The exchange splitting in the $2p_{3/2}$ main line is found to be 0.032 eV, also consistent with experimental results.

In Fig. 3.4(c) the experimental and theoretical spin polarization (multiplied by a factor of 6 for clarity) is plotted for comparison. Although the differences between majority and minority spectra are quite small, agreement between theoretical and experimental spin polarization is still very good, with theory predicting the correct spin polarization throughout the spectrum. The spin polarization of the spectrum can be understood as a combination of two effects:

(1) The exchange interaction shifts majority line strength to higher binding energy, both *across* and *within* each level.

(2) Extra-atomic screening transfers line strength preferentially from the minority-

dominated low-binding-energy side of the satellites to the main lines.

The two effects *add* in the $2p_{1/2}$ satellite, giving everywhere a majority spin polarization, they *cancel* in the $2p_{1/2}$ main line, leading to near zero spin polarization, they *cancel* in the $2p_{3/2}$ satellite, leading to the observed crossover, and they *add* in the $2p_{3/2}$ main line, leading to a net minority spin polarization.

3.3.2 Magnetic circular dichroism

In Fig. 3.5 we present theoretical spectra calculated for a grazing-angle geometry ($\theta_q = 0$) with right-circular-polarized (RCP) excitation. Fig. 3.5(a) is the spin-integrated spectrum for an electron takeoff angle $\theta_k = 0$ ($\mathbf{k} \parallel \mathbf{q}$), with the corresponding spin-resolved spectra shown below in Fig. 3.5(b). We see that the $2p_{3/2}$ level has a strong spin-down polarization, while the $2p_{1/2}$ level is totally spin up polarized. In fact, exactly 75% of the $2p_{3/2}$ photoelectrons are spin down, and 100% of the $2p_{1/2}$ photoelectrons are spin up. This is a well known fact from atomic physics [72]. For left-circular-polarized (LCP) excitation, the fraction of spin-up and spin-down photoelectrons at each level is exactly reversed, with 100% of the $2p_{1/2}$ photoelectrons being spin down for the same geometry. In Fig. 3.5(c) we present theoretical spectra for RCP excitation at the same grazing angle geometry ($\theta_q = 0$), except now for an electron takeoff angle of $\theta_k = 90°$ (normal emission), with the corresponding spin-resolved spectra shown in Fig. 3.5(d). We see that the spin polarization has reversed from the $\theta_k = 0$ case: now the $2p_{3/2}$ ($2p_{1/2}$) level has a strong spin-up (down) polarization. This example makes clear that, with circular-polarized excitation, changing the position of the electron detector has a drastic effect on the spin-resolved photoemission spectrum.

In Fig. 3.6(a) we present theoretical spectra due to RCP and LCP excitation for normal emission ($\theta_k = 90°$) and grazing-angle geometry ($\theta_q = 0$). For this geometry, we know from above that RCP excitation leads to a strong spin-up (minority) polarization at

$2p_{3/2}$, with LCP leading to an opposite spin polarization. At $2p_{1/2}$ the spin polarizations are reversed. This explains why RCP/LCP resemble minority/majority at $2p_{3/2}$ and majority/minority at $2p_{1/2}$ (compare with Fig. 3.4(b)). In Fig. 3.6(b) we plot the MCD, which we define as $I_{RCP} - I_{LCP}$, multiplied by a factor of 6 for clarity. Comparing the intensity difference of Fig. 3.6(b) to the theoretical spin polarization of Fig. 3.4(c), we see that the two spectra are virtually identical in structure and magnitude, with only a sign change at the $2p_{1/2}$ level due to its reversed spin polarization. These plots reveal the close link between spin resolution with unpolarized excitation and spin integration with circular-polarized excitation.

This relationship is even more explicit in Fig. 3.7, which plots the fractional spin polarization for RCP excitation at grazing incidence, as the emission angle θ_k is swept from 0° to 90°. We see that, as mentioned previously, at $\theta_k = 0°$ the $2p_{1/2}$ level is 100% spin-up polarized, whereas the $2p_{3/2}$ photoelectrons are exactly 75% spin down and 25% spin up. As we increase the emission angle, the spin polarization changes, resulting in a strong spin-down (spin-up) polarization for the $2p_{1/2}$ ($2p_{3/2}$) level at normal emission ($\theta_k = 90°$). Again, for LCP excitation the spin polarizations are exactly reversed. At some intermediate "crossover" angle, the photoelectrons from both levels will be exactly 50% spin up and 50% spin down. This occurs at $\sim 31°$ for the case of Ni. At this angle, the MCD is found to vanish *over the entire spectrum*; i.e., the spectra due to RCP and LCP excitation are identical. For grazing-angle excitation, the "crossover" angle occurs at:

$$\cos^2\theta_c = \frac{2R_2^2 - R_0^2 + R_0R_2\ \cos(\delta_2 - \delta_0)}{3(R_2^2 + R_0R_2\ \cos(\delta_2 - \delta_0))}, \tag{3.11}$$

where R_0 and R_2 are the radial matrix elements for the $l = 0$ and $l = 2$ spherical waves, and δ_0 and δ_2 are the respective phase shifts [47]. Measuring the crossover angle experimentally could give information on the radial matrix elements and phase shifts. The phase shifts are important because, in the absence of diffraction [34], they

determine the sign of dichroism with linear or unpolarized light, as discussed below. We have investigated such crossover angles for nongrazing geometries, and find that such angles also exist. The MCD is expected to vanish at these angles. It should be stressed that photoelectron diffraction effects can also give rise to dichroisms and could therefore alter these results, unless a suitable geometry can be chosen such that the diffraction contribution to the MCD vanishes.

3.3.3 Magnetic linear and unpolarized dichroism in the angular distribution

MCD can be understood as a consequence of preferential emission of a given spin component upon circular-polarized excitation. The origin of MLDAD is more subtle, involving an interplay between spin-orbit and exchange-induced spin polarizations. In a typical MLDAD experiment, one excites the sample using p-polarized light impinging at $\theta_q = 90°$ with $\mathbf{q} \sim \hat{y} - \hat{x}$ (see Fig. 3.2). The spin-integrated spectrum is measured for normal emission $\mathbf{k} \sim \hat{x}$, with magnetization $\vec{M} = M\hat{z}$. The magnetization direction is then reversed, and the spectrum remeasured. The two spectra are subtracted to obtain the magnetic dichroism.

In the absence of photoelectron diffraction [34], MLDAD is caused by cross-channel interference between the $l \pm 1$ channels, which, in the presence of spin-orbit coupling, can induce spin polarizations. This is apparent from Fig. 3.8(a) and 3.8(b), which contains the spin-resolved spectra for magnetizations along the $\pm z$ directions ($M \uparrow$ and $M \downarrow$, respectively), for the geometry described above. In this example, the valence bandwidth is set to zero to eliminate extra-atomic screening effects. In Fig. 3.8(c) the spin polarization, $I_{up} - I_{down}$, is plotted. This example is illustrative because it allows for a clearer separation of spin-orbit and exchange-induced spin polarizations. With zero valence bandwidth, the main lines are pure d^{10} in character, and hence cannot experience

any exchange-induced spin polarization. We see that for either magnetization, the $2p_{3/2}$ main line has a net spin-down polarization, while the $2p_{1/2}$ main line has a net spin-up polarization. The effect of spin-orbit coupling with cross-channel interference, therefore, is to induce a spin polarization at one level and an opposite spin polarization at the other level, *independent of magnetization.* The effect of exchange-induced spin polarization is to shift the majority spectrum to higher binding energy and the minority spectrum to lower binding energy for the d^9 satellites. For $M\uparrow$, the majority electrons are spin down, and so the spin polarization exhibits an overall -/+ feature at both satellites. For $M\downarrow$, the exchange dominated satellite spin polarization is largely reversed, now exhibiting an overall +/- feature at both levels.

In Fig. 3.9 we present the same spin-resolved spectra using p-polarized excitation for $M\uparrow$ and $M\downarrow$, except now with realistic broadening and full valence bandwidth to account for extra-atomic screening. With valence hopping, the main lines acquire some d^9 character which allows for a small exchange-induced spin polarization. However, the spin-orbit-induced spin polarization still dominates, as evident by the fact that the $2p_{3/2}$ main line still has a spin-down polarization and the $2p_{1/2}$ main line a spin-up polarization. The satellites, largely d^9 in character, are dominated by exchange-induced spin polarization. However, spin-orbit-induced spin polarization is still apparent. For example, exchange and spin-orbit *both* enhance the spin-up intensity in the $2p_{1/2}$ satellite for $M\downarrow$, leading to a very strong spin-up polarization. For $M\uparrow$, on the other hand, exchange effects enhance the spin- down character of the $2p_{1/2}$ satellite, while spin-orbit enhances the spin-up character. The two effects tend to cancel, leading to only a very weak spin polarization for the $2p_{1/2}$ satellite. Analogous arguments could be used to explain the spin polarizations of the $2p_{3/2}$ satellites.

The origin of such MLDAD is now clear: If there were no spin-orbit-induced spin polarization, then the spin-up intensity for $M\uparrow$ would exactly equal the spin-down

intensity for $M \downarrow$, and spin-up intensity for $M \downarrow$ would exactly equal spin-down intensity for $M \uparrow$. The spin-integrated intensities for either magnetization would then be exactly equal, and there would be no dichroism. Spin-orbit-induced spin-polarization breaks this symmetry.

In Fig. 3.10(a) we present theoretical spin-integrated spectra using p-polarized light in the same MLDAD geometry described above, for magnetizations $M \uparrow$ and $M \downarrow$. In Fig. 3.10(b) we present the MLDAD, which we define as $I_{M\downarrow} - I_{M\uparrow}$. In a previous work [38], we calculated the MCD according to $(I^{RCP} - I^{LCP})/(I^{RCP} + I^{LCP})$. However, to avoid an energy-dependent normalization factor, it is more natural to define the MCD simply as the difference spectrum $I^{RCP} - I^{LCP}$. With the MCD defined in this way, we find that the MCD signal, as a fraction of the peak intensity, is much larger than the corresponding MLDAD signal. However, the *lineshapes* are identical. This is because both difference spectra in fact measure the same fundamental spectrum I^1, as discussed by Thole and van der Laan [48, 73].

Two points should be stressed here:

(1) Special attention should be given regarding the *sign* of the dichroism. In the absence of diffraction, MLDAD is caused by cross-channel interference and the sign of the dichroism varies as $\sin(\delta_2 - \delta_0)$. The spin-orbit- induced spin polarization reverses sign as the phase difference passes through 0 or π. In other words, for different partial-wave phase shifts we may find opposite spin-orbit-induced spin polarizations from those described above. Therefore, measuring the *sign* of this dichroism would provide information on the phase shifts.

(2) It was shown by Fanelsa *et al.* [34] that scattering off the lattice (diffraction) can induce dichroisms even larger than those due to cross-channel interference. This effect must be taken into account when analyzing the *sign* of the dichroism, although it is possible that such effects may not alter the MLDAD *lineshape*.

We have seen that linear p-polarized radiation leads to a magnetic dichroism upon reversal of the magnetization, and that this dichroism measures the same fundamental spectrum as MCD. By symmetry, excitation by linear s-polarized light does not lead to such dichroism. However, unpolarized light is an incoherent superposition of s and p, and the p-component should lead naturally to dichroism as before.

In Fig. 3.11 we present theoretical spin-integrated spectra using unpolarized excitation for magnetic orientations $M \uparrow$ and $M \downarrow$, along with the corresponding (MUDAD) dichroism. The geometry is the same as the MLDAD geometry described above, and the spectra were normalized such that the photoemission intensity derived from the p-polarized component was the same in both cases. For such a normalization, we see that the difference spectrum of Fig. 3.11(b) is exactly the same as that of Fig. 3.10(b). However, due to the intensity contribution from the non-dichroic s-component, the percent asymmetry is less than with linear p-polarized light. The MUDAD, while being less than the MLDAD, is *not* exactly one-half as large as commonly believed. The reason for this is that the photoemission intensity derived from the s-polarized component is not equal to the photoemission intensity derived from the p-polarized component. In fact, for the phase shifts and geometry considered here, the ratio of p-derived to s-derived intensity is about 9:2. It should be mentioned that this ratio depends sensitively on the phase differences between the $l \pm 1$ channels. For zero phase difference, the intensity ratio drops to 3:2. Measuring this intensity ratio with linear-polarized synchrotron radiation also could yield information on the partial-wave phase shifts for the solid state.

As a final example of such MUDAD effects, we return to the SRXPS results of See and Klebanoff [27], for which the experimental geometry was already described. See and Klebanoff averaged the majority and minority spectra over both magnetic orientations, as discussed above. The purpose here is to investigate the spin-resolved spectra for *each* magnetic orientation. In Fig. 3.12(a) and 3.12(b) we present theoretical spin-

resolved spectra for $M \uparrow$ and $M \downarrow$ respectively. We see significant differences in the spin-polarization for the two orientations. For instance, the $2p_{3/2}$ main line has a strong minority-spin polarization for $M \downarrow$, but a small majority-spin polarization for $M \uparrow$. The sign of the $2p_{1/2}$ main-line spin polarization also depends on the magnetic orientation. The majority and minority spectra, averaged over both magnetizations, were presented already in Fig. 3.4(b), and are reproduced here in Fig. 3.12(c) for convenience.

3.3.4 Nature of the final state

In this section we investigate in greater detail the effects of electron-electron interaction and the nature of the final state. In Fig. 3.13 we consider the case of photoemission from a structureless core level, obtained by setting all of the *pd* exchange integrals to zero. The *dd* Slater parameters and the valence-band Bloch energies are set to their full values as given in Table 3.1. Each spectrum in this limit contains six features: the $2p_{3/2}$ main line ($\sim$ 852 eV), the $2p_{3/2}$ e/h pair excitation ($\sim$ 854 eV), the $2p_{3/2}$ satellite (as indicated by the arrows), and the corresponding features for the $2p_{1/2}$ level. We consider a grazing-angle geometry ($\theta_q = 0$) and normal emission, so that there is no spin-orbit-induced spin polarization. Since there can be no exchange-induced spin polarization either, the spin-up and spin-down intensities are equal. The analysis is further simplified because the satellites are reduced to single peaks. In Fig. 3.13 we plot the photoemission spectra as we progressively decrease the direct Coulomb repulsion U_{pd} from 5 eV to 2 eV. Reducing U_{pd} reduces the energetic cost of leaving the core hole unscreened, and the satellite position moves in toward the main lines, as shown. The satellite position is always more than U_{pd} eV to the left of the main lines because the localized valence hole, viewed in k-space, contains sizable components of higher-energy single-particle Bloch states. What is surprising is that the intensity of the satellite decreases so dramatically as the satellite moves in closer to the main lines. This intensity

loss in the satellite translates into an intensity *gain* for the main line. In other words, the effect of extra-atomic screening is to selectively transfer spectral weight from the low-binding-energy satellite states to the main lines. This effect is a fundamental feature of the Ni $2p$ photoemission spectrum, and is not an artifact of the structureless core considered here. This is most apparent by comparing the $2p_{3/2}$ majority satellite for the case of zero bandwidth and 50% bandwidth (shown as feature C in Fig. 3.3), as discussed in section A. In particular, this extra-atomic screening effect explains why there is a preferential transfer of minority line strength from the satellite to the main lines: the minority satellite intensity is naturally weighted nearer the main lines by intra-atomic exchange, and therefore transfers a greater proportion of its intensity to the main lines.

The e/h excitation appears as a distinct peak approximately 2 eV to the left of the main lines for all values of U_{pd} considered in Fig. 3.13. That the peak position is energetically fixed is reasonable because the e/h pair, viewed in k-space, involves promotion of electrons from states below E_F to unoccupied states at or near E_F. The energetic cost of doing this depends on the valence band structure, and the energies of the single-particle Bloch states do not change as we vary U_{pd}. Interestingly, for the physically realistic range of core-valence repulsion considered here, the *intensity* of the e/h excitation is largely independent of U_{pd}.

It should be emphasized that the e/h pair excitation appearing as a single peak in our spectra is purely an artifact of the model. This is a consequence of our Brillouin zone, which consists of Γ and the three X points. Exciting an electron from below E_F to a hole at or near E_F costs a discrete amount of energy in our model, due to the discrete nature of our Brillouin zone. In a realistic system, there is no energy gap at E_F and the e/h excitations can be of arbitrarily small energy. This leads to the classic asymmetric line shapes in core-level photoemission from metals, as described by Doniach and Šunjić[69].

For realistic broadening, however, the e/h excitation peak in our spectrum "gets buried" into the main line, and manifests itself also as an asymmetry in the main lines. While not leading to a continuous tail, it is remarkable that a simple four-atom cluster with periodic boundary conditions contains such excitations, which are a truly solid-state effect.

In Fig. 3.14 we plot the satellite intensity as a function of U_{pd} for the same limiting case considered in Fig. 3.13. The dramatic intensity drop with decreasing U_{pd} is purely an extra-atomic screening effect. For zero valence bandwidth, the satellite strength would always be exactly 50% (due to our ground state) and would always occur exactly U_{pd} to the left of the main lines. Since satellite position is roughly proportional to U_{pd}, the essential result of this plot is that the effect of extra-atomic screening is to dramatically dampen those satellite final states whose energetic position is nearer the main lines.

This binding-energy-dependent spectral-weight-transfer effect may also explain the lack of any observable minority component in the Ni 3s satellite [27]. Assuming for a moment zero valence bandwidth, and using our ground state (50% d^9 and 50% d^{10}), the majority Ni 3s spectrum would consist of three peaks: a main line of relative strength 2, and two satellite peaks, each of relative strength 1, corresponding to ^1D and ^3D final states. The minority spectrum would consist of two peaks: a main line of relative strength 2, and a satellite, corresponding to a ^3D final state, also of strength 2. The main line occurs at about 110 eV binding energy. If one now allows for extra-atomic screening by introducing a valence bandwidth, satellite line strength will be transferred to the main lines. If we assume that the triplet peak occurs at $\sim$ 113 eV binding energy and that the singlet peak occurs at $\sim$ 116 eV, then we can see from Fig. 3.14 that the triplet peak, which has minority character, would transfer its intensity almost completely to the main lines, which would then acquire minority character. Any residual

satellite triplet strength would be buried by the main lines, and the only satellite peak to survive in substantial strength would be the high binding energy singlet final state, leading to an apparent pure majority spin polarization for the 6-eV satellite, as observed experimentally [27].

Next we examine quantitatively the nature of the final state, both from a localized (real space) perspective, and also from a band-structure (k-space) point of view. In the former approach, it has been argued for some time that the main lines correspond to d^{10} final states, and the satellites to d^9 final states. However, See and Klebanoff measured a small exchange splitting in the Ni $2p$ main lines[55], thereby proving that the main lines could not be pure d^{10}. However, until now, quantitative descriptions of the main-line final-state configurations have not been reported. Also, the possibility of significant d^{10} mixing in the nominally d^9 satellite has not been investigated in detail.

In Fig. 3.15(a) we present a plot of the spin-integrated Ni $2p$ photoemission spectrum, with the fraction of local d^{10}, d^9, and d^8 configuration in the final states plotted below. We see that the main lines are not pure d^{10}, but have roughly 10% of d^9 configuration mixed in. This small d^9 hybridization in the nominally d^{10} main line explains the small exchange splitting observed experimentally. The e/h excitation, occurring at $\sim$ 854 eV for $2p_{3/2}$, also corresponds to a primarily d^{10} final state. The satellite, however, is found to contain a surprisingly large amount of d^{10} mixing in the final state. At the high-binding-energy side of the satellite, the d^{10} mixing is about 30%, but rises to nearly 50% at the low-binding-energy side. The d^8 final states (two valence holes on the core hole site) are found to occur approximately 10-15 eV to the left of the main lines and are not excited. It should be remarked that had our ground state contained a small amount of d^8 configuration, then we would have had a small probability of exciting these final states, leading to a very weak 14-eV satellite, as found experimentally [27] and predicted theoretically using an Anderson impurity model with such d^8 mixing [74].

Recently there has been speculation that the Ni core-level 6-eV satellites may actually correspond to d^8 final states [27, 55]. The reasoning behind this was that the observed spin polarization of the Ni $3s$ 6-eV satellite was believed to be inconsistent with the mixed spin polarization expected for a satellite corresponding to an s^1d^9 configuration. However, we believe that the extra-atomic screening effects described above resolve this apparent discrepancy and are consistent with the observed spin polarizations of both the Ni $3s$ satellites and main lines. Our main-line (nominally d^{10}) and satellite (nominally d^9) final-state assignments are also consistent with other theoretical descriptions based on an Anderson impurity model [37].

Finally, we consider the nature of the final-state configuration from a k-space point of view. In Fig. 3.16 we plot the Bloch-state decomposition for main-line, e/h pair, and satellite final states. For any final state, the number of valence holes, summed over all Bloch states, must equal two. In the ground state, both holes are in X_5. If there were no interaction between the core hole and the valence band, then there would be no rearrangement of the valence charges upon photoemission, and both holes in the final state would remain in X_5. For the main-line states, we see that there is a small rearrangement of the valence charges. However, about 90% of the valence holes still remain at (X_5) or near (X_2) the Fermi level.

For the e/h pair excitations, we see a substantial rearrangement of the valence charges, with a high probability of exciting "shakeup" electrons from either Γ'_{25} or X_3, which are both located well below E_F.

For the satellite, we see an almost uniform distribution of valence configurations in k-space. This is a reflection of the fact that the natural language for describing the satellite is the localized basis. There are more holes at X_5, but that is partly due to the fact that, statistically, there are simply more of these states; X_5 is a six-dimensional irreducible representation, while the other representations are of dimension two or three.

3.3.5 Conclusion

We have calculated Ni $2p$ spin-integrated and spin-resolved photoemission spectra for a variety of cases, including circular, linear, and unpolarized excitation. We have emphasized the subtle interplay between Coulomb, exchange, spin-orbit, and extra-atomic screening effects. We have also described an energy-dependent spectral-weight-transfer effect, which can also explain the spin polarization of the Ni $3s$ spectrum. Finally, we discussed the nature of the final state, showing that main lines have a small d^9 mixing, and that the satellite has a substantial d^{10} component.

Table 3.1: Slater integrals and spin-averaged band energies used in this work.

Integral	Energy (eV)	Bloch State	Energy (eV)
U_{dd}	3.0	Γ_{12}	0.92
F^2_{dd}	9.79	Γ'_{25}	2.04
F^4_{dd}	6.08	X_1	4.31
U_{pd}	4.0	X_2	0.18
G^1_{pd}	4.63	X_3	3.81
F^2_{pd}	6.18	X_5	0.0
G^3_{pd}	2.63		

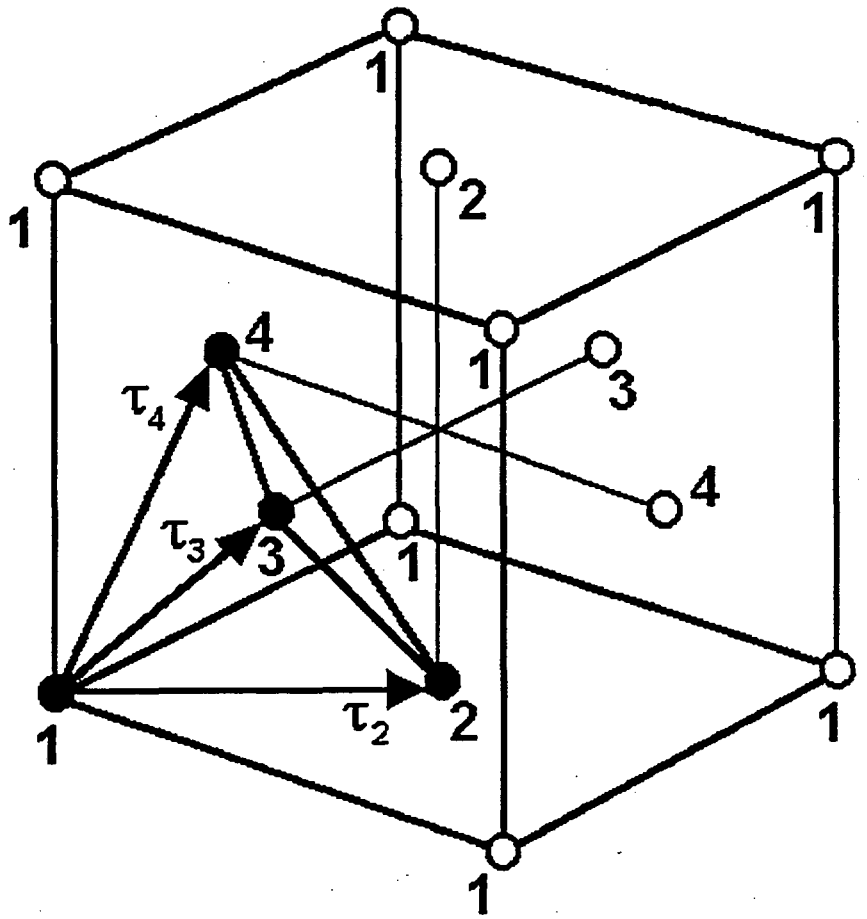

Figure 3.1: The model. Periodic boundary conditions are imposed on the small tetrahedral cluster of four atoms (black circles) to generate the full *fcc* lattice. Each atom is labeled by an index 1-4, and each is surrounded by twelve nearest neighbors of a different index. The four translations that leave the crystal invariant are $\vec{0}$, $\vec{\tau_2}$,$\vec{\tau_3}$, and $\vec{\tau_4}$, where $\vec{0}$ is the identity translation.

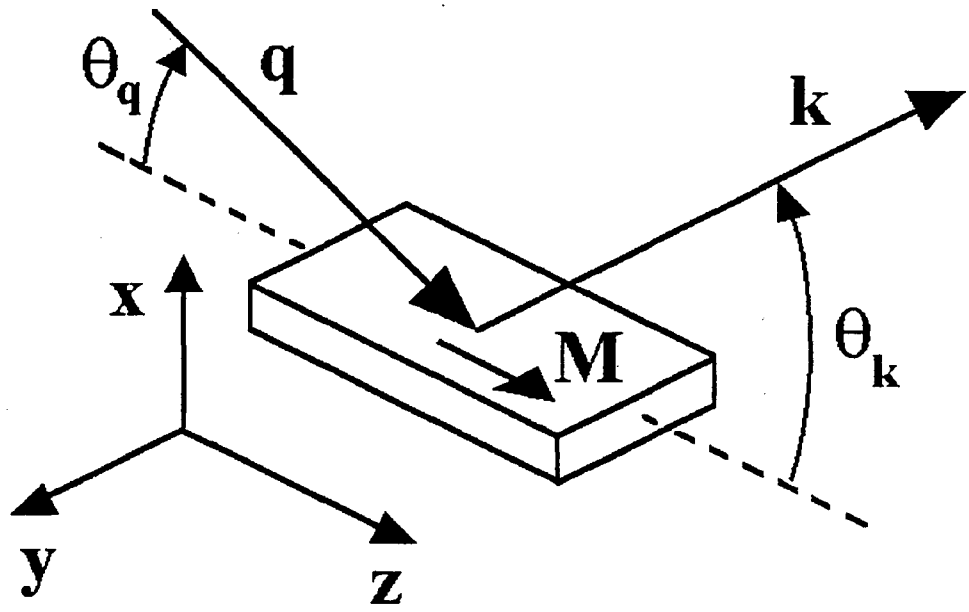

Figure 3.2: Definition of the geometry. The incident photons **q** make an angle θ_q with the magnetization direction, which is in plane along the z axis. The electrons **k** are emitted at a takeoff angle θ_k with respect to the z axis.

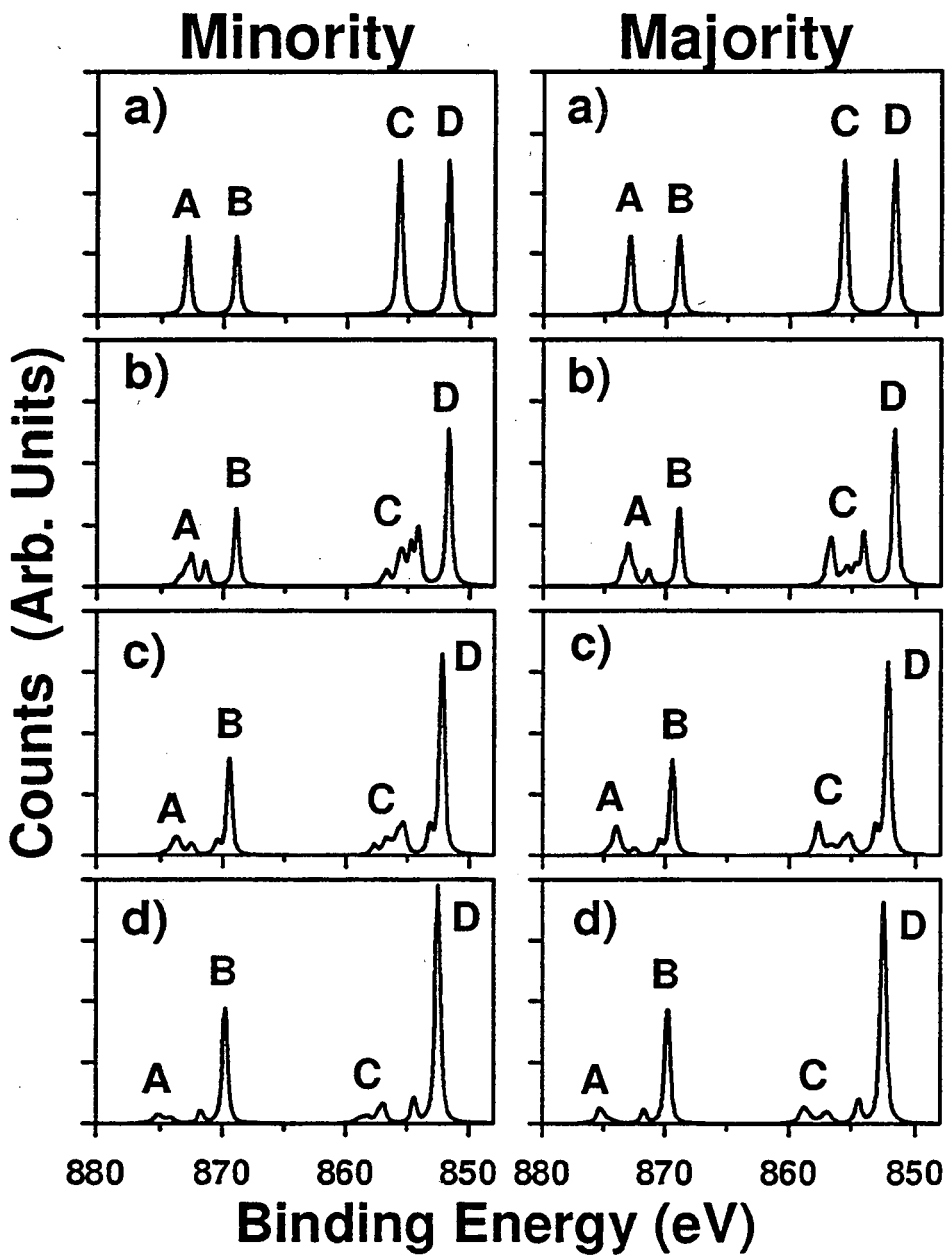

Figure 3.3: Majority and minority photoelectron spectra. All lines were Gaussian (Γ = 0.3 eV) and Lorentzian (σ = 0.3 eV) broadened. (a) Spectra for zero valence bandwidth and zero exchange interaction between core hole and valence states. (b) Spectra for zero valence bandwidth, now including core-valence exchange. (c) Spectra, including core-valence exchange, for 50% valence bandwidth. (d) Spectra for full Ni valence bandwidth.

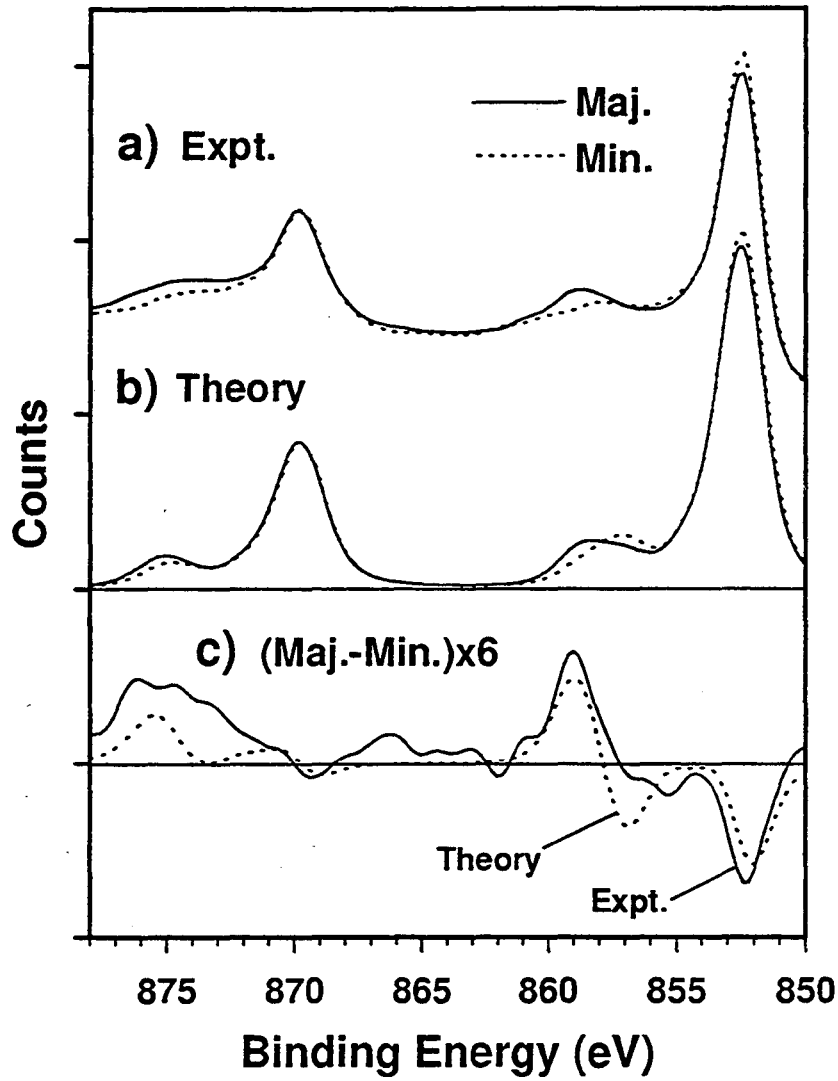

Figure 3.4: Ni $2p$ spin-resolved experimental and theoretical results. (a) Experimental results. (b) Theoretical results, convoluted with a Gaussian ($\Gamma = 1.6$ eV) and Lorentzian ($\sigma = 0.8$ eV and 1.2 eV for $2p_{3/2}$ and $2p_{1/2}$, respectively). (c) Difference of majority and minority spectra for theoretical (dashed lines) and experimental (solid lines) results, both multiplied by 6 for clarity.

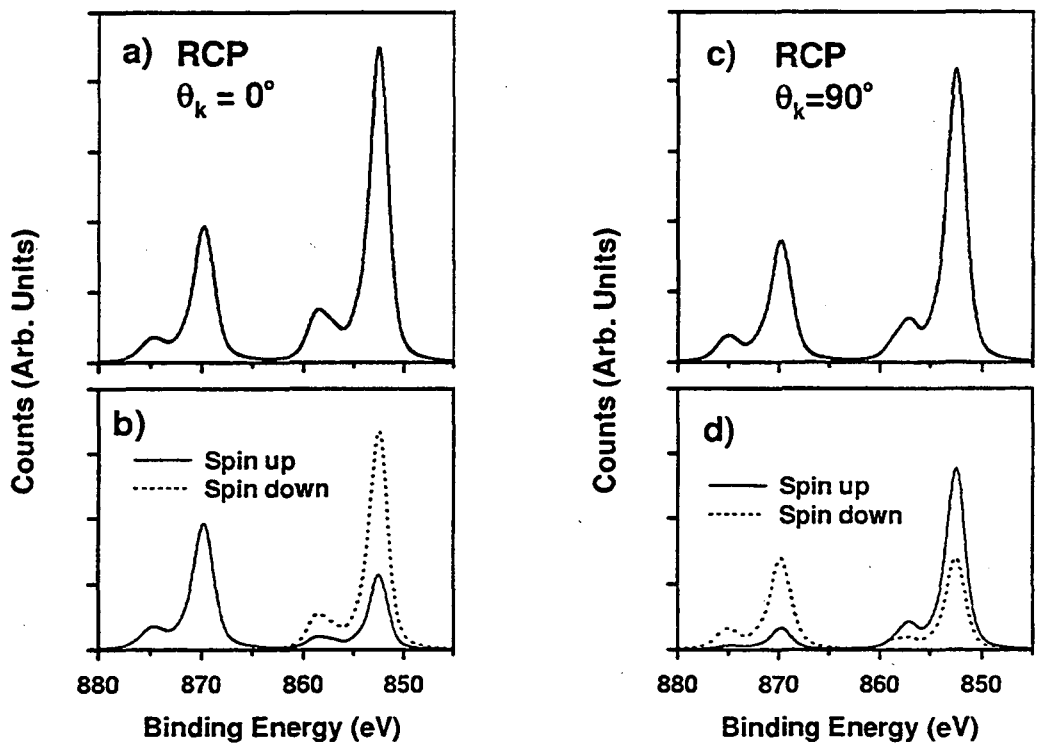

Figure 3.5: Spin-integrated and spin-resolved spectra for RCP excitation at grazing incidence ($\theta_q = 0$). For LCP excitation, the spin polarization is reversed. (a) Spin-integrated intensity for $\theta_k = 0$ takeoff angle. (b) Corresponding spin-resolved spectra. The $2p_{3/2}$ photoelectrons are 75% spin down and 25% spin up. The $2p_{1/2}$ photoelectrons are 100% spin up. (c) Spin-integrated intensity for normal emission ($\theta_k = 90$). (d) Corresponding spin-resolved spectra. Here the $2p_{3/2}$ ($2p_{1/2}$) level has a strong spin-up (down) character.

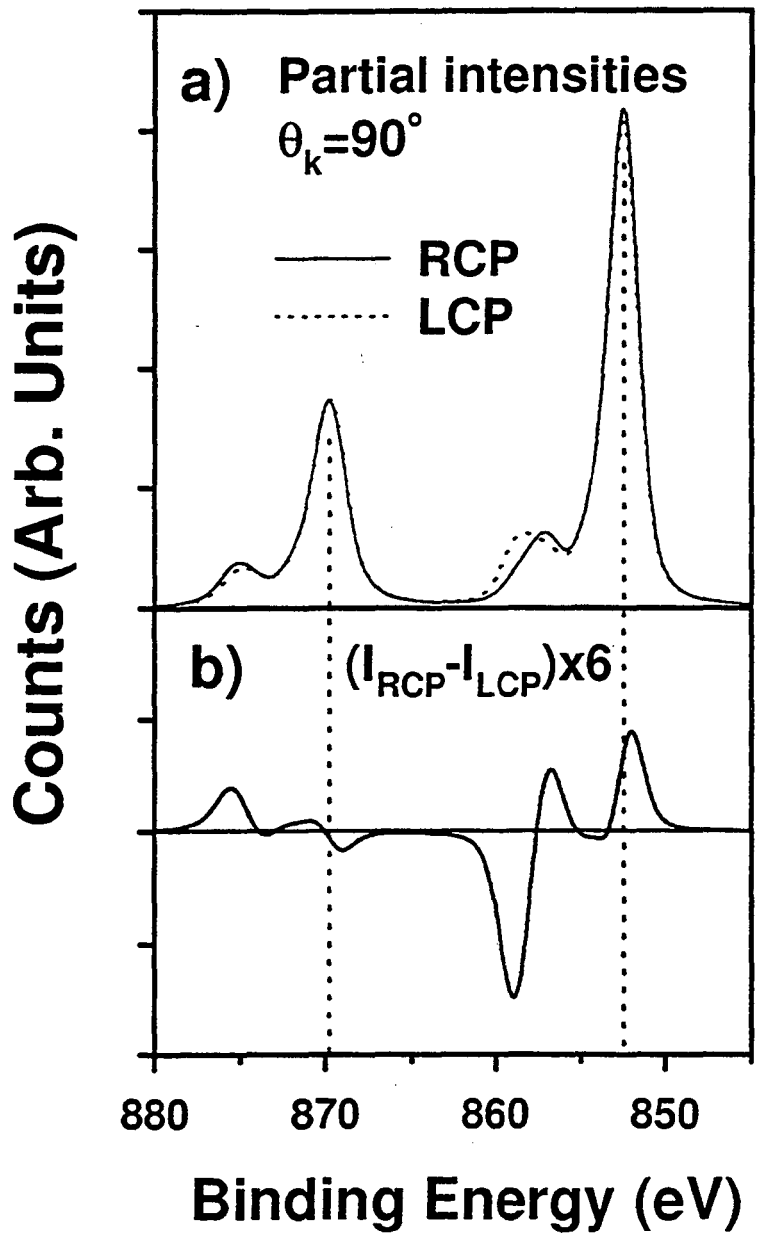

Figure 3.6: Magnetic circular dichroism for grazing incidence ($\theta_q = 0°$) and normal emission ($\theta_k = 90°$). (a) Partial intensities for RCP and LCP excitation. (b) MCD difference spectrum, multiplied by 6 for clarity.

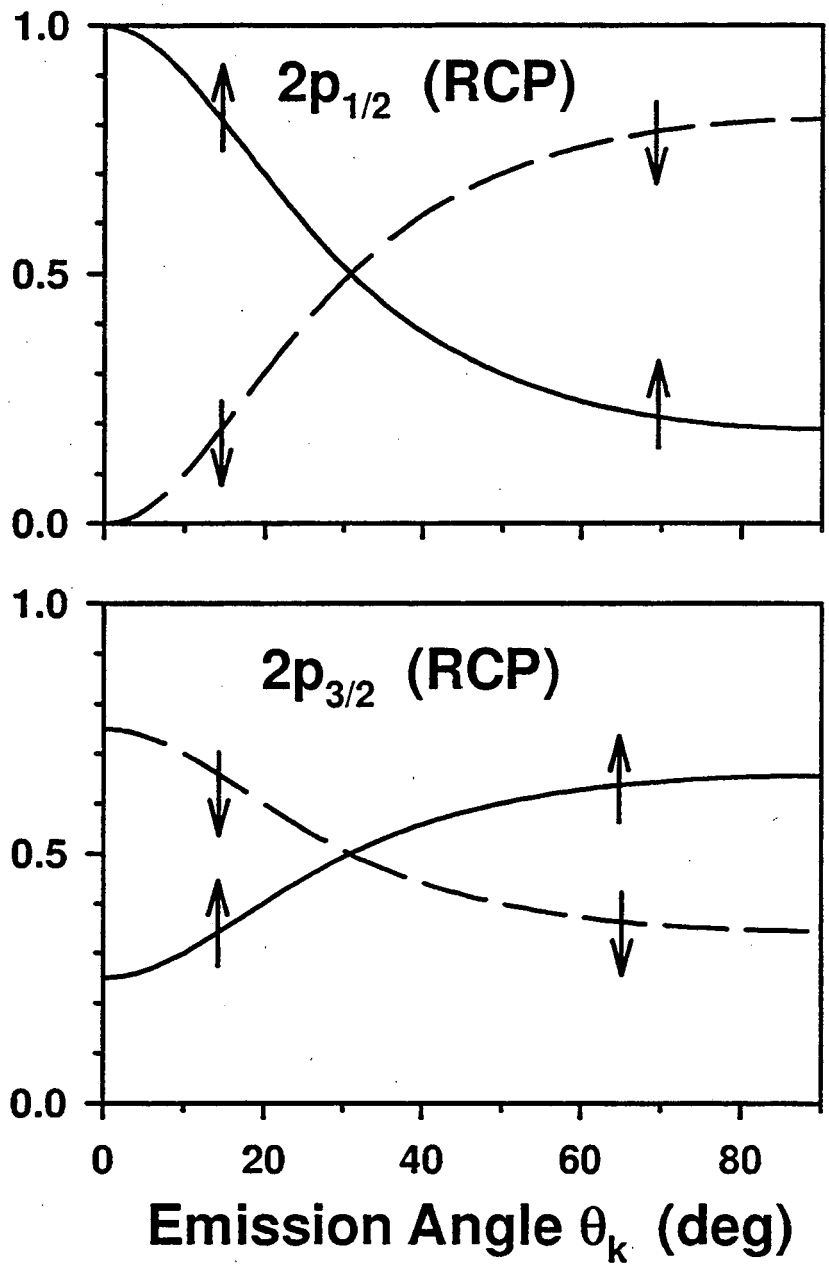

Figure 3.7: Fractional spin polarization at grazing incidence ($\theta_q = 0°$) for RCP excitation. For LCP, the spin polarization is exactly reversed. At approximately 31°, equal numbers of spin-up and spin-down electrons are ejected from each level. At this angle, the MCD is predicted to vanish throughout the spectrum.

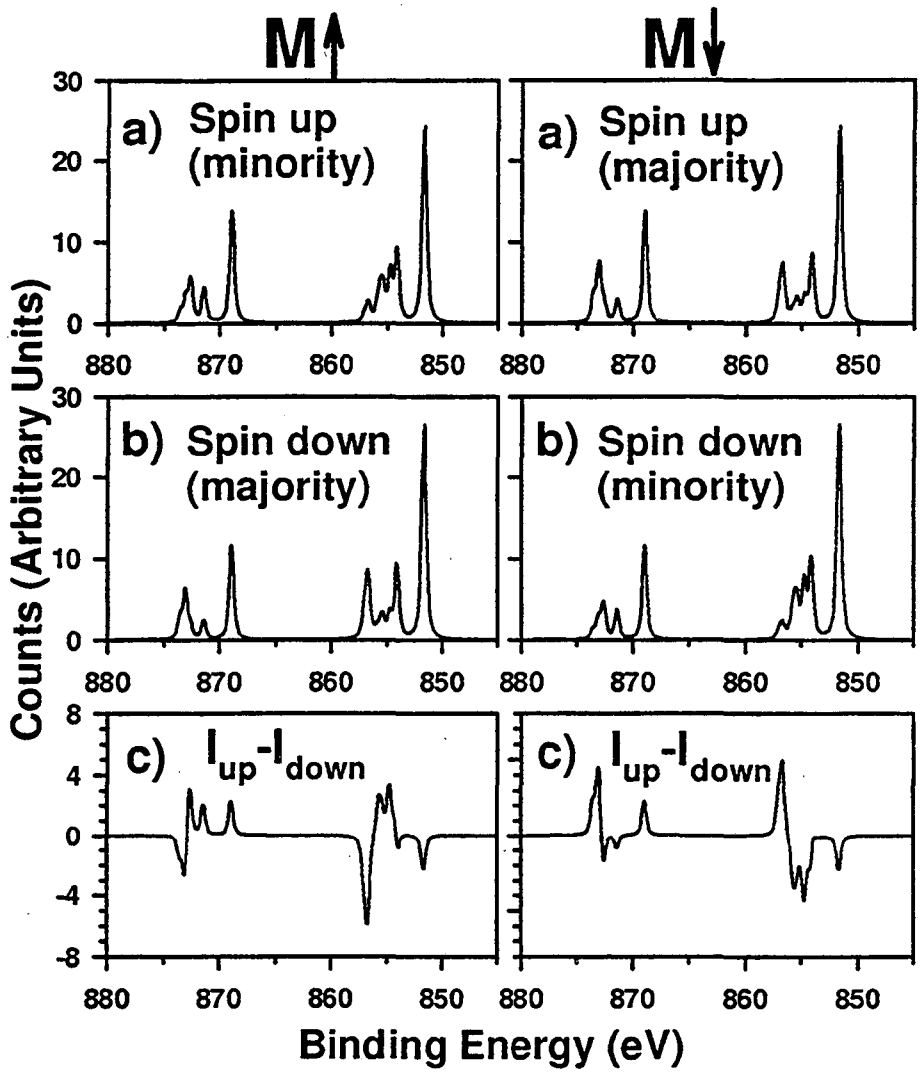

Figure 3.8: Spin-resolved spectra in the zero bandwidth limit using linear p-polarized excitation, for geometry described in text. All lines were narrowly broadened with a Gaussian ($\Gamma = 0.3$ eV) and Lorentzian ($\sigma = 0.3$ eV). (a) Spin-up intensities for magnetization along $+z$ and $-z$ respectively. (b) Spin-down intensities for magnetization along $+z$ and $-z$, respectively. (c) Spin polarization. The $2p_{3/2}$ main line is polarized spin down, whereas the $2p_{1/2}$ main line is polarized spin up, independent of magnetization. The main-line spin polarization is due exclusively to spin-orbit and cross-channel interference. The spin polarization of the satellites is dominated by the exchange interaction.

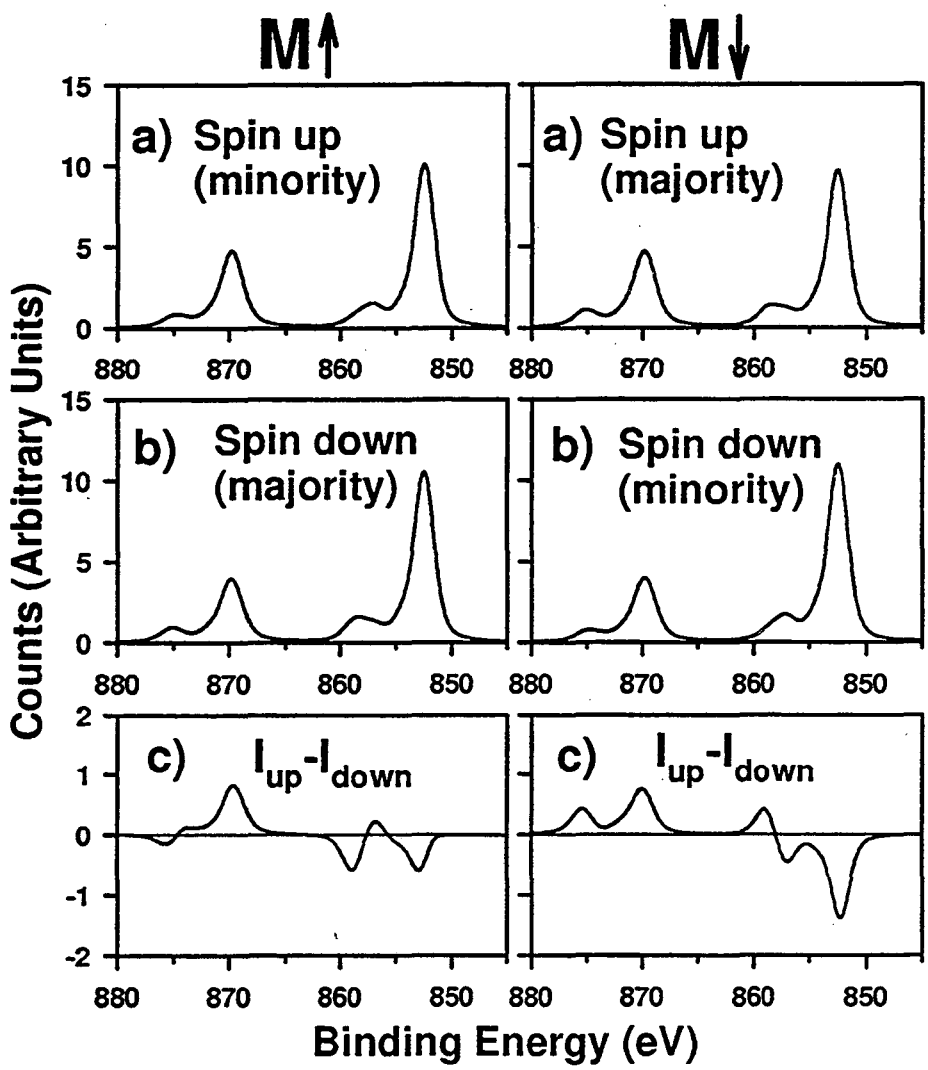

Figure 3.9: Spin-resolved spectra using true valence bandwidth with linear p-polarized excitation, for geometry described in text. Lines convoluted with a Gaussian (Γ = 1.6 eV) and Lorentzian (σ = 0.8 eV and 1.2 eV for $2p_{3/2}$ and $2p_{1/2}$, respectively). (a) Spin-up intensities for magnetization along $+z$ and $-z$ respectively. (b) Corresponding spin-down intensities. (c) Spin polarization for $+z$ and $-z$ magnetizations. Main lines display a spin polarization due to spin-orbit (small exchange), but the satellite spin polarization is due mainly to exchange (due to larger exchange effects present there).

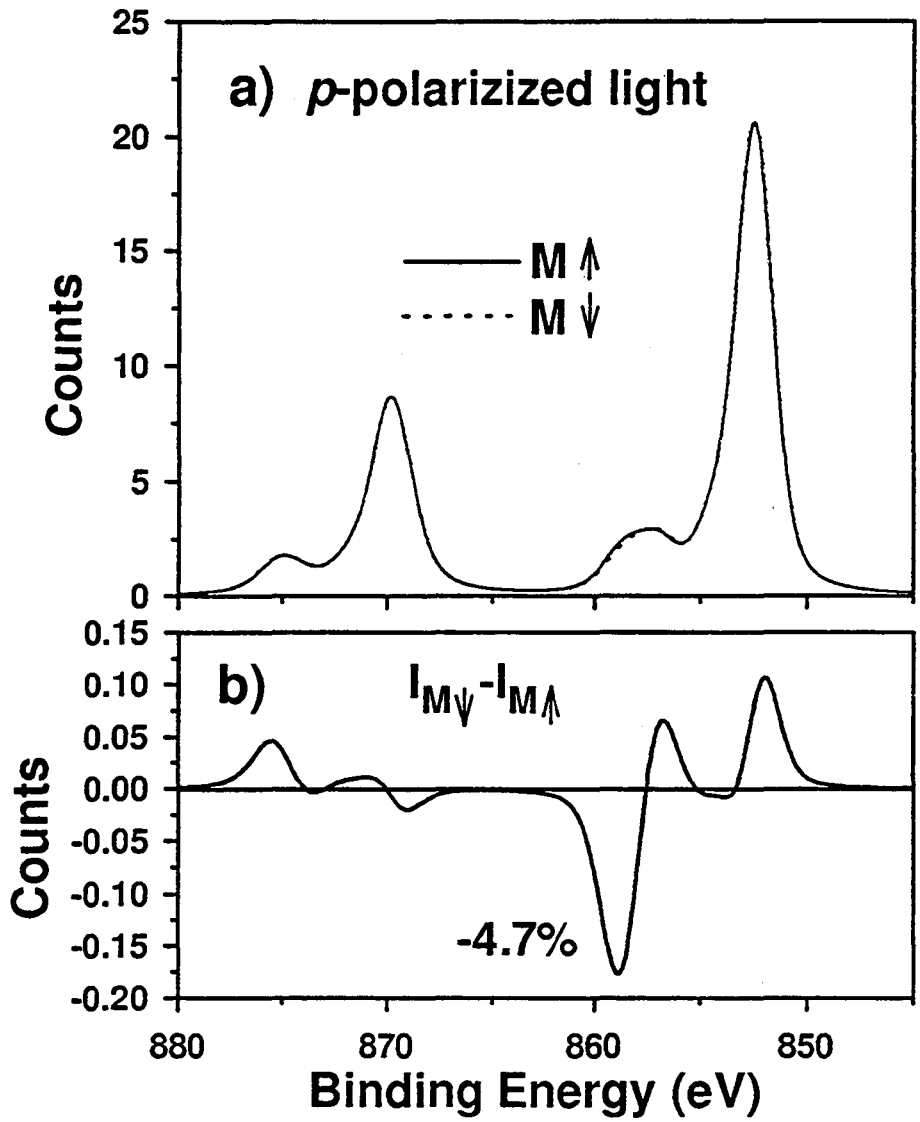

Figure 3.10: MLDAD for geometry described in text. (a) Spin-integrated intensities for magnetization along $+z$ and $-z$ respectively. (b) MLDAD difference spectrum. Except for the reduced magnitude, the spectrum is identical to the MCD spectrum presented above.

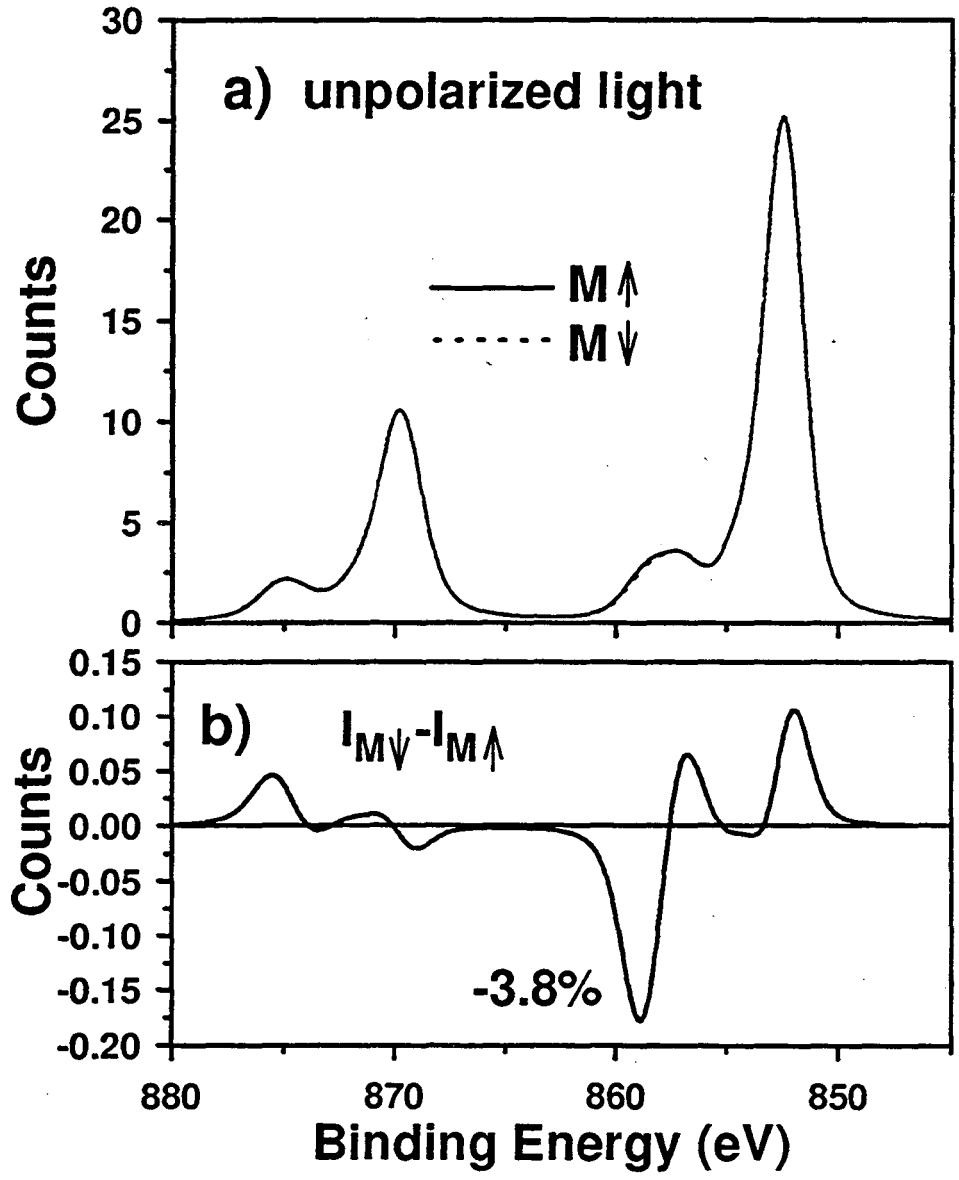

Figure 3.11: MUDAD for geometry described in text. (a) Spin-integrated intensities for magnetization along $+z$ and $-z$ respectively. (b) Unnormalized MUDAD spectrum. The lineshape is identical to the MLDAD spectrum, but slightly smaller in magnitude due to the non-dichroic component derived from s-polarized photons.

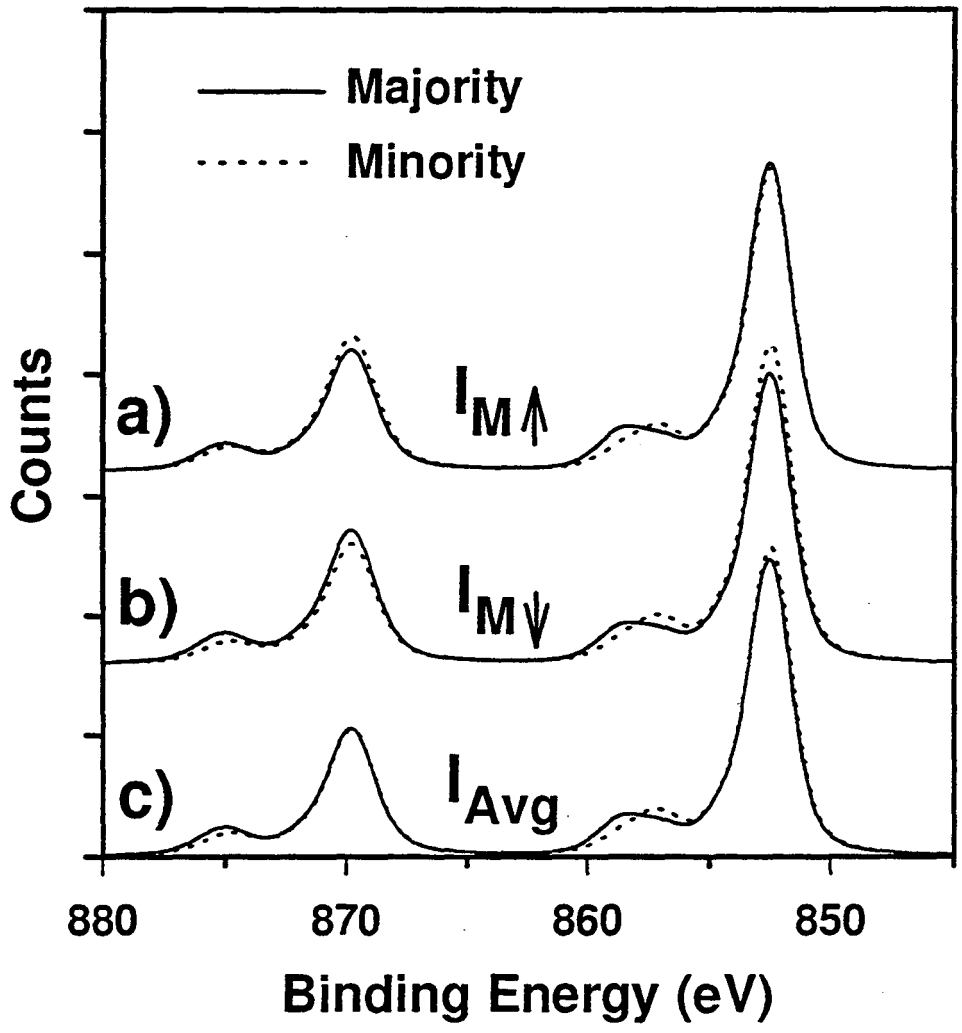

Figure 3.12: Spin-resolved spectra using unpolarized excitation for experimental geometry described in text. (a) Majority and minority spectra for $M\uparrow$. (b) Majority and minority spectra for $M\downarrow$. (c) Majority and minority spectra, averaged over both magnetizations.

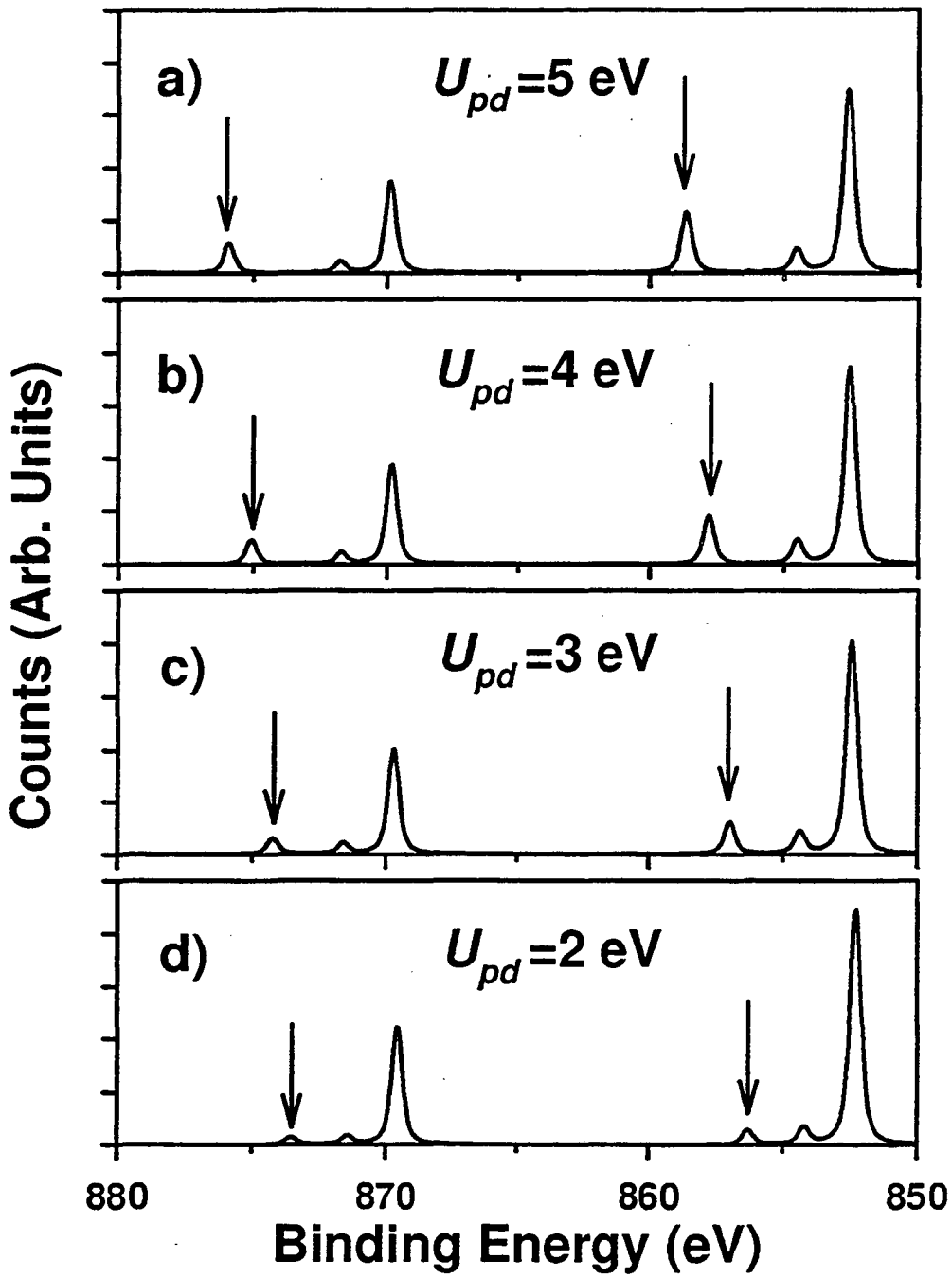

Figure 3.13: Ni $2p$ photoemission spectra at full valence bandwidth setting exchange integrals to zero. (a)-(d) Spectra for $U_{pd} = 5, 4, 3,$ and 2 eV respectively. As the satellite lines move to lower binding energy, they also transfer line strength to the main lines.

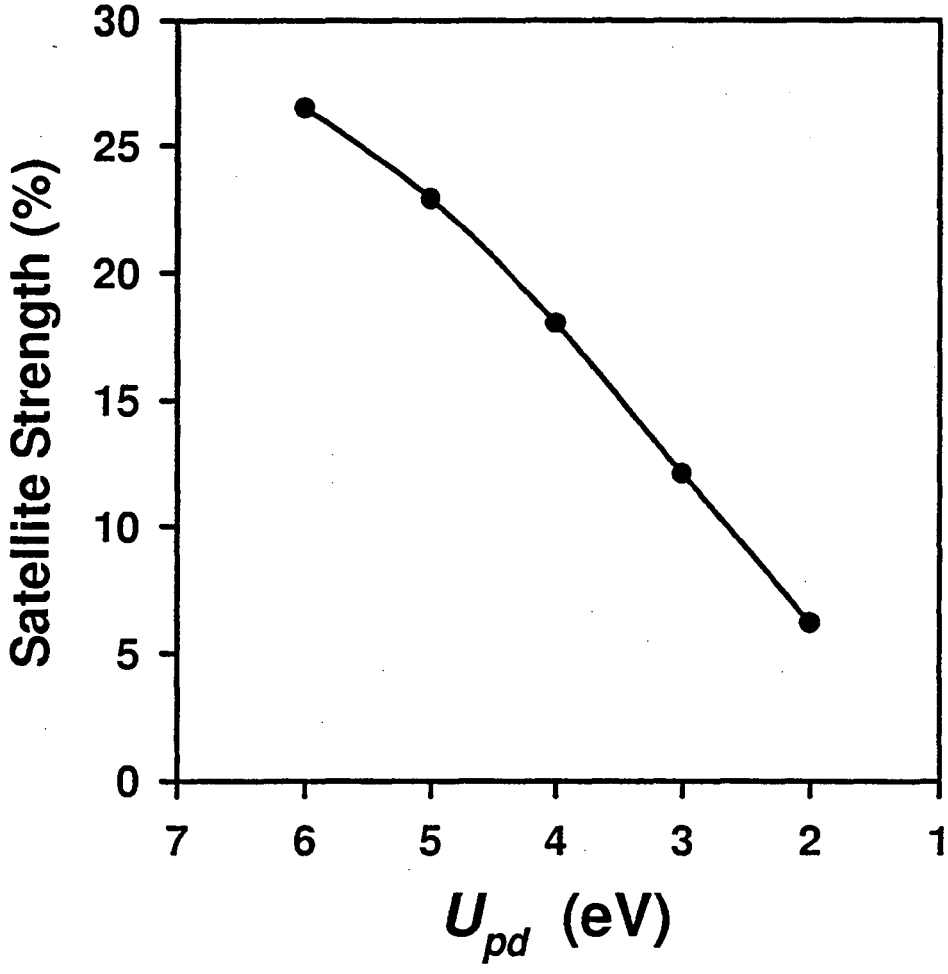

Figure 3.14: Satellite strength as percent of total intensity. As the direct Coulomb repulsion U_{pd} varies from 6 to 2 eV, the satellite strength is dramatically reduced.

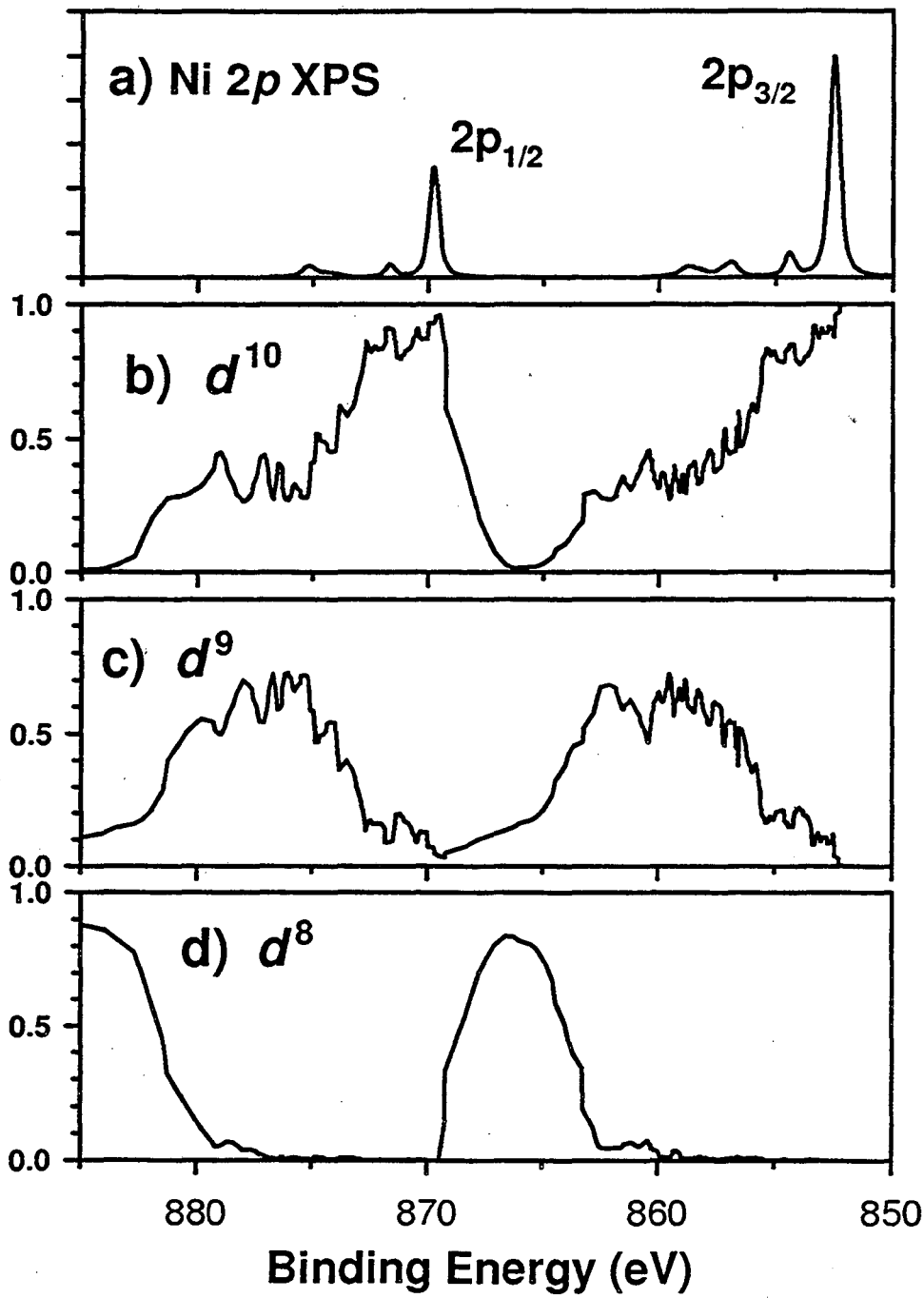

Figure 3.15: Local atomic configuration. (a) Ni $2p$ photoemission spectrum, with narrow broadening. (b)-(d) Fractional d^{10}, d^9, and d^8 character of the final states, respectively. The main lines are about 90% d^{10} and 10% d^9. The satellites are about 60-70% d^9 and 30-40% d^{10} character. The d^8 states occur approximately 10-15 eV to the left of the main lines and are not excited.

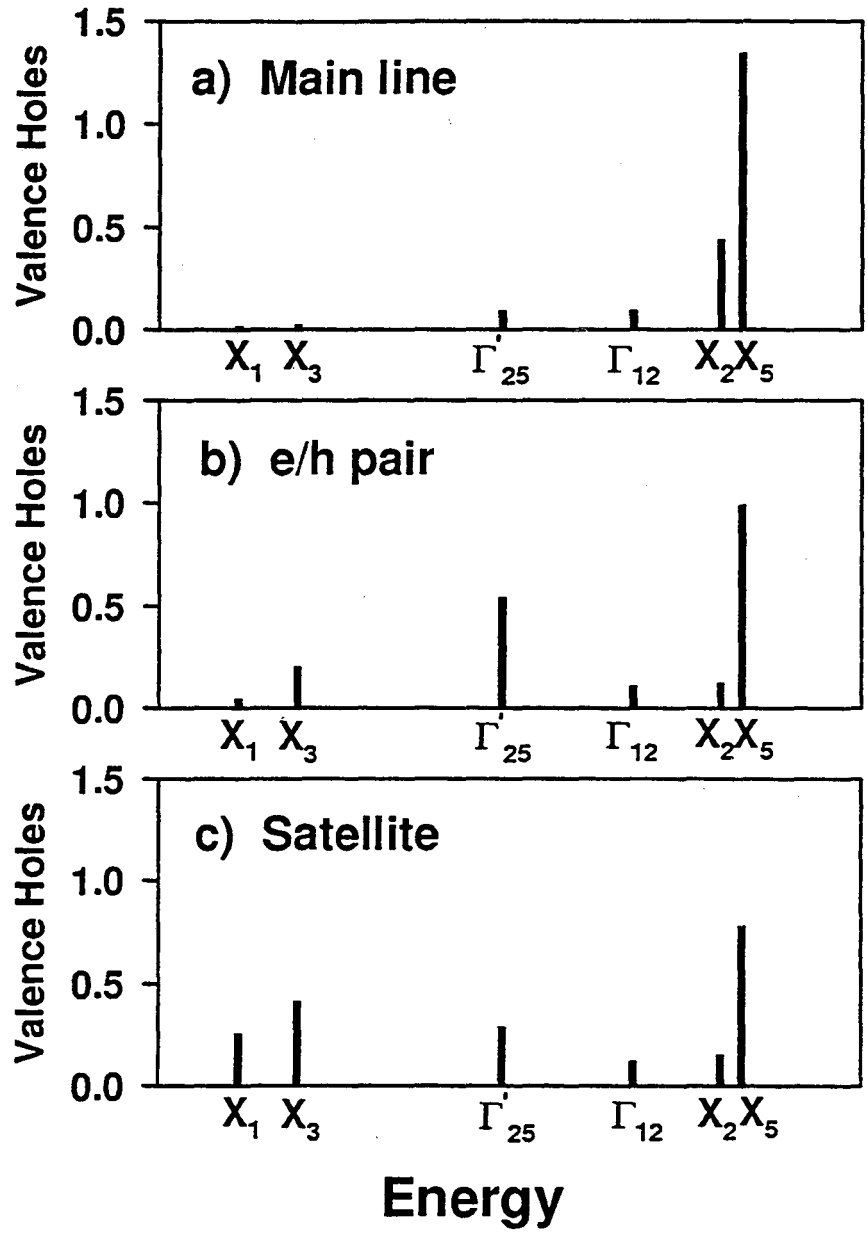

Figure 3.16: Bloch state valence configurations. (a) Main-line decomposition. Both holes are at or near the Fermi level. (b) For e/h pairs , there is a substantial probability of exciting a shakeup electron from below the Fermi level. (c) For satellite final states, we find significant probability of finding holes at any of the Bloch states.

Chapter 4

Many-Body Theory of Ni $3p$ Photoemission

4.1 Introduction

In a typical core-level photoemission experiment, monochromatic light of wavevector $\mathbf{q}$, polarization ϵ, and energy $\hbar\omega$ impinges on a sample, exciting the core electrons into free electron states far above the Fermi sea. The wavevector $\mathbf{k}$, kinetic energy E_k, and perhaps also the spin σ of these photoelectrons are then measured. Knowing E_k and $\hbar\omega$ allows one to deduce the electron binding energy E_B via the simple relation: $E_B = \hbar\omega - E_k$. The core-level binding energies of the elements are well known, and so a peak in a photoemission spectrum at a given binding energy serves as a sort of "atomic fingerprint" for the presence of a given species of atom. This makes core-level photoelectron spectroscopy a powerful element specific probe of condensed matter systems.

More specifically, several core-level photoemission investigations have been carried out for the itinerant ferromagnets Fe, Co, and Ni. The core electrons in these systems are coupled to the spin-polarized valence electrons through the Coulomb and exchange interactions. In a ferromagnet, therefore, core electrons with spin parallel to the majority in the valence band should see their average position shifted to higher binding energy. In spin-resolved x-ray photoelectron spectroscopy (SRXPS), the spin of the outgoing photoelectron is measured, and these spin-polarized spectra serve as a direct probe of the local electronic and magnetic environment. Such SRXPS studies have been performed on Fe [25], Co [26], and Ni [27] using unpolarized radiation sources.

Alternative probes – without requiring electron spin detection – are possible with high-intensity polarized synchrotron radiation. The dipole operator, which acts only on the orbital component of the core wavefunction, can couple indirectly to the core spin via the spin-orbit interaction. The core spin, in turn, couples to the spin-polarized valence electrons through exchange. Therefore, the photon couples indirectly to the valence band, and so the spin-integrated spectra in an angle-resolved photoemission experiment can depend on the magnetic orientation. Measuring these intensity differences upon reversal of the sample magnetization is known as magnetic dichroism in the angular distribution. Such dichroism using circularly polarized light (MCDAD) was first observed by Baumgarten *et al.* [21] in Fe $2p$, and using linearly polarized light (MLDAD) by Roth *et al.* in Fe $3p$.

For the relatively delocalized transition metals Fe and Co, one-electron theories [40, 41] reproduce experimental results relatively well for $2p$ and $3p$ core levels. These methods all involve calculating – in one way or another – the intensities of the six $|j, m_j\rangle$ core states, and then positioning the lines at the appropriate energy. This approach implicitly assumes that the $|j, m_j\rangle$ are good quasiparticle states. This assumption clearly breaks down in a localized atomic-like system, where coupling between the core hole and the valence shell results in a complex multiplet structure. For such systems, the spectra cannot be described with only six lines.

The situation for Ni is complicated by the fact that it not only exhibits a multiplet structure, but also displays extra-atomic screening effects. Therefore, both the *localized* and the *delocalized* properties of the valence electrons are manifest in the photoemission spectrum. It is this "intermediate coupling" nature of Ni that makes it a particularly instructive and interesting system to study.

Up to now, most theoretical efforts to describe core-level photoemission from Ni have been based on an Anderson impurity model [37, 75, 76]. In this model, Ni is treated

as an "impurity" within a Ni host, and extra-atomic screening is described in terms of hybridization of valence orbitals with adjacent atoms through an adjustable "mixing parameter".

An alternative approach is the periodic small-cluster model used by Victora and Falicov [53] to describe the Ni valence band photoemission spectrum, and by Menchero [38, 39] to analyze the Ni $2p$ core level. It is this model which we extend here to consider the case of photoemission from the Ni $3p$ core level. Unlike the Anderson model, this model contains translational symmetry operations due to periodicity. Translational symmetry implies a band structure, which in turn describes the hopping of the valence electrons. Therefore, extra-atomic screening is treated naturally by way of the electronic band structure.

The chapter is organized as follows: In Sec. 4.2 we provide a brief description of the model. We then present the calculated Ni $3p$ spin-resolved spectra and make a detailed comparison to experimental results. In Sec. 4.3 we present and discuss spin-resolved and circular-polarized spectra for a variety of limiting cases. This analysis provides important insights into the underlying physics. We also present results from a simple model that correctly explains the transfer of spectral weight between the satellites and the main lines. We then discuss hybridization effects between d^8, d^9, and d^{10} configurations, and plot the local atomic configuration as a function of binding energy. Conclusions are given in Sec. 4.4.

4.2 Results

Our model has been described elsewhere [39]. Briefly, it consists of a tetrahedral cluster of four Ni atoms, with periodic boundary conditions imposed to generate the full *fcc* lattice. Each atom in the lattice can be labeled by an index 1-4, and is surrounded by twelve nearest neighbors of a different index. Such periodicity dictates that all Bloch

states must transform according to either Γ or X in the Brillouin zone.

We use d-orbitals to describe the valence band and p-orbitals for the core electrons. Our Hamiltonian contains three types of terms: core-level spin-orbit coupling, intrasite electron-electron Coulomb repulsion, and valence band hopping. We use 1.74 eV for the spin-orbit splitting between the $j = 3/2$ and $j = 1/2$ core levels, a value used by previous workers [76].

The Coulomb interaction is described in terms of the standard Slater integrals, which are given in Table 4.1. For the F and G integrals, we again adopt the values of previous workers [76]. The U_{dd} and U_{pd} must be treated as adjustable parameters. For U_{dd} we use 3 eV, although the calculated spectra are found to be virtually independent of this parameter for any reasonable choice. This is a reflection of the fact that d^9 and d^{10} configurations dominate both the initial states and the final states. U_{pd} determines the overall energy of the p^5d^9 final states, and hence the satellite position. We obtain good agreement with experiment using $U_{pd} = 5$ eV.

The valence band hopping is described in terms of the electronic band structure. For a four-site cluster, one particle in the valence band can occupy one of 20 d-orbitals. These 20 states can be constructed using the complete projection operators [62], and decompose with the following symmetries:

$$\Gamma_{12} \oplus \Gamma'_{25} \oplus \mathrm{X}_1 \oplus \mathrm{X}_2 \oplus \mathrm{X}_3 \oplus \mathrm{X}_5 \ . \tag{4.1}$$

The energies of these Bloch states are matched to the spin-averaged band structure calculations of Wang and Callaway [56], which are given in Table 4.1.

The ground state in our model is ferromagnetic with a 50% d^9 and 50% d^{10} initial-state configuration, leading to a spin moment of 0.50 μ_B per atom. In this work, we use the sign convention that the magnetization direction is "up", meaning that the majority electrons are spin *down*. Spectra are calculated using Fermi's golden rule

within the electric dipole and sudden approximations. We include interference between the $l \pm 1$ channels, and use the channel matrix elements and phase shifts of Goldberg, Fadley, and Kono [47]. Photoelectron diffraction effects are not considered in this work, although in some cases such effects are known to cause significant changes in both the spin polarization [77] and magnetic dichroism [34, 78].

In Fig. 4.1 (a) we present experimental Ni $3p$ spin-resolved spectra due to See and Klebanoff [27]. A single-crystal Ni sample, remanently magnetized in the surface plane, was irradiated with a Mg $K\alpha$ x-ray source. Photoelectrons were collected normal to the surface and their spin measured along the magnetization direction. Instrumental resolution was 1.6 eV FWHM. Solid (dashed) lines are for photoelectrons with spin parallel to the minority (majority) electrons in the valence band. The experimental results are characterized by three main features: a broad main line (labeled A), and two satellite structures (labeled B and C) centered about ~ 72 eV and ~ 77 eV. The main line displays a strong minority spin polarization, as does satellite B. Satellite C, on the other hand, exhibits a strong majority spin polarization.

In Fig. 4.1 (b) we present the corresponding theoretical spin-resolved spectra, which were calculated for normal emission and a grazing-angle geometry, i.e., photon $\mathbf{q}$ was taken parallel to magnetization $\mathbf{M}$, with photoelectron $\mathbf{k}$ normal to $\mathbf{M}$. The geometry adopted for the calculation was chosen to eliminate spin-orbit induced spin polarization. The experimental geometry, which was chiral, has been described in Chapter 3. Experimentally, the elimination of spin-orbit induced spin polarization was accomplished by averaging over both magnetic orientations. We use channel matrix elements taken at Mg $K\alpha$ photon energy [47]. Lines were convoluted with a Gaussian (1.6 eV FWHM) to simulate instrumental broadening, and by Lorentzians (1.5 eV FWHM for A and B, 2.5 eV for C) to simulate lifetime broadening. For narrower broadenings, the well known 2-eV shoulder emerges in the main line. For the relatively wide broadenings used here,

however, this shoulder is hardly discernible.

The theoretical results correctly reproduce all the principal features of the experimental spectra, and the relative positions and intensities of peaks A, B, and C agree very well with observations.

In Fig. 4.1 (c) we plot the theoretical and experimental spin polarizations. In both theory and experiment, feature C has a strong majority spin polarization, whereas features A and B exhibit minority spin polarizations. While the theoretical results correctly predict the *sign* of the spin polarization throughout the spectrum, the *magnitude* is overestimated at C and underestimated at A and B. This is probably due to a net minority background spin polarization in this energy range. Since the core is fully occupied in the initial state, the spin polarization integrated over the energy range of the core shell should vanish:

$$\int_{core} (I_{up.} - I_{down}) dE = 0. \tag{4.2}$$

Clearly, the experimental observations do not satisfy this result. Agreement between theory and experiment would be improved if the minority spectrum of the latter were rigidly shifted downward to correct for the background spin polarization.

4.3 Discussion

The Ni $3p$ spectrum exhibits several complex subtleties due to the interplay between Coulomb and exchange interaction, spin-orbit coupling, and extra-atomic screening. In order to gain physical insight into the underlying structure, we consider here a variety of limiting cases. From Fig. 4.1, we see that the satellites are spread over a manifold of more than 12 eV. Spin-orbit splitting, on the other hand, is only 1.74 eV. This suggests that LS coupling is a reasonably good starting point for describing the satellite structures. We then discuss the transfer of spectral weight between satellites and main lines, and

show that the effect can be understood in terms of a simple 2x2 model. Finally, we turn to the question of final-state configurations. This allows us to describe in a more quantitative way the physical nature of the final states.

4.3.1 Spin polarization

In this section we present theoretical spin-resolved spectra for a variety of limiting cases, with the same grazing-angle geometry described in Sec. II. Lines were convoluted with Gaussian (FWHM=1 eV) and Lorentzian (FWHM=1 eV) lineshapes and the channel matrix elements were taken at 400-eV photon energy [47]. The photon energy was chosen to permit a more direct comparison with experimental MCDAD data presented later, which were also taken at 400-eV.

As our first case, we consider the spin-resolved spectra in the limit of LS coupling and zero valence bandwidth. We obtain the zero-bandwidth limit by setting the energies of all the Bloch states in Table 4.1 to zero. For this case, there can be no mixing or hybridization in the final states; i.e., the number of valence electrons on the core-hole atom is a good quantum number. In this way, each line in the spectrum can be assigned a precise physical interpretation. We obtain the LS limit by setting the spin-orbit coupling to zero. In this case, the total L and total S of the core-hole atom are good quantum numbers.

The spin-resolved spectra are presented in Fig. 4.2(a). As before, majority electrons are spin down. Even in this limit, already the gross features of the actual Ni $3p$ spectra are apparent: i.e., a main line A and two satellites B and C, each with the correct spin polarization. The most obvious discrepancies between these spectra and the actual SRXPS spectra are that the satellite intensities are too large and that there is no 2-eV shoulder in the main line.

For this simple limit, it is instructive to examine in greater detail the underlying

structure of the spectra. If the core hole is created at a site which is locally d^9, then the core hole and the valence hole angular momenta couple according to the LS scheme. The resulting term energies can be calculated analytically:

$$
\begin{aligned}
E(^3F) &= U_{pd} - \frac{6}{15}G^1_{pd} + \frac{2}{35}F^2_{pd} - \frac{3}{245}G^3_{pd} \\
E(^1D) &= U_{pd} - \frac{3}{15}G^1_{pd} - \frac{7}{35}F^2_{pd} + \frac{21}{245}G^3_{pd} \\
E(^3P) &= U_{pd} - \frac{1}{15}G^1_{pd} + \frac{7}{35}F^2_{pd} - \frac{63}{245}G^3_{pd} \\
E(^3D) &= U_{pd} + \frac{3}{15}G^1_{pd} - \frac{7}{35}F^2_{pd} - \frac{21}{245}G^3_{pd} \\
E(^1P) &= U_{pd} + \frac{1}{15}G^1_{pd} + \frac{7}{35}F^2_{pd} + \frac{63}{245}G^3_{pd} \\
E(^1F) &= U_{pd} + \frac{6}{15}G^1_{pd} + \frac{2}{35}F^2_{pd} + \frac{3}{245}G^3_{pd} \, .
\end{aligned}
\tag{4.3}
$$

The resulting spectrum in this limit contains exactly seven lines: a single d^{10} line and six lines for the d^9 configuration. These spin-resolved line strengths are given in Table 4.2, and yield the following observations:

(a) The d^{10} line, being intrinsically nonmagnetic, is unpolarized.

(b) The net intensities of the d^9 and d^{10} lines are in exact proportion to their ground state populations; i.e., 50% of the line strength is d^9 and 50% d^{10}.

(c) The d^9 triplet lines are minority spin polarized in the ratio 2:1; the singlet lines are 100% majority spin polarized.

(d) The spin-integrated strengths of the d^9 lines are proportional to the number of states in the terms: e.g., $I(^3P)/I(^1P)$ =3:1, $I(^3D)/I(^3P)$ =5:3, etc.

Therefore, in this limit, the leading edge of the main line is d^{10}, but the spin polarization is due to the ^3F term. Feature B is due to the ^3P and ^3D terms, leading to a strong minority spin polarization. Feature C is due to ^1P and ^1F terms and is therefore 100% majority spin.

As our next case, we introduce a realistic spin-orbit splitting of 1.74 eV between $p_{3/2}$ and $p_{1/2}$, but maintain the valence bandwidth at zero. With nonzero spin-orbit coupling, total L and total S of the core-hole atom are no longer strictly good quantum numbers. Total angular momentum J of the core-hole atom is still rigorously a good quantum number, and the triplet terms in Eq. 4.3 break up into individual lines of definite J. Therefore, in this limit, the spectrum consists of 14 lines: the spin-orbit split d^{10} lines and the 12 d^9 lines.

The spin-resolved spectra for this case are presented in Fig. 4.2(b). Satellite C is almost unchanged from the strict LS limit case. However, satellite B is noticeably broader due to the splitting of the ^3P and ^3D terms. The most obvious change with the introduction of spin-orbit coupling is the appearance of a "twin peak" structure in the main line.

Again, since the number of lines is so limited, and because each line can be unambiguously assigned, it is instructive to explicitly examine the intensities of each line, which are given in Table 4.3. We observe the following:

(a) The d^{10} lines are unpolarized. The d^{10} lines are intrinsically nonmagnetic and so can exhibit no exchange-induced spin polarization. Although there can be spin-orbit-induced spin polarization in a d^{10} line [57], in the nonchiral geometry considered here such effects are not present. Therefore, the spin polarization is determined exclusively by the d^9 configuration.

(b) The relative intensities of the $p_{3/2}d^{10}$ to $p_{1/2}d^{10}$ lines is 2:1, a reflection of the $2j+1$ multiplicity of the levels.

(c) The relative spin-integrated intensities of the d^9 lines are proportional to the multiplicity $2J+1$.

(d) The spin polarization of the $^1D_2$ line is effectively neutralized through strong mixing with the $^3F_2$ line. This example clearly demonstrates the strong hybridization

effects that occur when two energetically nearby lines are allowed to mix. Before spin-orbit coupling is turned on, the ^1D line is 100% spin down, and energetically separated by only 0.57 eV from the ^3F line, which is primarily spin up. With spin-orbit coupling, the lines repel and $^1D_2$ acquires much of the spin-up character of $^3F_2$, and vice versa.

(e) The main-line leading edge is $p_{3/2}d^{10}$ and the high binding energy "twin peak" is due to ^3F and $p_{1/2}d^{10}$.

Next we consider the effect of extra-atomic screening by introducing a narrow valence bandwidth. This is accomplished by multiplying the energies of the Bloch states in Table 4.1 by a scaling factor of 0.50. The resulting spectra are presented in Fig. 4.2(c). With a small but nonzero bandwidth, configurations can mix, meaning that the electron occupancy of the core-hole atom is no longer a good quantum number. Also, line strength is now transferred from the high binding energy side of the spectrum to the low binding energy side, i.e., satellites B and C lose intensity to the main line. This is also true *within* the main line: the high binding energy "twin" in the main line transfers intensity to the low binding energy side, and thereby reduces itself to a shoulder.

Although satellite peaks B and C are no longer pure d^9 due to hybridization, the peaks are still clearly identified. In this sense it is still meaningful to assign satellite C to ^1P and ^1F terms, and satellite B to ^3P and ^3D terms.

Caution must be exercised in assigning the main line. Before the valence bandwidth is turned on, the $^3F_2$, $^3F_3$, and $p_{1/2}$ lines are energetically separated by only 120 meV (see Table 4.3). Any mixing between these lines will lead to very strong hybridization, as demonstrated by our previous example. Therefore, although the Ni $3p$ main line cannot be unambiguously defined, we can say that it consists of a heavily hybridized mixture of $p_{1/2}d^{10}$, ^3F, and $p_{3/2}d^{10}$ lines.

As our final case, we set the valence bandwidth to 100% of its actual value, and present the resulting spectra in Fig. 4.2(d). As the bandwidth is increased , extra-

atomic screening transfers additional spectral weight from the d^9 satellites to the main line. While satellites B and C both lose intensity, careful examination of Figs. 4.2(b)-(d) show that as the bandwidth is increased from 0% to 100%, satellite B loses a *greater* proportion of its intensity. This transfer of spectral weight, which depends sensitively on relative binding energy, is discussed in greater detail below.

We further observe that as the bandwidth is increased, the positions of satellites B and C are shifted to higher binding energy. This is because a local d^9 excitation, when viewed in k-space, must contain sizable components of Bloch states from below the Fermi level. As the bandwidth is increased, the energetic cost of promoting these electrons is also increased, and the line shifts to higher binding energy.

Finally, we observe that line strength continues to be transferred within the main line from the high binding energy side to the low side. In doing so, the 2-eV shoulder becomes less pronounced.

4.3.2 Magnetic circular dichroism

In Fig. 4.3(a) we present theoretical spin-integrated spectra at 400-eV photon energy for RCP and LCP excitation. Spectra were calculated for the same grazing-angle geometry as described above, and normalized to a peak intensity of 100. Lines were convoluted with a Gaussian of 1.6 eV FWHM and Lorentzians of 1.5 eV FWHM (for A and B) and 2.5 eV FWHM (for C). The corresponding MCDAD, defined as $I_{RCP} - I_{LCP}$, is presented in Fig. 4.3(b). Satellite C is characterized by a plus feature, whereas the high binding energy side of satellite B displays a strong minus feature. The main line A is characterized by a very pronounced minus/plus feature, centered about the intensity maximum. In addition to these four strong dichroism peaks, there is also a very weak positive feature centered about $\sim$ 70 eV.

For comparison, we present Ni $3p$ experimental and theoretical MCDAD results,

both due to van der Laan *et al.* [75]. The experimental data, presented in Fig. 4.4, were taken at 400-eV photon energy from a single-crystal sample. In their data, the dichroism was multiplied by a factor of 2 to account for the incomplete circular polarization of the light and incomplete magnetization of the sample. The theoretical results, presented in Fig. 4.5, were calculated using an Anderson impurity model. The *shape* of our calculated MCDAD agrees well with both the experimental (Fig. 4.4) and theoretical (Fig. 4.5) results of van der Laan. Two comments are in order regarding the *magnitude* of the dichroism:

1) The magnitude of the calculated dichroism found here ($\sim 2\%$) is roughly the same as that calculated by van der Laan *et al.*, even though the present work uses considerably narrower line broadenings. This can be attributed to differences in the ground states: the ground state used by van der Laan *et al.* contains a nonzero orbital moment as well as a sizable fraction of d^8 configuration.

2) The magnitude of the MCDAD calculated here is smaller than the observed dichroism (Fig. 4.4). This may be due in part to photoelectron diffraction effects arising from the single-crystal sample used in the experiment by van der Laan *et al.*[75].

These questions will be addressed in greater detail in Chapter 5. For present purposes, however, we are not so concerned about the magnitude of the dichroism. Instead, we concentrate here on trying to understand the underlying structure of the lineshape.

To gain physical insight into the MCDAD spectrum, we consider the same limiting cases as before. Spin-integrated spectra for RCP and LCP excitation are presented in Fig. 4.6. All lines were broadened by Gaussian and Lorentzian lineshapes of 1.0 eV FWHM each.

As our first case, we consider the limit of zero spin-orbit coupling and zero valence bandwidth. In the absence of spin-orbit coupling, there is no way for the dipole operator – which acts only on the orbital part of the wavefunction – to couple to the spin-polarized

valence band. For this case, we see from Fig. 4.6(a) that $I_{RCP} = I_{LCP}$, and hence the dichroism vanishes. We can also see from Table 4.2 that this result holds on a line by line basis.

As our next limiting case, we set the core-level spin-orbit splitting to 1.74 eV, but maintain the valence bandwidth at zero. With nonzero spin-orbit coupling, we see from Fig. 4.6(b) that a dichroism is now observed: satellite C acquires a plus feature, satellite B a minus/plus feature, and the main line also acquires a minus/plus feature. Already in this simple limiting case, therefore, we have correctly reproduced the sign of the dichroism throughout the spectrum. However, we see that the low binding energy side of satellite B exhibits a relatively large dichroism, whereas in the final calculated result (Fig. 4.3(b)), it possesses only a very weak MCDAD signal. We show below that the disappearance of this feature is due to the combined effect of line broadening and extra-atomic screening.

Again, it is useful to explicitly examine the intensities of the individual lines, which are given in Table 4.3. We see that the d^{10} lines exhibit no dichroism. However, as the d^9 lines split apart into lines of definite J, each acquires a dichroic character. In this way, the minus/plus feature at the main line A is due to lines derived from the ^3F term. In satellite B, ^3P leads to a plus feature, whereas the minus feature is due to ^3D. In satellite C, ^1P and ^1F both give rise to a positive dichroism. We also note from Table 4.3 that $I_{up} + I_{down} = I_{RCP} + I_{LCP}$ on a line by line basis; either way, the sum of the two gives the spin-integrated spectrum for unpolarized excitation.

In Fig. 4.6(c) we see the effect of introducing a valence bandwidth of 50% its actual value. While extra-atomic screening significantly affects the circular-polarized spectra, the *difference* spectrum is still characterized by the same plus/minus features as before. However, due to spectral weight transfer, the low binding energy side of satellite B loses more intensity than the high binding energy side, and so the resulting dichroism in this

region is reduced accordingly.

This can be seen even more clearly for the case of 100% valence bandwidth, which is plotted in Fig. 4.6(d). The high binding energy side of satellite B preserves its negative dichroism, but the positive MCDAD on the low binding energy side is almost entirely washed out by extra-atomic screening. When the wider broadenings of Fig. 4.3 are employed, the weak positive dichroism of this feature is further washed out by the much larger negative dichroisms on either side. Therefore, we see that the MCDAD can be understood by first examining the limit of zero valence bandwidth, and then considering the effects of line broadening and extra-atomic screening.

4.3.3 Transfer of spectral weight

In this section we investigate in greater detail how extra-atomic screening transfers spectral weight between a d^9 satellite and a d^{10} main line. In particular, we wish to determine how this transfer depends on the valence bandwidth and satellite position.

From Fig. 4.2 we see that each satellite maintains its relative spin polarization as intensity is transferred to the main line, although satellites B and C do not lose strength in the same proportion. In other words, to first order, the transfer of spectral weight does not depend on spin, but rather on relative binding energy. This suggests that we can neglect electron spin when modeling the effect.

We choose as our simple model a two-atom system with periodic boundary conditions and one valence orbital per site. In our initial state we have one hole in the valence band, so that the local occupancy fluctuates between zero and one holes. This is in direct analogy to the case of Ni, where the dominant d^{10} and d^9 configurations also lead to local fluctuations of zero or one holes. For spinless electrons, the basis states are given by:

$$|f_1\rangle = c^{\dagger}_{v_1}|0\rangle \tag{4.4}$$

$$|f_2\rangle = c^{\dagger}_{v_2}|0\rangle$$

where $c^{\dagger}_{v_i}$ creates a valence hole at site i. If t is the hopping parameter for holes, then the Hamiltonian matrix is given by:

$$H = \begin{bmatrix} 0 & t \\ t & 0 \end{bmatrix}. \tag{4.5}$$

The ground state has energy $-t$ and is given by:

$$|GS\rangle = \frac{|f_1\rangle - |f_2\rangle}{\sqrt{2}} \tag{4.6}$$

The anti-bonding state is at energy $+t$ and hence the valence bandwidth is $BW = 2t$. Upon photoemission, a core hole is created, and our new basis states become:

$$\begin{aligned} |g_1\rangle &= c^{\dagger}_{c_1}|f_1\rangle \\ |g_2\rangle &= c^{\dagger}_{c_1}|f_2\rangle \end{aligned} \tag{4.7}$$

where $c^{\dagger}_{c_1}$ creates a core hole at site 1. The Hamiltonian H' after photoemission is given by:

$$H' = \begin{bmatrix} U & t \\ t & 0 \end{bmatrix}, \tag{4.8}$$

where U is the Hubbard term which describes the intrasite Coulomb repulsion between the core hole and the valence hole. The unnormalized eigenstates of H' are given by:

$$\begin{aligned} |e^+\rangle &= \left(U + \sqrt{U^2 + 4t^2}\right)|g_1\rangle + 2t|g_2\rangle \\ |e^-\rangle &= 2t|g_1\rangle - \left(U + \sqrt{U^2 + 4t^2}\right)|g_2\rangle, \end{aligned} \tag{4.9}$$

In the limit $t \to 0$, we see $|e^+\rangle \sim |g_1\rangle$ and $|e^-\rangle \sim |g_2\rangle$. In other words, $|e^+\rangle$ corresponds to the satellite and $|e^-\rangle$ to the main line. We obtain the satellite intensity in the sudden approximation by projection:

$$I_{sat} = \frac{|\langle e^+|c^{\dagger}_{c_1}|GS\rangle|^2}{\langle e^+|e^+\rangle}. \tag{4.10}$$

If we define the dimensionless parameter $\tau = BW/U$, then the result is given by:

$$I_{sat} = I_0 \left[\frac{1 - \tau + \tau^2 + (1-\tau)\sqrt{1+\tau^2}}{1 + \tau^2 + \sqrt{1+\tau^2}} \right], \tag{4.11}$$

where I_0 is the satellite intensity in the limit of zero valence bandwidth (in this example, $I_0 = 0.5$). In the narrow bandwidth limit, Eq. 4.11 reduces to $I_{sat} = I_0(1-\tau)$; i.e., the satellite intensity is predicted to decrease linearly with increasing valence bandwidth.

To study how well Eq. 4.11 describes the screening process in Ni, we must first determine $\tau = BW/U$ for the satellites. From Table 4.1, the Ni valence bandwidth is 4.31 eV. For U, we must use the *effective* Hubbard interaction U_{eff}, defined here as the energy separation in the limit of zero valence bandwidth between the satellite and the leading edge of the main line. From Table 4.3, this is roughly 5.4 eV for satellite B and roughly 10.4 eV for satellite C. Hence, we use $\tau_B = 0.80$ and $\tau_C = 0.41$. In Fig. 4.7 we plot the intensities of satellites B and C as a function of valence bandwidth. These intensities were calculated two different ways: first by means of numerical integration using the full many-body calculation and second by using Eq. 4.11 with the τ_B and τ_C given above. The two approaches yield results that are in excellent agreement, indicating that the important quantity governing the transfer of spectral weight is the ratio of the valence bandwidth to the effective Hubbard repulsion.

4.3.4 Final state configuration

In this section we examine in greater detail hybridization effects and the nature of the final state. Upon photoexcitation, a localized core hole is created at a particular site, leading to a sudden attractive potential for nearby electrons. If the core hole is created at a site that is locally d^9, then an electron from a neighboring atom can hop into the unoccupied valence orbital, thereby screening the core hole. This extra-atomic screening leads to mixing of the configurations.

For a given final eigenstate $|\Psi_f\rangle$, of energy E_f, we wish to know the local number of valence electrons on the core-hole atom. Let $|d_k^n\rangle$ be the kth basis state with exactly n valence electrons on the photoexcited atom. We then calculate the local atomic configuration according to:

$$F^n(E_f) = \sum_k \left|\langle d_k^n|\Psi_f\rangle\right|^2 , \tag{4.12}$$

where $F^n(E_f)$ gives the fractional probability of finding the final eigenstate of energy E_f with n valence electrons on the core-hole atom. We then average over a sufficiently small energy interval to obtain a smooth function defined for the range of core-level binding energies. Since the valence configuration fluctuates between 8,9, and 10 electrons,

$$F^8 + F^9 + F^{10} = 1.0 \tag{4.13}$$

must hold for every eigenstate $|\Psi_f\rangle$.

In principle, such a description could be misleading. Consider the zero bandwidth limit. In this case, each line in the spectrum can be unambiguously assigned to either d^9 or d^{10} configurations, e.g., the satellites are pure d^9 final states. However, there may be d^{10} states of zero intensity in the energetic neighborhood of the d^9 satellite. In such a case, we would not wish to include these d^{10} lines in our average, as this would imply that the satellite were not pure d^9. One way around this would be to eliminate all lines below some cutoff intensity, say 2% of the intensity of the strongest line in the spectrum. In practice, such a distinction introduces only relatively small differences in the theoretical final-state configuration. The reason is that all neighboring lines are sufficiently well hybridized so that the calculation using either method yields similar results.

In Fig. 4.8 we present the local d^8, d^9, and d^{10} configurations calculated according to Eq. 4.12, with the Ni $3p$ spin-integrated spectrum plotted on the same energy scale for convenient reference.

We see that the leading edge of the main line is 80-90% d^{10}, and the trailing edge is roughly 70-80% d^{10}. Therefore, the nominally $d^9\ {}^3F$ lines get largely mixed into the nearby d^{10} states, leading to a strongly hybridized mixture of the two. Even so, as we have seen, analysis of the purely $d^9\ {}^3F$ term for the zero-bandwidth limit correctly predicted both the minority spin polarization and the minus/plus dichroism feature of the main line.

We also see from Fig. 4.8 that satellite B is roughly half d^9 and half d^{10}, while satellite C is roughly 60% d^9, 35% d^{10}, with a little d^8 mixed in. If we eliminate all lines below a 2% cutoff intensity, we find that the d^9 character of satellite B is increased by 10-15%, and the d^9 character of satellite C is increased by 15-20%.

Finally, we observe that most of the d^8 states occur 20-25 eV to the left of the main line. These states are not excited in our model due to the absence of d^8 in our ground state.

4.4 Conclusions

We have presented theoretical Ni $3p$ photoemission spectra calculated within a periodic small-cluster model. Theoretical results were found to compare very well with experimental observations. We examined theoretical spectra for a variety of limiting cases, thereby gaining considerable physical insight into the underlying structure. We showed that, upon introduction of a valence bandwidth, there is a strong transfer of spectral weight to the main line. We showed further that this spectral weight transfer depends on the ratio of the valence bandwidth to the effective Hubbard interaction U_{eff}. Finally, we discussed hybridization effects and configuration mixing in the final state, and calculated the local atomic configuration as a function of binding energy.

Table 4.1: Slater integrals and spin-averaged band energies used in this work.

Integral	Energy (eV)	Bloch State	Energy (eV)
U_{dd}	3.00	Γ_{12}	0.92
F^2_{dd}	8.65	Γ'_{25}	2.04
F^4_{dd}	5.40	X_1	4.31
U_{pd}	5.00	X_2	0.18
G^1_{pd}	10.99	X_3	3.81
F^2_{pd}	8.84	X_5	0.00
G^3_{pd}	6.70		

Table 4.2: Final states and relative binding energies in the limit of zero spin-orbit interaction and zero valence bandwidth. I_{up} and I_{down} are the spin-resolved photoemission intensities for unpolarized excitation. I_{RCP} and I_{LCP} are the spin-integrated intensities for right and left circular-polarized excitation.

State	Energy (eV)	I_{up}	I_{down}	I_{RCP}	I_{LCP}
d^{10}	0.00	50.00	50.00	50.00	50.00
^3F	1.03	23.33	11.67	17.50	17.50
^1D	1.60	0.00	8.33	4.17	4.17
^3P	4.32	10.00	5.00	7.50	7.50
^3D	4.85	16.67	8.33	12.50	12.50
^1P	9.22	0.00	5.00	2.50	2.50
^1F	9.98	0.00	11.67	5.83	5.83
Total		100.0	100.0	100.0	100.0

Table 4.3: Final states and relative binding energies for a spin-orbit splitting of 1.74 eV, in the limit of zero valence bandwidth. I_{up} and I_{down} are the spin-resolved photoemission intensities for unpolarized excitation. I_{RCP} and I_{LCP} are the spin-integrated intensities for right and left circular-polarized excitation.

State	Energy (eV)	I_{up}	I_{down}	I_{RCP}	I_{LCP}
$p_{3/2}d^{10}$	-0.58	33.33	33.33	33.33	33.33
$^3F_4$	0.45	10.48	4.52	9.30	5.70
$^3F_2$	1.04	2.20	6.14	2.58	5.75
$^3F_3$	1.10	6.99	4.68	5.57	6.10
$p_{1/2}d^{10}$	1.16	16.67	16.67	16.67	16.67
$^1D_2$	2.19	3.94	4.40	4.32	4.01
$^3P_0$	3.74	0.83	0.83	1.03	0.63
$^3P_1$	3.83	4.12	0.88	3.06	1.94
$^3P_2$	4.17	5.06	3.27	4.90	3.44
$^3D_3$	4.68	7.09	4.58	5.64	6.02
$^3D_1$	5.17	2.45	2.55	1.64	3.36
$^3D_2$	5.57	6.65	1.68	2.87	5.47
$^1P_3$	9.39	0.10	4.90	2.80	2.20
$^1F_3$	10.08	0.09	11.57	6.29	5.38
Total		100.0	100.0	100.0	100.0

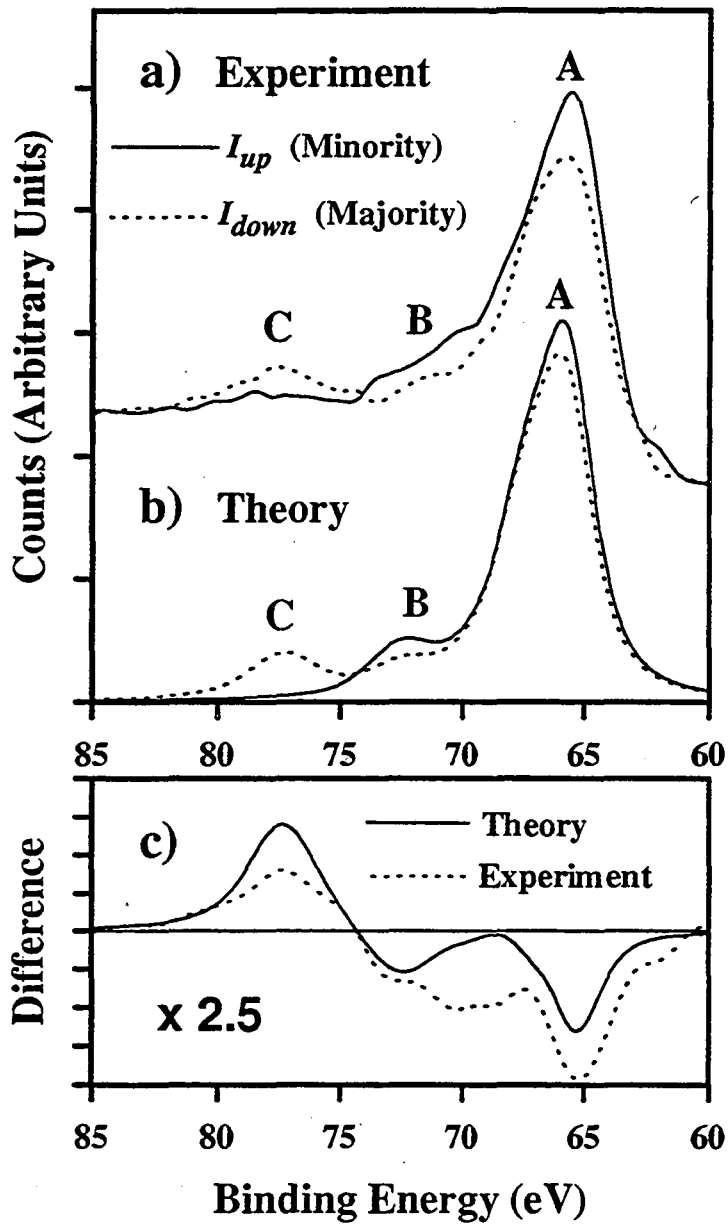

Figure 4.1: Experimental and theoretical SRXPS results. (a) Experimental results taken at $\hbar\omega$ = 1253.6 eV. (b) Theoretical results. Lines were convoluted with Gaussian (FWHM=1.6 eV) and Lorentzian (1.5 eV FWHM at A and B, 2.5 eV at C) lineshapes to simulate instrumental and lifetime broadenings. (c) Theoretical and experimental spin polarizations, multiplied by 2.5 for clarity.

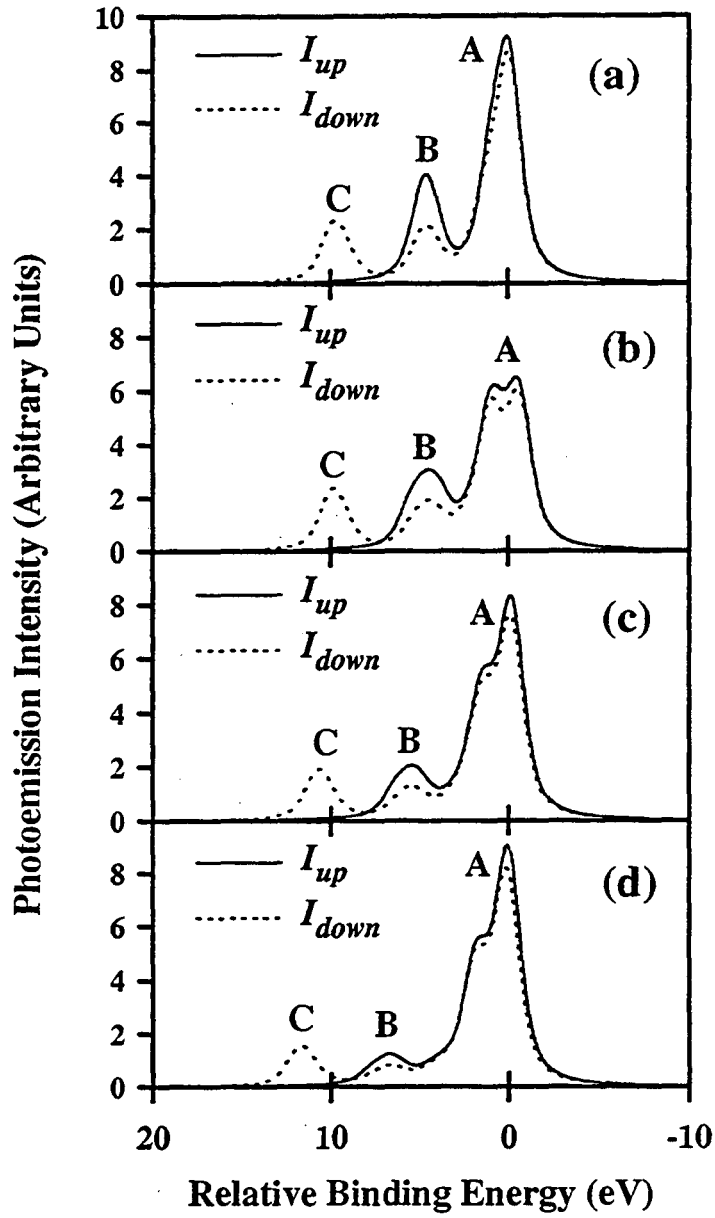

Figure 4.2: Theoretical spin-polarized photoemission spectra, with spin-up (down) corresponding to minority (majority) photoelectrons. All lines were broadened with Gaussian (FWHM=1 eV) and Lorentzian (FWHM=1 eV) lineshapes. (a) SRXPS for zero core-level spin-orbit splitting, and zero valence bandwidth. (b) SRXPS for $3p$ spin-orbit splitting of 1.74 eV, and zero valence bandwidth. (c)-(d) SRXPS for 1.74 eV spin-orbit splitting, with 50% and 100% valence bandwidth, respectively.

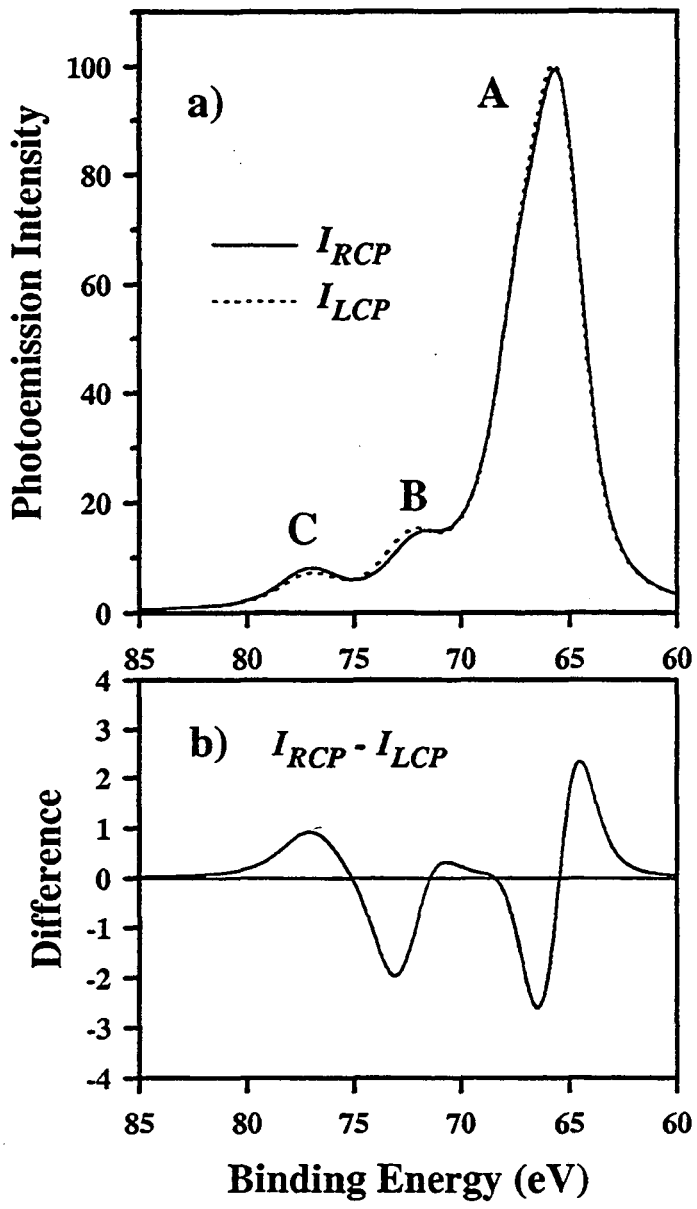

Figure 4.3: Theoretical MCDAD results. (a) Spin-integrated results for RCP and LCP excitation. (b) Difference spectrum. Lines were broadened with Gaussian (FWHM=1.6 eV) and Lorentzian (1.5 eV FWHM for A and B, 2.5 eV for C) lineshapes.

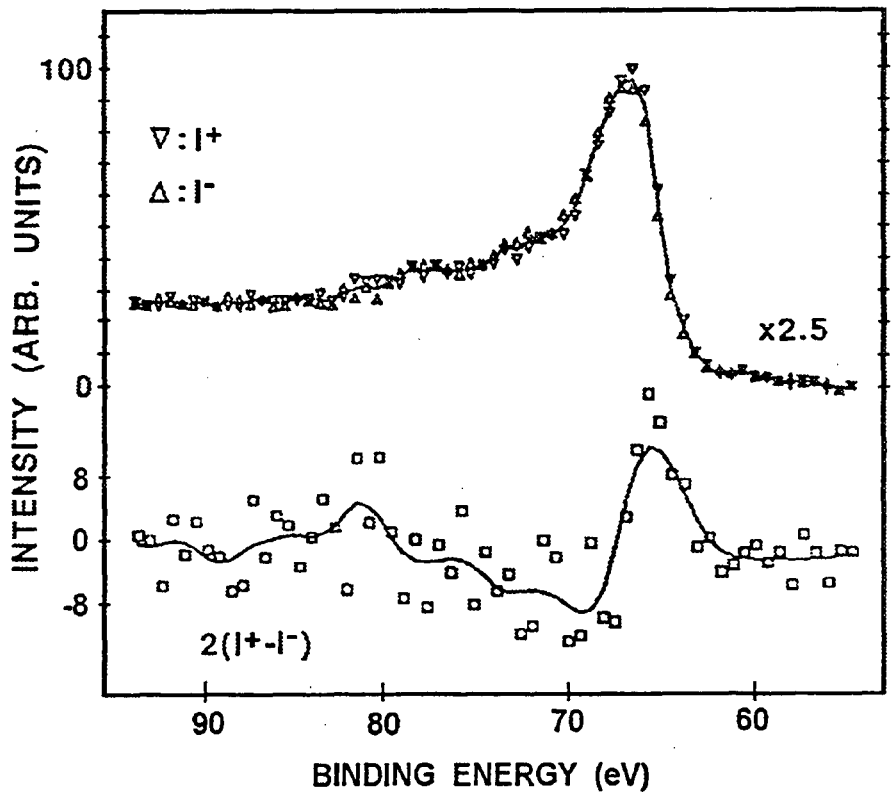

Figure 4.4: Experimental MCDAD results due to van der Laan *et al.* (Ref. 75). In the top panel, experimental Ni $3p$ photoemission intensities I^+ and I^- using circularly polarized x-rays with the projected photon helicity parallel (∇) and antiparallel (Δ), respectively. In the bottom panel, $2(I^+ - I^-)$ gives the MCDAD $I_R - I_L$.

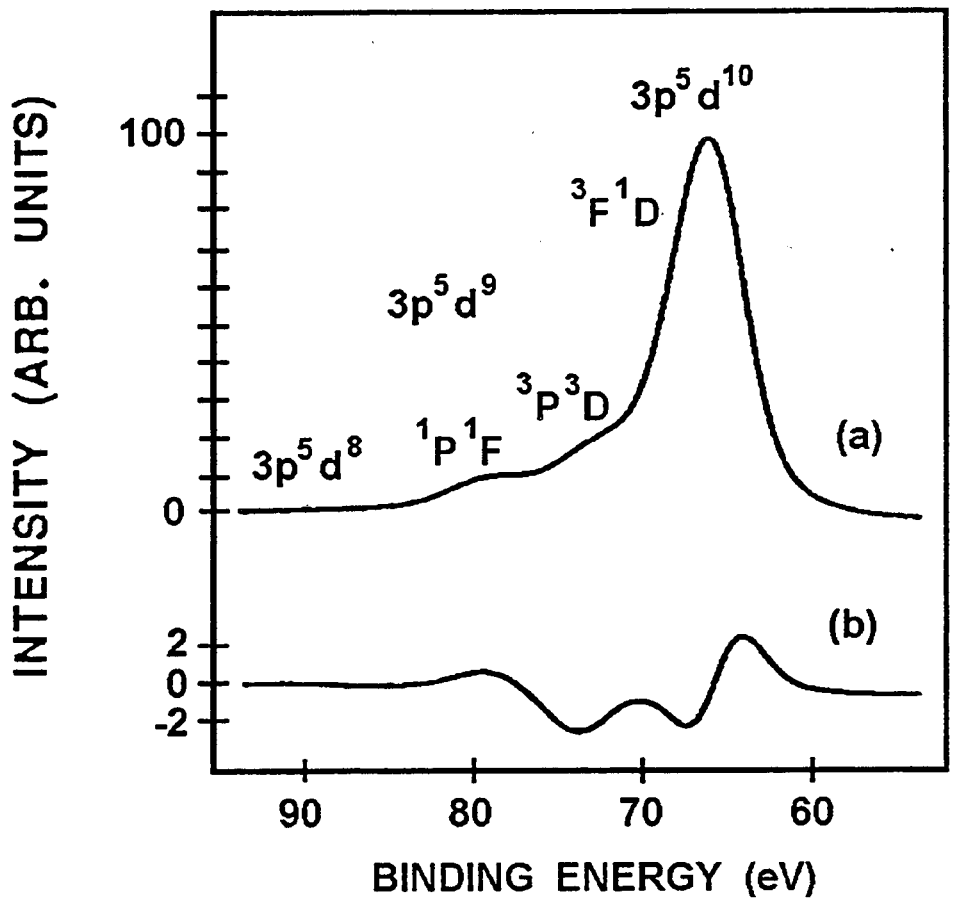

Figure 4.5: Theoretical MCDAD results for Ni $3p$ due to van der Laan *et al.* (Ref. 75). (a) Spin-integrated spectrum averaged over RCP and LCP excitation. Results were calculated using an Anderson impurity model with ground state d weights 18% d^8, 49% d^9, and 33% d^{10}. (b) Difference spectrum $I_R - I_L$. Lines were broadened with a Gaussian of 2.66 eV FWHM and a Lorentzian of 4.0 eV FWHM.

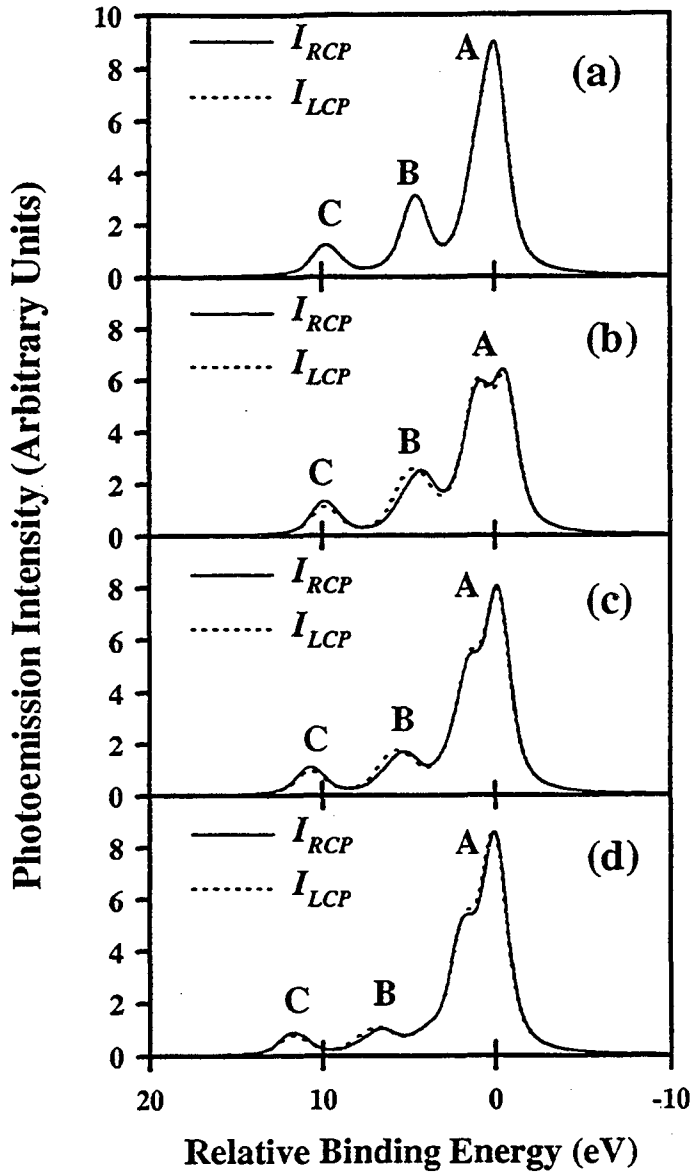

Figure 4.6: Theoretical spin-integrated photoemission spectra for RCP and LCP excitation. All lines were broadened with Gaussian (FWHM=1 eV) and Lorentzian (FWHM=1 eV) lineshapes. (a) Spectra for zero core-level spin-orbit splitting, and zero valence bandwidth. In the absence of spin-orbit interaction, the MCDAD signal vanishes. (b) Spectra for $3p$ spin-orbit splitting of 1.74 eV, and zero valence bandwidth. (c) - (d) Photoemission spectra for 1.74 eV spin-orbit splitting, at 50% and 100% valence bandwidth, respectively.

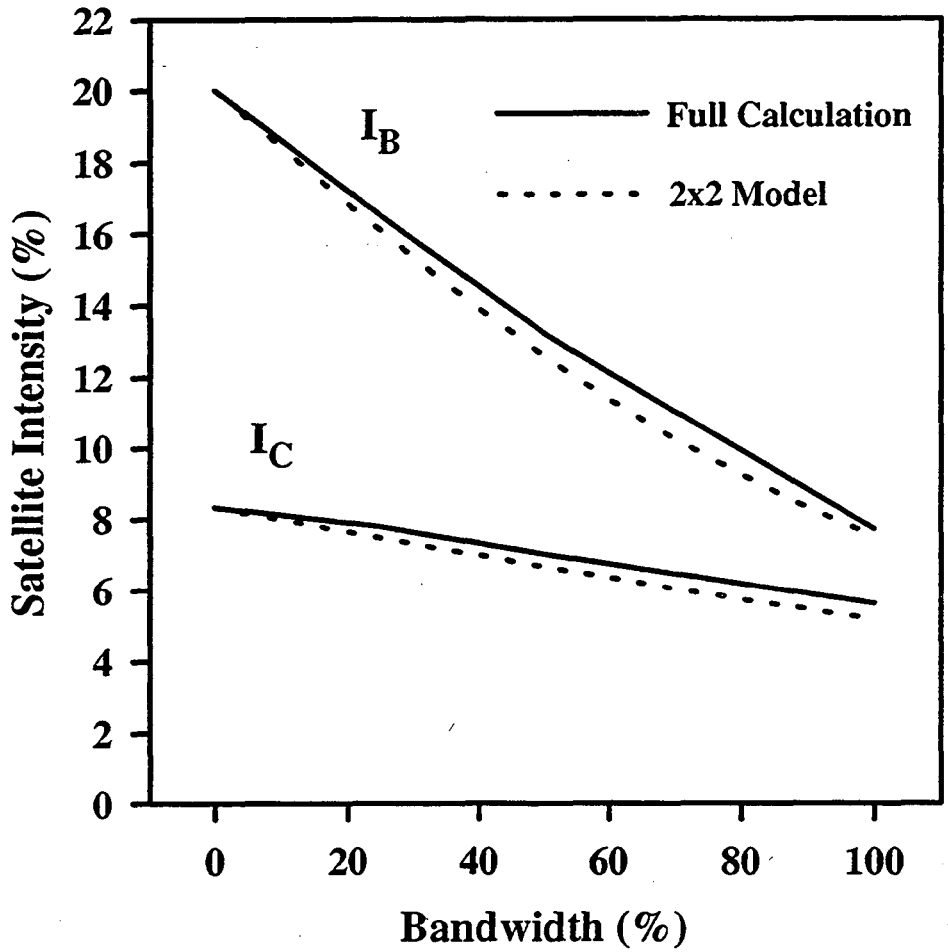

Figure 4.7: Spin-integrated intensities of satellites B and C as a function of valence bandwidth, for unpolarized excitation. Satellite intensities are given as a percent of total Ni $3p$ line strength. The solid lines are the result of an exact numerical integration using the full many-body calculation. The dashed lines are the results of a simple 2x2 model (see text), using $\tau = 0.80$ for satellite B and $\tau = 0.41$ for satellite C.

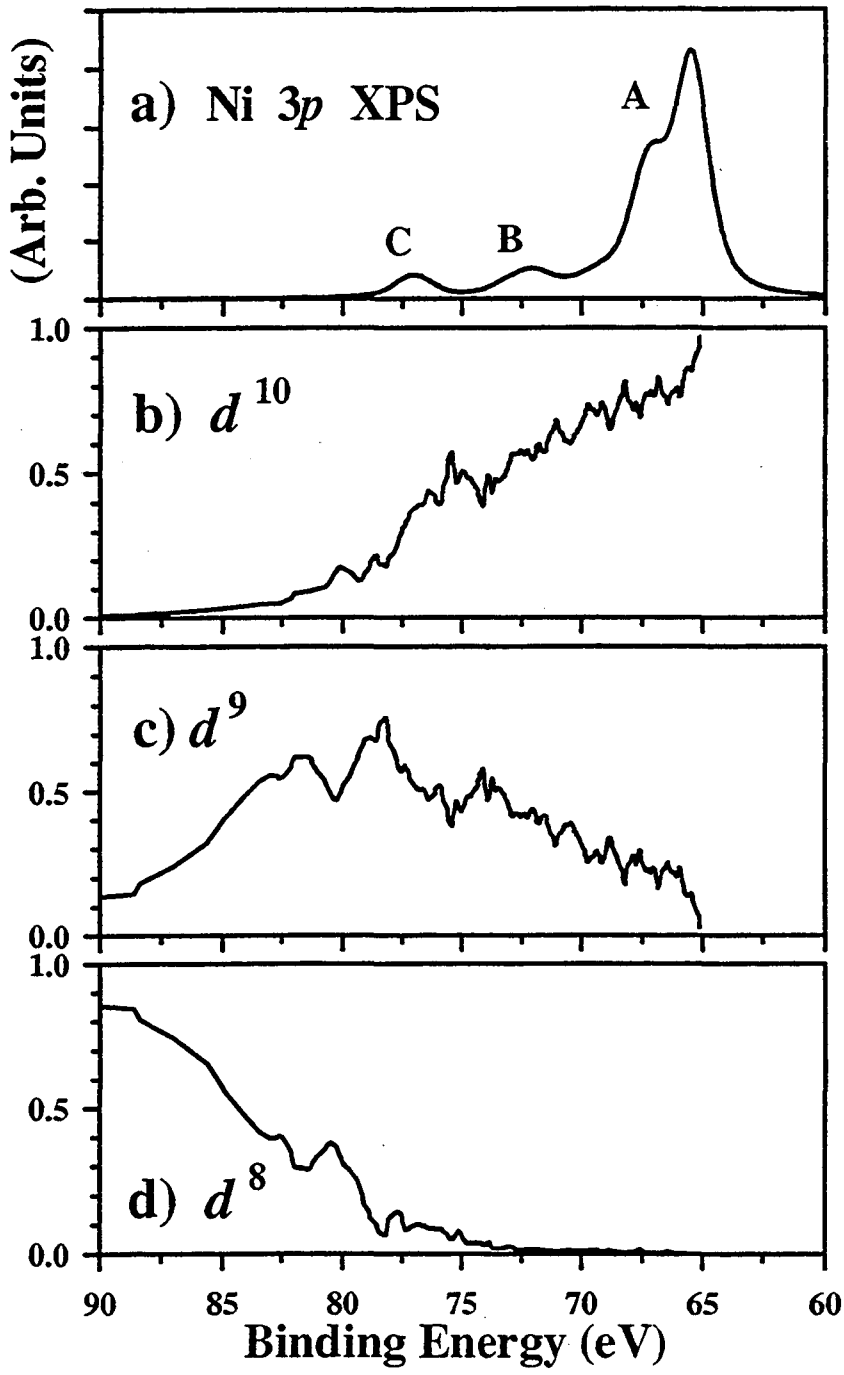

Figure 4.8: Local final-state configuration. (a) Ni $3p$ spin-integrated results for unpolarized excitation. (b) - (d) Fraction of d^{10}, d^9, and d^8 local final-state configuration as a function of binding energy.

Chapter 5

On the Enhancement of the Ni Surface Orbital Moment

5.1 Introduction

Since the earliest demonstration of magneto-optical effects in photoemission from ferromagnetic surfaces [21, 40], it has become apparent that some fundamental problems of surface magnetism may be investigated with such techniques. In a photoemission experiment one can fully characterize the final state of the photoelectron by measuring its energy, k-vector and spin. Both circular- and linear-polarized excitation can further be used to probe the magnetic order at surfaces and interfaces [45, 49, 48, 80]. With the use of linearly polarized radiation, angular selection of the photoelectrons is required in order to define a chirality between the vectorial quantities of the photoemission experiment [22, 41, 81]. Accordingly, such effects have been referred to as linear magnetic dichroism in the angular distribution, or MLDAD.

The great interest in magneto-optical effects in core-level spectroscopy is connected with the promise of developing an atom-specific surface/interface magnetometry [82]. This implies that the method must be understood at a quantitative level, and it must provide reliable measurements of spin and orbital magnetic moments of the surface and interface atoms. This quantitative analysis is lacking in the case of conventional magneto-optic effects, i.e., the Faraday and Kerr effects which involve transitions sampling the joint density of states of the ferromagnetic material [83]. The search for magneto-optical effects in higher-energy spectroscopies has produced the important technique of magnetic circular dichroism in X-ray absorption (XMCD) [84], which involves

transitions from atomic-like core states to unoccupied states in the valence band. Optical transition sum rules have been developed which relate the orbital and spin moments to the dichroic X-ray absorption intensity, in an atom-specific and chemically sensitive way, with reasonable accuracy, and such measurements have been used to measure both spin and orbital moments [85]. Dichroism in core-level photoemission, by contrast, involves transitions to free-electron states and can be qualitatively understood within a simple atomic photoionization model, which accounts for the main features measured in Fe $3p$ and Fe $2p$ core levels [45, 41, 86]. However, beyond this qualitative understanding, there is a compelling need to deepen the quantitative understanding of the magneto-optic dichroism in photoemission, and of the solid state effects involved, with the aim of developing a truly surface sensitive magnetometry.

Electron spectroscopy of Ni has been the test-bench for many important improvements in the understanding of correlated narrow-band systems, since spin-polarized final-state satellites are present in both the valence band and the core-level spectra, and these can only be explained in terms of many-body interactions [87]. Surface sensitive experiments on Ni are also challenging due to the high reactivity of the free surface. Nonetheless, recent experiments on Ni core levels with spin resolution [27] or circular-polarized excitation [75] have clearly shown the distribution of intensity over a complex satellite manifold for both Ni $2p$ and Ni $3p$ core levels. In a recent pioneering study, van der Laan *et al.* measured circular dichroism for Ni $3p$ at a photon energy of $h\nu =$ 400 eV and calculated the dichroism in an Anderson impurity model [75]. They found that the calculation severely underestimated the experimental dichroism, and this was interpreted as evidence of a significantly enhanced orbital moment for the surface and near-surface Ni atoms contributing to the surface sensitive photoemission spectra. The possibility of an enhanced surface orbital moment arises from theory [88] and from the presence of perpendicular magnetization for some ferromagnetic surfaces [89]. On the

other hand, $L_{2,3}$ X-ray circular dichroism experiments on Ni layers grown on Fe(100) [90] showed that the total magnetic moment is *reduced* at monolayer thickness and converges to the bulk Ni values for thicknesses of 4-6 monolayers, when the epitaxial strain starts to relax. This result was based on the application of the magneto-optic sum rules for XMCD. It is therefore clear that the fine details of the surface structure, i.e. relaxation, tetrahedral distortion, interface strain, etc., can cause changes of the spin and orbital moments for the surface atoms which may differ substantially with respect to bulk matter.

5.2 Results

Here we present data obtained by MLDAD on a thin layer of Ni grown on Fe(100). The Ni thickness is of the order of 20 monolayers, which assures the relaxation of the film to the stable *fcc* structure, although some residual stress from the epitaxial interface may be present in the deeper layers of the film. The sample was grown *in situ* by e-beam deposition on a room temperature substrate. The residual gas pressure was of the order of $5\text{x}10^{-10}$ mbar during growth and $2\text{x}10^{-11}$ mbar during measurements. The surface contamination was probed by core-level and valence-band photoemission at UV energies where the sensitivity to CO photoemission is maximum. Clean Ni surfaces could be maintained and measured for several hours. Ni $3p$ photoemission spectra were measured in the geometries sketched in the inset of Fig. 1. The linearly polarized radiation of the SU3 undulator of the SuperAco storage ring at Orsay was monochromatized by a plane grating monochromator and impinged at 45° from the surface normal. The photon energy was 160 eV, leading to Ni $3p$ photoelectrons at $\sim 80 - 100$ eV and greater surface sensitivity than the prior work by van der Laan *et al.* [75]. The normal emission photoelectrons were accepted by an hemispherical electrostatic energy analyzer with $\pm 1°$ angular resolution; the overall energy resolution was $\sim$ 100 meV. The Ni film

was exchange coupled to the Fe(100) substrate whose in-plane magnetization, perpendicular to the photoemission reaction plane, could be oriented up or down. The two orientations of the magnetization vector determine the two mirror experiments which define the MLDAD dichroism spectrum. The relaxed Ni film is polycrystalline, although some texture may exist. This is an important requirement if one wishes to compare the dichroism calculated in an atomic model to the experimental dichroism, which is defined here as $MLDAD = (I_{up} - I_{down})$, where $I_{up(down)}$ is the photoelectron spectral intensity obtained with the magnetization in the up (down) direction. That is, large directional effects have been measured in Fe and Co MLDAD from single-crystal surfaces, which can be explained in terms of photoelectron diffraction effects [34, 42]. These MLDAD modulations can be so large that the dichroism may vanish at some combined angle and energy, or even undergo a change of sign. The present experiment integrates over all the hidden chiralities that modify the photoelectron transport towards and through the surface due to the integration over the misaligned grains of the polycrystalline film, so that only the external chirality between the vectors describing the photoemission experiment is active. The spectra exhibit pronounced satellite structures, and these structures display a large dichroism. The experimental curves are presented in the top panel of Fig. 1. The central panel shows the spectra after an integral background subtraction, and the bottom panel shows the difference between the two spectra measured in the mirror experiments. The noise level in the difference spectrum is estimated at 10%.

In our calculation we employ the same small-cluster model which has been used previously to successfully describe both the valence band [53] and the $2p$ core-level [38, 39] photoemission spectra of Ni. The model consists of a small tetrahedral cluster of four atoms, with periodic-boundary conditions imposed to generate the full *fcc* lattice. All Bloch states with such periodicity must transform according to Γ or X in the Brillouin zone. Each atom in the lattice can be labeled by an index 1-4, and is surrounded by

twelve nearest neighbors of a different index. Therefore, same-site and nearest-neighbor interactions are treated quite accurately in this approach, and due to the highly localized nature of core electrons and the $3d$ valence electrons, these are expected to give rise to the dominant effects in Ni.

As our basis set, we use ten $3d$ spin-orbitals per site to model the valence electrons, and six $3p$ spin-orbitals for the core electrons. The Hamiltonian used in the present work has been described elsewhere [38, 39]. Briefly, it contains terms describing the hopping of the valence holes, the spin-orbit splitting of the core level, and Coulomb repulsion between two holes on the same site. Valence hole hopping, which gives rise to extra-atomic screening effects, is described in terms of the Ni band structure. One hole in the valence band can occupy any of 20 $3d$ spatial orbitals. These states decompose with the following space group symmetries:

$$\Gamma_{12} \oplus \Gamma'_{25} \oplus X_1 \oplus X_2 \oplus X_3 \oplus X_5. \tag{5.1}$$

We match the energies of these Bloch states to the spin-averaged band structure calculations of Wang and Callaway [56]. In this way, the screening is described without resorting to adjustable parameters. The intrasite repulsion for two valence holes is described by the Slater integrals U_{dd}, F^2_{dd} and F^4_{dd}, whereas the core-valence repulsion is described by Slater integrals $U_{pd}, G^1_{pd}, F^2_{pd}$, and G^3_{pd}. For all the F and G integrals, as well as the spin-orbit coupling strength, the values of previous workers [76] are adopted. For the direct Coulomb term U_{dd} we use 3 eV, although this term has almost no effect on the calculated spectra due to the domination of both the initial and final states by d^9 and d^{10} configurations. Therefore, the only truly adjustable parameter in our Hamiltonian is the direct Coulomb term U_{pd}. This important parameter determines the relative energy difference between the d^9 and d^{10} final-state configurations, which in turn determines the satellite positions. We obtain good agreement with experiment using U_{pd}=5 eV. For

present purposes, valence band spin-orbit splitting is assumed to be small and is not included.

We solve for the Ni ground state within our model by placing two valence holes on the four-atom cluster. We find that the many-body ground state results from placing both holes in Bloch states at X_5 in the Brillouin zone, and has overall symmetry $^3X_2$. The ground state is thus 50% d^9 and 50% d^{10}, leading to a spin moment of 0.50 μ_B per atom that is in excellent agreement with prior band structure calculations [56]. Due to the vanishing valence spin-orbit splitting used here, the orbital moment in the ground state of our model is identically zero. With the ground state thus defined, we obtained the spectra using Fermi's golden rule and the sudden approximation to calculate the transition probabilities between the ferromagnetic ground state and the final states which contain a core hole and an outgoing photoelectron. The resulting lines were convoluted with Lorentzians and Gaussians of HWHM 0.75 eV and 0.50 eV respectively, with these chosen to best fit experimental lineshapes.

In Fig. 2 we present theoretical angle-resolved spectra calculated for both magnetic orientations (I_{up} and I_{down}), for the same geometry shown in the inset of Fig. 1(a). Overall, the calculated spectra agree very well with the experimental results of Fig. 1(b). The main line contains much internal structure, consisting of final states which are nominally $p_{3/2}d^{10}$ and $p_{1/2}d^{10}$, but also ^3F and ^1D multiplets derived from the p^5d^9 configuration. The bump at $\sim$ 87 eV is due to p^5d^9 multiplets derived from ^3P and ^3D terms, and the broad peak at $\sim$ 82.5 eV is due to ^1P and ^1F terms.

In Fig. 1(b) we present the difference spectrum $I_{up} - I_{down}$, which also compares well with the experimental results of Fig. 1(c). The calculated dichroism exhibits four prominent features: a broad plus feature at the $^1F^1P$ peak, a broad minus feature at the $^3D^3P$ peak, and a sharp minus-plus feature at the main line.

Notably, the calculated dichroism is *larger* than the experimental dichroism. In the

work of van der Laan *et al.*, the calculated dichroism was *smaller* than the measured dichroism by a factor of 2.5 [75]. It was argued that this could only be explained as due to a strongly enhanced surface orbital moment for Ni. Our results here do not support these earlier conclusions, i.e., *our calculated dichroism is larger than the experimental dichroism even using a ground state that has zero orbital moment.*

We provide two possible reasons to account for this apparent discrepancy. Firstly, the Ni $3p$ main line actually contains considerable structure, as discussed above. Thus, the calculated linewidth is due to an intrinsic structure as well as Lorentzian and Gaussian broadenings to incorporate both lifetime and instrumental effects, respectively. Reducing these broadenings will greatly enhance the intrinsic differences, and lead to a much larger dichroism. In their work, van der Laan *et al.* used much larger line broadenings of 2.0 eV HWHM (Lorentzian) and 1.33 eV HWHM (Gaussian). We calculated the dichroism with the same broadenings as used by van der Laan *et al.*, and then recalculated it with the smaller broadenings used in this work, and found that the calculated dichroism increased by a factor of 4. It appears therefore that the magnitude of the calculated dichroism depends strongly on the line broadening which is adopted in the calculation, and that a careful analysis of the integral spectra must be the guideline for the choice of the maximum allowed broadening of the calculated spectra. Here we present a calculation which intentionally overestimates slightly the FWHM of the $3p$ main line (it is 3.4 eV for the calculated spectra and 3 eV for the experimental spectra). As a result, we can safely say that the larger dichroism calculated here is not due to artificially narrow lineshapes. Therefore, although the present data cannot exclude the possibility of an enhanced surface orbital moment for Ni, such an enhancement is *not required* in order to explain the experimental data.

A second possible explanation to account for the apparent contradiction between the present results and those of van der Laan *et al.* is connected to differences between

the experiments. Van der Laan's experiment was done on a Ni (110) single crystal, with the sample magnetized in the surface plane along the $[1\bar{1}1]$ direction. The plane of measurement contained the surface normal and the magnetization axis. However, such a plane is not a plane of mirror symmetry, and it is known that photoelectron diffraction effects can have a large, even dominating effect on the measured dichroism in such cases [91]. The present experiment, due to the polycrystalline sample, does not suffer from such effects. From this point of view, the present data represent an improvement of the experimental information on Ni 3p MLDAD. In addition, the present calculation both reproduces all the features of the difference spectrum and sets a lower limit on the theoretical value of the MLDAD, which is larger then the measured one.

In conclusion, we have measured the Ni $3p$ magnetic dichroism using linear p-polarized synchrotron radiation and with greater surface sensitivity than in a prior study, and calculated the dichroism by means of a small-cluster many-body approach. Even using a ground state with zero orbital moment, the calculated dichroism was found to be larger than the measured one. Thus, our findings do not support an earlier analysis of Ni $3p$ magnetic dichroism that required the existence of an enhanced surface orbital magnetic moment.

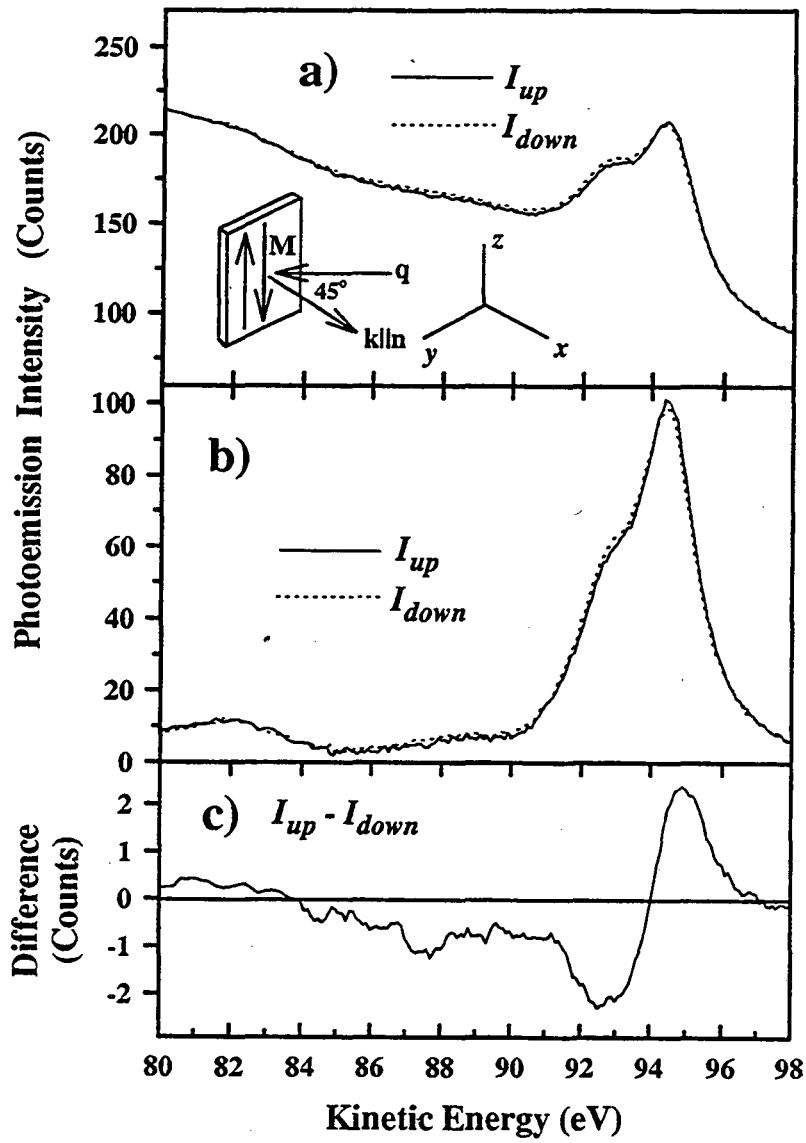

Figure 5.1: Ni $3p$ experimental results. (a) Raw data for magnetization up (I_{up}) and down (I_{down}), with inset showing geometry. Linearly p-polarized photons $\mathbf{q}$ of 160 eV energy impinge in the xy plane, making an angle of 45° with the photoelectron $\mathbf{k}$, which coincides with the surface normal. (b) Background subtracted experimental spectra, normalized to a peak intensity of 100. (c) MLDAD difference spectrum between I_{up} and I_{down}. Data were smoothed by one cycle of five-point averaging.

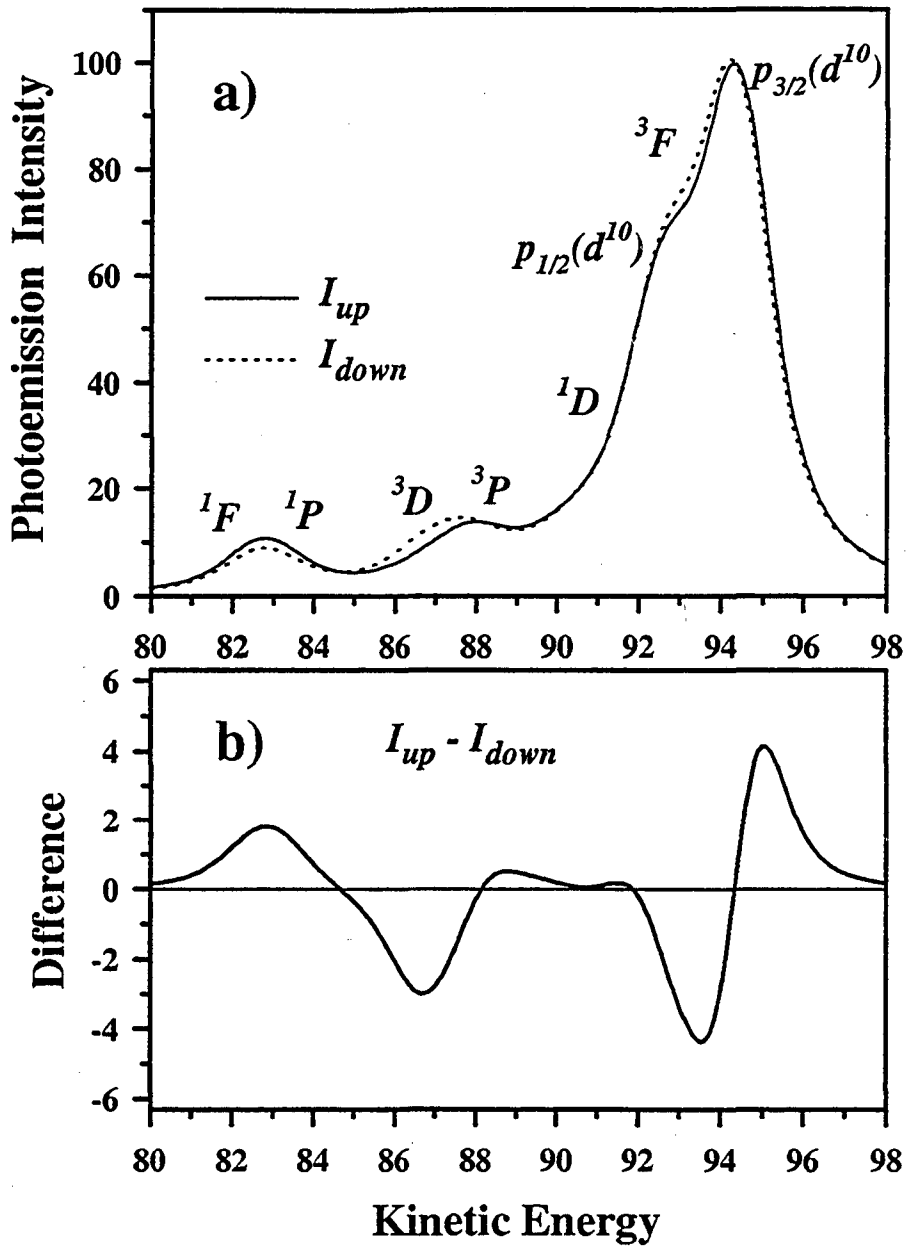

Figure 5.2: Theoretical results for bulk Ni. (a) Ni $3p$ angle-resolved spectra for magnetization up (I_{up}) and magnetization down (I_{down}), for the geometry shown in inset of Fig. 1(a). Spectra were Gaussian (HWHM=0.50 eV) and Lorentzian (HWHM=0.75 eV) broadened, and normalized to a peak height of 100. (b) Calculated dichroism $I_{up} - I_{down}$.

Chapter 6

Photoelectron Diffraction Effects in Magnetic Dichroism

6.1 Introduction

Magnetic dichroism in core-level photoelectron emission from solids represents a promising new probe of surface and interface magnetic order It has been shown recently that, for magnetic solids, the *spin-integrated* photoelectron intensity in a given direction can depend on the direction of the long-range magnetization, leading to one kind of magnetic dichroism [21, 22]. This is found to occur when the photoelectrons are excited by circular-polarized radiation, leading to magnetic circular dichroism (MCD) [21], as well as by p-type linear- polarized radiation (MLD) [22]. In such dichroism experiments, the photon- electron geometry can be held fixed, and the magnetization simply switched from being parallel ($M \uparrow$) to anti-parallel ($M \downarrow$) to some special axis, with the dichroic asymmetry then being measured from the two different intensities $I_{M\uparrow}$ and $I_{M\downarrow}$ as: $A = (I_{M\uparrow} - I_{M\downarrow})/(I_{M\uparrow} + I_{M\downarrow})$.

From symmetry considerations, it can also be shown that MLD effects occur only in angle-resolved photoemission, and that they disappear with integration over emission angle [58]. Accordingly, this effect has been referred to as magnetic linear dichroism in angular distributions (MLDAD). Such effects have also more recently been observed with unpolarized radiation, where they can be termed MUDAD [23, 92]. The fact that the photoelectron intensity with unpolarized radiation (I_{unp}) can be simply related to those with both s and p linear, and right and left circular, polarizations via $I_{unp} = I_s + I_p = I_{rcp} + I_{lcp}$ also makes clear the close connections among them. Thus, unpolarized light

contains the p component producing MLDAD, and MUDAD can be viewed as a special manifestation of MLDAD. MCD was immediately explained in terms of the selection rules for dipole-allowed transitions from *initial states* that are split by both spin-orbit and exchange effects, with the latter being directly related to the magnetization of the sample [21]. The potential importance of photoelectron diffraction effects in the *final states* of the excitation have also been pointed out [91, 93] and such effects have been shown to play a role in MLDAD [78]. However, a complete understanding of MLDAD and MUDAD including both initial-state and final-state effects is yet to be obtained. In the present investigation, we explore magnetic dichroism occurring with unpolarized radiation in a different experimental geometry, and find that a more general model including both initial- and final- state effects is essential for interpretation. The particular example treated is higher-energy unpolarized x-ray excitation such that strong forward scattering effects arise in the resulting photoelectron angular distributions (AD) [28].

The first quantitative explanation of core-level MLDAD was made by Rossi *et al.* [41], who treated core spectra of a single free atom. They simulated ferromagnetic alignment by fixing the orientation of the atomic magnetic moment and found good agreement with the experimental data of Roth *et al.* [22]. Van der Laan *et al.* [94] further predicted that the intensity difference obtained for the two magnetization directions should scale with $|\vec{M}\cdot(\vec{k}\mathrm{x}\vec{\mathrm{E}})(\vec{\mathrm{k}}\cdot\vec{\mathrm{E}})| \sim \sin 2\theta$, where $\vec{M}$ is the magnetization, $\vec{k}$ is the photoelectron wave vector, $\vec{E}$ is the electric field vector of the light, and θ is the angle between $\vec{k}$ and $\vec{E}$. In these free-atom models, there can be no dependence of the dichroism on the emission direction with respect to a crystal lattice. Recently, the dependence of the dichroism on the angle θ has been investigated [78, 95]. In the latter experiment [95], as $\vec{k}$ was varied, the sample also was rotated to keep the relation between the emission direction and the crystallographic directions constant. The $\sin 2\theta$ dependence was

found to be correct, confirming one of the predictions of the atomic model. In the former experiment [78], the directions of $\vec{E}$ and $\vec{M}$ were kept fixed in space, and photoelectrons emitted from the sample in narrow angular intervals were collected by a multichannel photoelectron detector. Accordingly, two quantities were changed simultaneously: the angle θ and the emission direction with respect to the crystallographic directions. An overall $\sin 2\theta$ dependence was observed here also, but it was found to be modulated by fine structure that was successfully explained by considering photoelectron diffraction effects in the crystal lattice [78]. Fanelsa *et al.* [23, 92] have also observed that the dichroic asymmetry changes sign when varying the photoelectron emission angle with respect to the crystal lattice while keeping all the other parameters fixed with respect to one another. Thus, the single-atom model for MLDAD is not adequate to describe all of the effects observed previously.

6.2 Results

In the present investigation, we have varied only the emission direction with respect to the crystal lattice, while keeping the geometrical conditions between $\vec{M}$, $\vec{k}$, and $\vec{E}$ constant; this serves to focus on photoelectron diffraction as the only source of dichroism. This was achieved simply by rotating the sample about the direction of the magnetization, as shown schematically in Fig. 6.1(a). $\vec{M}$ was perpendicular to both light incidence and $\vec{k}$, with the angle between the latter two being fixed at 45°. For each setting of the rotation angle α, an energy distribution curve (EDC) covering the entire Fe $2p$ core level spectrum was collected, as shown in Fig. 6.2(a). A large range in α was spanned to obtain an overview of the behavior of the dichroism in this parameter space. We used a standard X-ray source emitting unpolarized Mg $K\alpha$ radiation (1253.6 eV) and a commercial hemispherical electrostatic analyzer accepting electrons over a cone with about a 5° full acceptance angle. The overall energy resolution was 0.9 eV as

judged from the width of the Ag Fermi edge. The samples were 2 nm thick epitaxial bcc Fe(001) films grown *in situ* on Ag(001) in UHV conditions, with an in-plane easy magnetization direction ($x =< 100 >$) coinciding with the axis of rotation. The films were magnetized in the $+x$ or -x direction by short field pulses of about 80 Oersted which were applied after each energy scan at a preset value of α.

Fig. 6.2(a) shows Fe $2p$ energy distribution curves for magnetization along $+x$ (solid lines) and -x (dashed lines) for emission slightly off normal ($\alpha = -2°$). Fig. 6.2(b) shows the corresponding asymmetry, and constitutes part of a larger MUDAD data set on the (α, E_b) grid, with E_b denoting the binding energy. The peak-to-peak value is approximately 5%, which is comparable in magnitude to the results obtained earlier with linearly polarized radiation at $h\nu = 879$ eV [42]. The maximum of the dichroism occurs at 0.65 eV smaller binding energy than the peak of the $2p_{3/2}$ intensity. The $2p_{3/2}$ and $2p_{1/2}$ lines show asymmetries with opposite energy dependence, with that of the $j = \frac{3}{2}$ sublevel being much stronger than that of the $j = \frac{1}{2}$ sublevel; this is qualitatively similar to what has been seen with circular-polarized excitation of Fe $2p$ [21]. The asymmetry does not vanish between the two sublevels, also in qualitative agreement with prior experiments using linearly polarized light [42].

Fig. 6.3(a) shows simultaneously the full set of intensity and asymmetry data for the Fe $2p_{3/2}$ region of the spectrum in the form of a 3D plot of $I(\alpha, E_b)$, with the surface being shaded according to the value of the asymmetry (light = +, and dark = -). The intensity surface displays the usual photoelectron diffraction (PED) peaks occurring at emission angles of $\alpha = 0°, 25°$, and 45° that are well-known to be due to strong forward scattering along the $< 001 >$, $< 012 >$, and $< 011 >$ directions, and which should ideally occur at $\alpha = 0°, 26.5°$, and 45° for rotation about $< 100 >$ [28]. Directly along these emission angles, the dichroism is very small, but it exhibits sign changes around each of them as α is varied. Fig. 6.3(b) shows in more detail the region of Fe $2p_{3/2}$ emission

near the $< 001 >$ surface normal; here, the contour plots of the intensity (indicated as dashed lines) are overlaid with a shaded contour plot of the asymmetry (indicated by various grey levels). The maximum of the dichroism occurs at an emission angle $\alpha = -8°$ and a binding energy of 706.2 eV and the minimum at $\alpha = +6°$ and the same binding energy. The signs of the asymmetry pattern on the high-binding energy side of the $2p_{3/2}$ intensity peak are also opposite to those on the low-binding energy side, yielding a second type of sign change. Combined with the angular dependence of the dichroism, this leads to a characteristic "chessboard" pattern that is nearly centered in (α, E_b) along the forward scattering peak. The same pattern is found around each of the forward scattering peaks in Fig. 6.3(a). Similar behavior is observed in Fe $2p_{1/2}$ and Fe $3p$ MUDAD data not shown here.

The fact that the *sign* of the dichroism depends on the emission angle with respect to low-index directions in the crystal lattice immediately indicates that photoelectron diffraction is a primary factor, as the relations between $\vec{M}$, $\vec{k}$, and $\vec{E}$ which in a single-atom picture exclusively determine the dichroism are not affected by the rotation in the present experiment. We thus consider a more quantitative model of these high-energy MUDAD effects which includes photoelectron diffraction within a well-established atomic cluster model [96, 97] that has recently been generalized to calculate all forms of dichroism (CDAD in non-magnetic systems [91, 93], as well as MCDAD, and ML-DAD/MUDAD [91, 93]). We have carried out calculations of the Fe $2p_{3/2}$ intensity from a simple two-atom Fe cluster (one emitter and one scatterer) with interatomic spacing of 0.287 nm to represent the $< 001 >$ direction that is in the center of Fig. 6.3(b) at $\alpha = 0°$. Correct interference of the s and d photoelectron channels was also included, although spin-orbit scattering of the photoelectron (which has been found to be negligible in prior photoelectron diffraction calculations [28, 91, 93, 96, 97]) was not. The four m_j sublevels of the $j = \frac{3}{2}$ manifold were assumed to be separated from one another by an empirical

exchange splitting of 0.30 eV that has been used to correctly describe both MCDAD and spin polarization data for Fe $2p$ [21, 91, 93], and the levels finally broadened using a Doniach-Sunjic lineshape (FWHM of 1.0 eV and singularity index of 0.44) that has been employed previously to simulate such spectra [25]. Calculations were performed for both orientations of the magnetization, and the resultant asymmetry thus calculated. A plot of these theoretical results analogous to Fig. 6.3(b) is shown in Fig. 6.3(c), and we see that the chessboard pattern is correctly predicted. Simple photoelectron diffraction theory is thus able to predict the characteristic pattern seen in these MUDAD results. Including interference between the s and d channels is *not* essential for producing the chessboard pattern, as was verified by carrying out a calculation with the dominant d channel only. This $s-d$ interference does however produce the shift in the zero line of the asymmetry as a function of α, which is exactly along $\alpha = 0°$ with only the d channel included.

A more heuristic picture of the underlying physics is also possible. We consider for simplicity the case of d-channel emission only from the same two-atom cluster, with geometry as shown in Fig. 6.1(b). In the dipole approximation, the p-component of the unpolarized light (the s-component does not contribute to MUDAD) yields photoelectron amplitudes for the $\left|\frac{3}{2}, \pm\frac{3}{2}\right\rangle$ core states that are proportional to $1 + 3e^{\pm 2i\phi}$, where ϕ is the electron emission angle (see Fig. 6.1b). The amplitudes of the primary waves at the electron detector are thus $1 \pm 3i$ for photoelectrons derived from the $\left|\frac{3}{2}, \pm\frac{3}{2}\right\rangle$ states, respectively. At the scatterer $\phi = 45° + \alpha$, so the amplitudes of the same primary waves at the scattering site are $1 \pm 3ie^{\pm 2i\alpha}$. The amplitudes $\tilde{A}$ of the scattered waves at the electron detector are thus proportional to:

$$\tilde{A}_{\left|\frac{3}{2},\, \pm\frac{3}{2}\right\rangle} = \left(1 \pm 3ie^{\pm 2i\alpha}\right) |f(\alpha)|\, e^{i\delta(\alpha)} \,, \tag{6.1}$$

where $|f(\alpha)|$ is the magnitude of the scattering factor, and $\delta(\alpha)$ is the *total* phase shift

due to scattering and path-length difference. The key to producing the chessboard dichroism pattern is the fact that the primary waves from the $|j,\ \pm m_j\rangle$ both suffer the *same* overall phase shift $\delta(\alpha)$ at the scattering site. The total amplitude at the electron detector is the sum of the primary and scattered waves, leading to an intensity difference between the two levels that is finally proportional to:

$$I_{|\frac{3}{2},\frac{3}{2}\rangle} - I_{|\frac{3}{2},-\frac{3}{2}\rangle} = 12\,|f(\alpha)|\sin\delta(\alpha)\,[1 - \cos 2\alpha - 3\sin 2\alpha]\ . \tag{6.2}$$

The same calculation for the $m_j = \pm\frac{1}{2}$ levels yields the result:

$$I_{|\frac{3}{2},\frac{1}{2}\rangle} - I_{|\frac{3}{2},-\frac{1}{2}\rangle} = 4\,|f(\alpha)|\sin\delta(\alpha)\,[1 - \cos 2\alpha - 3\sin 2\alpha]\ . \tag{6.3}$$

When the magnetization direction is reversed, the intensity of each sublevel remains unchanged, but the energetic positions of the $|j,\ \pm m_j\rangle$ core states are simply interchanged due to the exchange splitting. Therefore, equations (2) and (3) give precisely the (unnormalized) MUDAD asymmetry, and it is qualitatively clear from the functional form that the chessboard pattern should result. These equations were then used to simulate the asymmetry via appropriate exchange splitting of levels and energy broadening, and we find that the characteristic chessboard pattern in the asymmetry is very well reproduced by considering only d-channel emission in this simple picture, although these results are not shown here. The proportionality to $|f(\alpha)|\sin\delta(\alpha)$ in equations (2) and (3) also makes it clear that such MUDAD asymmetry requires scattering and diffraction: in the absence of scattering, $|f(\alpha)|$ is identically zero.

Finally, in order to obtain a more comprehensive comparison between theory and experiment, we have carried out photoelectron diffraction calculations using a large 79-atom five-layer cluster. Multiple scattering effects were included by utilizing a program developed by Kaduwela *et al.* [91, 93, 97]. Photoemission spectra were calculated plac-

ing the emitter in each layer, and then averaging over the layers. Appropriate electron attenuation and angular broadening (over a cone of $\pm 5°$) were also included, and the resulting intensity and asymmetry contours are shown in Fig. 6.4. The theoretical findings are seen to be in excellent agreement with experiment, with three prominent forward scattering peaks apparent in the intensity contours, and a corresponding chessboard pattern centered about each of these peaks in the asymmetry contours. Note in particular that this more realistic calculation moves the maxima and minima in the chessboard pattern closer to the $< 001 >$ direction, thereby improving agreement with experiment in Fig. 6.3(b) as compared to the two-atom single-scattering calculation of Fig. 6.3(c). This also makes it clear that the combined effects of s, d interference and diffraction can move the peaks in intensity (e.g., for $< 012 >$) and the zero of the asymmetry (for all three low-index directions) away from a given low-index direction. More quantitative studies of these effects would be of interest in the future.

In summary, the magnetic dichroism in core-level photoelectron angular distributions excited by a standard laboratory x-ray source in the keV range exhibits around each low-index forward scattering peak an antisymmetry in emission angle and an antisymmetry with binding energy which combine to yield a characteristic chessboard pattern. This pattern is furthermore found to be correctly predicted using photoelectron diffraction theory, and can be understood more fully via a simple analytical model. These results thus not only permit better understanding the origins of linear and unpolarized magnetic dichroism in photoelectron angular distributions, but also suggest future combined structural and magnetic studies by photoelectron diffraction using widely available standard laboratory x-ray sources. The latter is particularly attractive since the higher x-ray photoelectron energies involved also lead to a dominance of forward scattering that simplifies the analysis significantly.

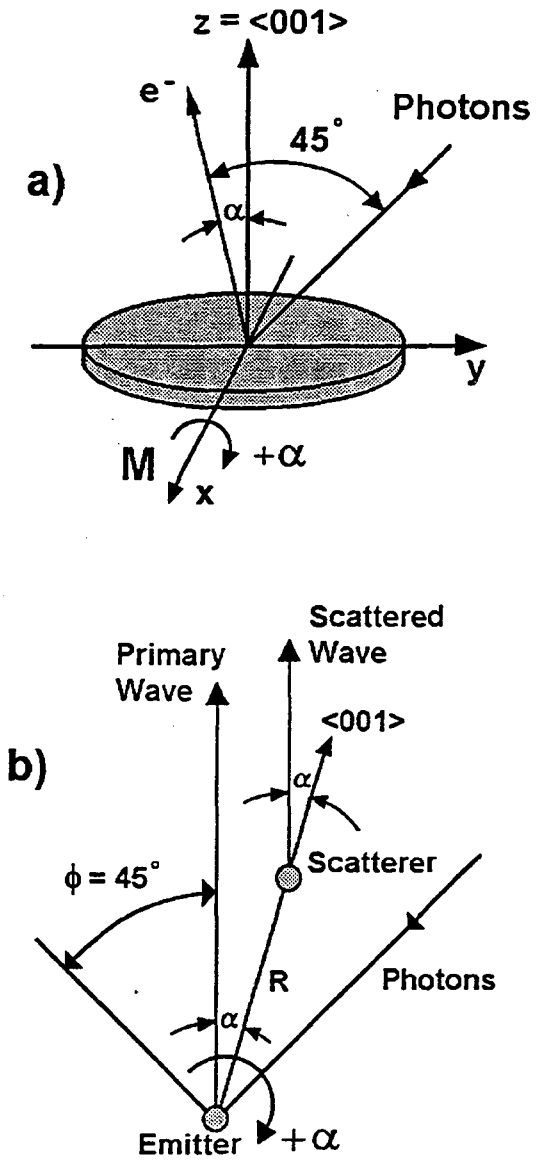

Figure 6.1: Photoemission and scattering geometry. (a) The photoemission geometry: Mg $K\alpha$ radiation impinges on the sample in the yz plane at an angle of 45° with respect to the photoelectron collection direction. The sample magnetization is switched between the $+x$ and $-x$ directions to obtain the dichroism. The sample can be rotated about the x axis to vary the angle α, which equals zero for emission normal to the surface. (b) The emission and scattering geometry, with the angles α and ϕ both defined about the magnetization or x axis perpendicular to the plane of the figure.

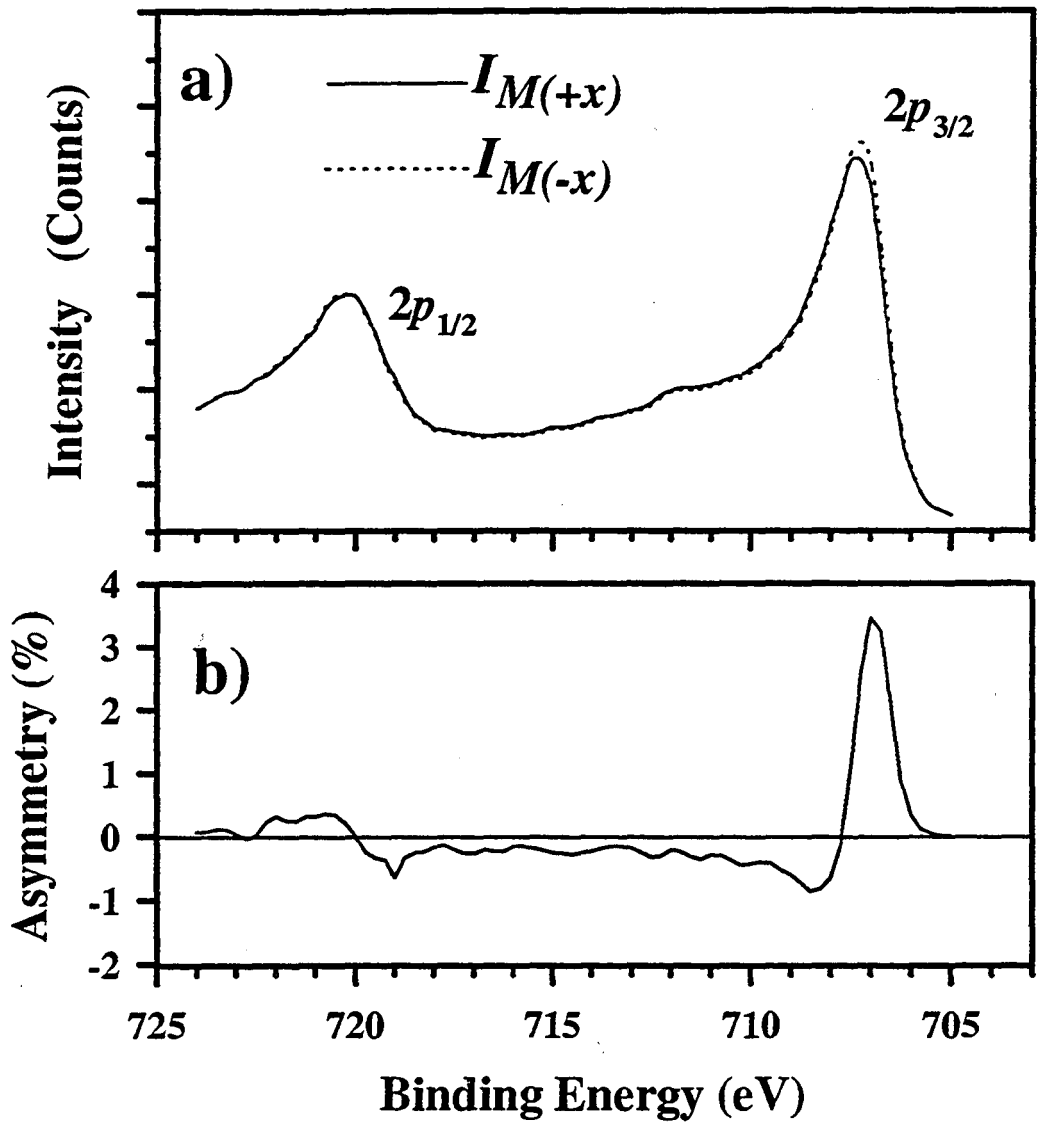

Figure 6.2: (a) Fe $2p$ photoemission spectra for 10 ML Fe/Ag(100) with emission deviating by $\alpha = -2°$ from normal. Solid and dashed lines show spectra for magnetization directions along $+x$ and $-x$, respectively. The small structure at 711-712 eV binding energy is due to the Mg $K\alpha_{3,4}$ satellite x-rays. (b) Dichroic intensity asymmetry when switching the magnetization direction from $-x$ to $+x$, as defined in the text.

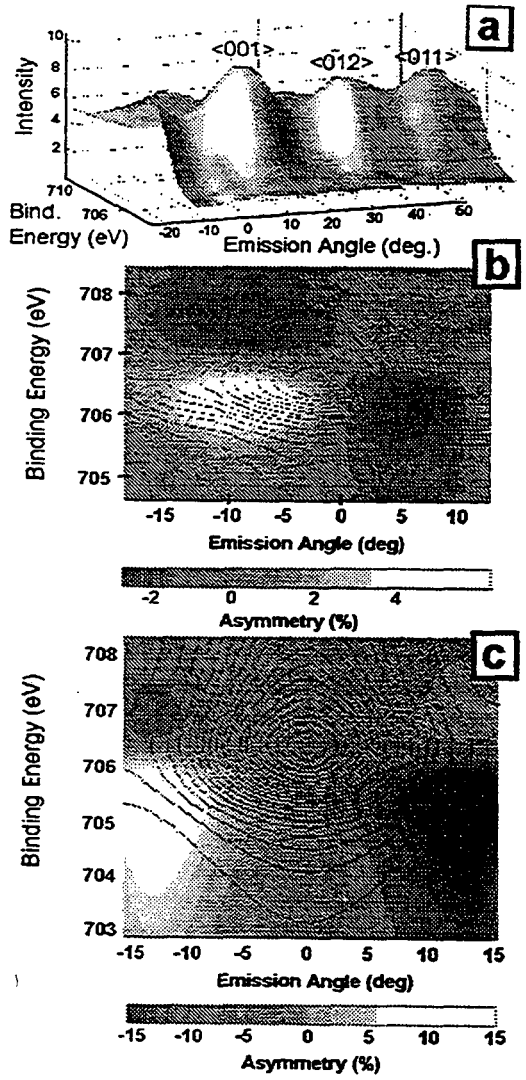

Figure 6.3: (a) Fe $2p_{3/2}$ photoelectron intensity as a function of the emission angle (α) and binding energy (E_b). The height of the surface above the (α, E_b) plane represents the photoemission intensity, with the intensity surface further grey shaded corresponding to the MUDAD asymmetry. (b) Intensity and dichroic asymmetry results for Fe $2p_{3/2}$ around the $< 001 >$ photoelectron diffraction maximum, shown as a contour plot of the intensity (dashed lines) overlaid with a grey-scale contour map of the MUDAD asymmetry. (c) Theoretical simulation corresponding to (b), calculated for a two-atom Fe cluster using single-scattering photoelectron diffraction theory, and assuming a uniform exchange splitting of 0.30 eV between the 4 m_j sublevels of Fe $2p_{3/2}$.

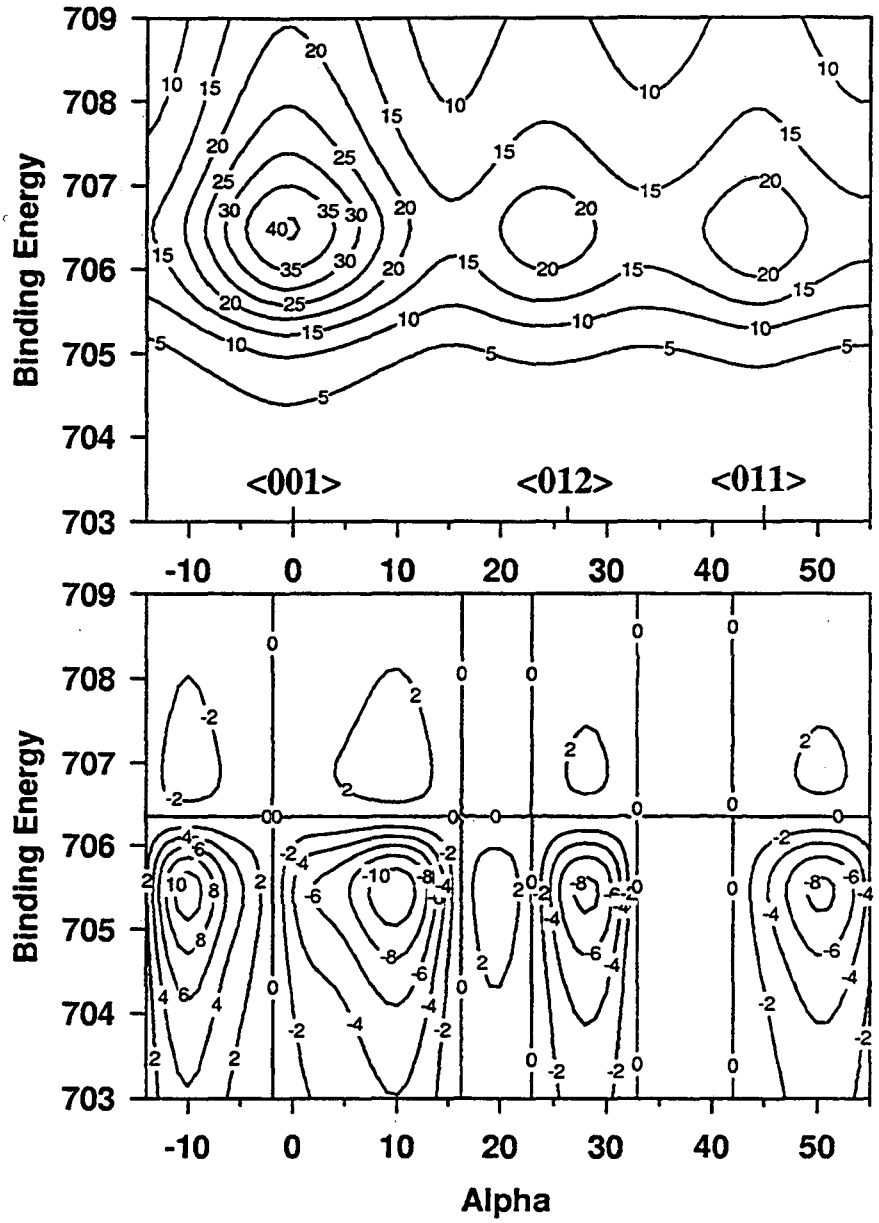

Figure 6.4: Intensity (top panel) and asymmetry (bottom panel) contour lines for Fe $2p_{3/2}$, calculated using a 79-atom cluster, and with multiple-scattering included. The intensity contours are labelled in arbitrary units; the asymmetry contours are in %. The three forward-scattering peaks in the intensity contours and the corresponding chessboard pattern in the asymmetry contours are clearly visible.

Chapter 7

Conclusion

7.1 Thesis Summary

In this thesis we have presented a theoretical investigation of core-level photoemission from ferromagnetic Fe and Ni. We have explicitly considered the spin-orbit and exchange interactions, and included the most general photon polarization within the electric dipole approximation. The resulting formalism allows the calculation of angle- and spin-resolved photoemission spectra. We have compared our theoretical spectra with numerous experimental results, and the favorable agreement indicates that the theory of photoemission from such systems is sufficiently well advanced to understand the spectra at the quantitative level.

In Chapter 2 we treated the ferromagnetism in a phenomenological way; the effect of the spin-polarized valence band was to introduce an exchange splitting between the different m_j sublevels. This approach is expected to work well for systems with weak many-body interactions. We applied our phenomenological model to the case of Fe, and found good agreement with experiment in both the spin polarization and the magnetic dichroism. There was, however, experimental evidence of mixing between the levels and spin-dependent lineshapes. These effects were not accounted for in a natural way by our model. We have argued that the spin-dependent lineshapes are indicative of weak satellite structures.

In Chapter 3 we introduced a much more sophisticated model which treats many-body interactions and extra-atomic screening effects in a realistic way. The model was

applied to the case of photoemission from the Ni $2p$ core level, for which the spin-orbit interaction is significantly larger than the core-valence exchange interaction, and the resulting spectra were in excellent agreement with experiment. We also analyzed the nature of the final state, and assigned physical meaning to the various peaks in the spectrum. We showed that the satellite intensity depends sensitively on the energetic separation between the main line peak and the satellite position. We also showed that this effect explains the spin polarization of the spectrum. As an appendix to this chapter, we detailed the group-theoretical formulation employed in the construction of our symmetrized basis states. This construction, though laborious, ultimately saves three orders of magnitude in computational effort, thereby making the problem tractable.

In Chapter 4 we used the model to investigate the spin polarization and magnetic circular dichroism of the Ni $3p$ core level, for which the spin-orbit and exchange interactions are comparable. Again, the theoretical results were in very good agreement with experiment. We provided physical interpretation of the various spectral features, and also presented a simple 2x2 model that explained the satellite intensity and transfer of spectral weight in a physically intuitive way.

In Chapter 5 we considered the case of magnetic dichroism with linear-polarized excitation. We presented recent experimental data which constitute the best dichroism data presently available for Ni $3p$, and obtained very good agreement using our theoretical model. This case is important because it relates to a current controversy on the surface orbital magnetic moment of Ni. We argued that the magnetic dichroism data do not support the existence of an enhanced moment.

In Chapter 6 we examined the effect of photoelectron diffraction on magnetic dichroism with unpolarized light. We discussed recent experimental results that demonstrate the fundamental importance of photoelectron diffraction in the analysis of such data. We also presented theoretical spectra based on a finite-cluster multiple-scattering calcu-

lation, and these results were found to compare very favorably with experiment. Finally, we provided an intuitive physical argument that correctly explained the underlying effect.

7.2 Prospects for Future Work

Presently, the field of core-level photoemission is very active, and finds itself in the fortunate position of having its theoretical and experimental communities at roughly the same level. New experimental discoveries are constantly leading to new theories, and these theories are in turn motivating experimental work. All of the experimental spectra which have been presented in this thesis are either pending publication, or have been published only within the last three years.

While we have demonstrated that the theory of core photoemission is sufficiently well advanced to explain experiment at the quantitative level, several interesting problems stand out for future theoretical work. For instance, in this thesis we applied a phenomenological one-electron model to describe photoemission from Fe, but used a more rigorous small-cluster many-body scheme to treat the case of Ni. The connection between the two is ambiguous. In the limit of a large cluster, of course, the many-body approach must converge to the correct result. However, the calculation quickly becomes intractable with increasing cluster size. A two-atom cluster, with periodic boundary conditions, will generate the full Fe *bcc* lattice. Even with such a small cluster, however, the problem is formidable due to the large number of holes in the valence band. Nevertheless, it would be fascinating to calculate the photoemission spectrum of Fe within a many-body small-cluster model. Such an analysis would certainly provide important insights into the physical nature of the screening process and answer questions regarding the existence of satellite structures in Fe.

A more comprehensive treatment of final-state effects is another area that appears

promising for future work. Final-state effects may be divided into two categories:

(1) Photoelectron diffraction. This final-state effect results from the outgoing photoelectron scattering off the lattice and interfering with the primary wave, thereby producing intensity modulations in angle and/or energy.

(2) Many-body effects. This type of final-state effect results from the electron response to the sudden creation of a core hole. The excitations that arise from this include Doniach-Sunjic type electron-hole pairs, as well as satellite structures.

Up until now, no theoretical work has incorporated both effects into the same calculation; i.e., either the diffraction effects are calculated accurately within a one-electron theory, or the many-body effects are calculated accurately while the photoelectron diffraction effects are neglected. However, a combination of the two is in principle relatively simple. The calculation of the spectra in the many-body theory requires the matrix elements of the dipole operator, which is a one-electron operator. Typically, only the primary wave is considered when calculating these matrix elements within a many-body approach. However, it is a straighforward matter to utilize the amplitudes from diffraction calculations to construct the matrix elements for the dipole operator. These matrix elements could in turn be used as input into the many-body calculation. An interesting first case to consider for such a calculation would be the Ni $3p$ MCD spectrum. It was argued by van der Laan that the large experimentally observed dichroism was evidence of a strongly enhanced surface orbital magnetic moment. The improved calculation proposed here would test whether this large dichroism were in fact due to photoelectron diffraction effects.

Appendix A

Group Theory: Symmetrization of Basis Functions

Our model consists of a tetrahedral cluster of four Ni atoms, with periodic boundary conditions imposed to generate the full *fcc* lattice. Each atom in the crystal can be labeled by an index 1-4 – as shown in Fig. A.1(a) – and is surrounded by twelve nearest neighbors of a different index.

As our basis states, we use five d-orbitals per site for the valence electrons, and three p-orbitals for the core electrons on the emitting site. We simulate the electronic structure of Ni in the ground state by placing two d-holes on the four-atom cluster. The spectral weight of a line is determined by the projection of the $N-1$ many-body final state onto the N-electron ground state (excluding the orbital from which photoemission occurs). Calculation of the photoemission spectrum therefore requires knowledge of the ground-state wavefunction as well as all eigenstates of the system upon the introduction of a core hole. The Hamiltonian considered here includes same-site hole-hole Coulomb repulsion, valence-band hopping, and spin-orbit interaction in the core level (but not the valence states).

With five d-orbitals per site, there are a total of 20 spatial orbitals. Therefore, including spin, one valence hole can occupy one of 40 states, and a second hole can occupy one of the remaining 39 states. The number of many-body basis states to describe the initial-state manifold is therefore 40x39/2! = 780. When a core hole is introduced, the number of many-body states increases to 780x6 = 4680. It is quite a formidable task to diagonalize and manipulate such large matrices–even with the most powerful computers. By using group theory to fully exploit the symmetries, however, the computational effort

can be greatly reduced. Furthermore, the classification of symmetries often gives insights into the underlying structure of a problem. Consequently, it is well worth the time and effort in symmetrizing the basis functions.

If the origin is chosen to coincide with one of the atoms – say atom 1 – then it may be readily verified that the system has point-group symmtery O, i.e., the set of all proper rotations that map a cube onto itself. These 24 rotations are shown in Fig. A.1(b) and consist of the following: the identity operation E, eight rotations of $\pm 120°$ about the corners of the cube (a, b, c, d), six rotations of 180° about the midpoints of the edges (e, f, g, h, i, j), six rotations of $\pm 90°$ about the centers of the square faces (x, y, z), and three rotations of 180°, again about the centers of the square faces. The character table for point-group O is presented in Table A.1. Functions transform according to the first five irreducible representations. The last three – Γ_6, Γ_7, and Γ_8 – are the so-called double-group representations, and are necessary for describing particles with half-integer spin. Such objects do not transform into themselves upon a rotation of 2π, but rather undergo a sign change. For every operation R in the ordinary group, there is an associated operation $\bar{R}$ in the double group, whose action corresponds to R followed by rotation of 2π. As we shall see, the double-group representations are not necessary for describing the ground state. This is a consequence of the absence of spin-orbit coupling in the valence band, which permits the spin part of the wavefunction to be treated completely independently from the orbital part. Upon introduction of a core hole with strong spin-orbit interaction, it becomes essential of course to use the double-group description.

The d-orbitals form a basis for a reducible representation of the point-group O, and are given by:

$$
\begin{aligned}
f_1 &= 3z^2 - r^2 \quad (e_g) \\
f_2 &= \sqrt{3}(x^2 - y^2) \quad (e_g) \\
f_3 &= yz \quad (t_{2g}) \\
f_4 &= xz \quad (t_{2g}) \\
f_5 &= xy \quad (t_{2g}) \, .
\end{aligned}
\tag{A.1}
$$

The first two functions transform according to E (e_g), and the last three according to T_2 (t_{2g}).

The 20 one-particle basis functions can be written in the localized basis as $f_i(j)$, where $i = 1, 5$ defines the d-orbital and $j = 1, 4$ gives the site index. These functions also form a basis for a reducible representation of the point-group O, whose decomposition can be uniquely determined by [62]:

$$
a(n) = \frac{1}{h} \sum_k N_k \chi^{(n)}(C_k)^* \chi(C_k) \, . \tag{A.2}
$$

Here $a(n)$ is the number of times the nth irreducible representation appears ($n = A_1, A_2, E, etc.$), h is the number of elements in the group, N_k is the number of elements in the kth class, $\chi^{(n)}(C_k)$ is the character of representation n and class k, and $\chi(C_k)$ is the trace of the basis functions under the action of an operator in class k.

The traces, $\chi(C_k)$, are determined through the transformation of the basis functions. In this work we adopt the active viewpoint. The transformation of sites 1-4 and coordinates x, y, z under the action of the point-group O is given in Table A.2, and the transformation of the d-orbitals is presented in Table A.3. The traces can be determined by inspection. For instance, given a rotation C_3 (class 5), $f_1 \rightarrow -1/2(f_1 \pm \sqrt{3} f_2)$ and $f_2 \rightarrow -1/2(f_2 \pm \sqrt{3} f_1)$. Therefore, f_1 and f_2 each contribute -1/2 to the trace, for a total of -1. The other basis functions, f_3, f_4, and f_5 do not contribute to the trace;

e.g., f_3 always transforms into f_4 or f_5, but never into itself. Only sites that remain invariant can contribute to the trace. From Table A.2 we see that only site 1 remains invariant under a rotation C_3, so that $\chi(C_3) = -1$. The other traces can be determined similarly: $\chi(E) = 20$, $\chi(C_4^2) = 4$, $\chi(C_4) = -2$, and $\chi(C_2) = 2$. Therefore, from Eq. A.2 the irreducible representations appear as

$$
\begin{aligned}
a(A_1) &= \frac{1}{24}\Big[(1)(1)(20)+(3)(1)(4)+(6)(1)(-2)+(6)(1)(2)+(8)(1)(-1)\Big] = 1 \\
a(A_2) &= \frac{1}{24}\Big[(1)(1)(20)+(3)(1)(4)+(6)(-1)(-2)+(6)(-1)(2)+(8)(1)(-1)\Big] = 1 \\
a(E) &= \frac{1}{24}\Big[(1)(2)(20)+(3)(2)(4)+(6)(0)(-2)+(6)(0)(2)+(8)(-1)(-1)\Big] = 3 \\
a(T_1) &= \frac{1}{24}\Big[(1)(3)(20)+(3)(-1)(4)+(6)(1)(-2)+(6)(-1)(2)+(8)(0)(-1)\Big] = 1 \\
a(T_2) &= \frac{1}{24}\Big[(1)(3)(20)+(3)(-1)(4)+(6)(-1)(-2)+(6)(1)(2)+(8)(0)(-1)\Big] = 3,
\end{aligned}
\tag{A.3}
$$

leading to a decomposition

$$A_1 \oplus A_2 \oplus 3E \oplus T_1 \oplus 3T_2 \ . \tag{A.4}$$

Thus, group theory predicts that one valence electron in this system will split into nine energy levels – three of which are two-fold degenerate and four of which are three-fold degenerate. Any Hamiltonian possessing such symmetry should lead to the above degeneracies. However, if we use a tight-binding Hamiltonian and diagonalize the resulting matrix, we find that the spectrum does not split into nine energy levels, bit rather only six. These "accidental" degeneracies are a consequence of not considering

other "hidden" symmetries. In addition to the 24 rotational symmetries, the system also possesses four translational symmetries: the identity, and the three translations that map site 1 into sites 2-4. Therefore, the full space group contains 96 symmetry operations. The character table has been determined by Reich [98], and is presented in Table A.4. In order to obtain the decomposition, we must determine the traces of the basis functions under each class of operations. The traces of classes 1-5 are the same as previously determined. A characteristic element of class 6 is $\{E|\tau\}$, i.e., a simple translation. Under a simple translation, all sites are interchanged, and so the trace is zero. It is easy to verify that the traces for each class 6-10 are also zero. Therefore, Eq.(A.2) yields the decomposition

$$\Gamma_{12} \oplus \Gamma'_{25} \oplus X_1 \oplus X_2 \oplus X_3 \oplus X_5. \tag{A.5}$$

Thus, by considering the larger group of symmetry operations, we confirm that the spectrum should indeed split into six energy levels. Furthermore, the group-theoretical approach leads to basis functions of well-defined Brillouin-zone symmetry, which can therefore be directly related to band-structure calculations. A tight-binding approach invariably requires the use of adjustable parameters, with a consequent loss of theoretical footing.

The space-group to point-group compatibility relations are given in Table A.5, and it can be verified that the decompostions of Eq. (A.4) and Eq. (A.5) are indeed equivalent. In the point-group decomposition, some of the irreducible representations occur more than once. Therefore, matrix diagonalization is required to obtain the eigenstates. In the space-group decomposition, on the other hand, each irreducible representation occurs only once, and therefore these basis states must also be eigenfunctions of the one-electron Hamiltonian.

The basis functions can now be symmetrized by applying the complete projection

operators [62], which project out of any state only that part which transforms according to a given row of a given irreducible representation. We are now faced with the following question: *which set of projection operators (i.e., the space group or the point group) are we to use?*

Ultimately, we need to couple the valence holes to the core hole, which breaks translational symmetry. Therefore, all valence states must be identified by a point-group symmetry. However, if we apply the point-group projection operators directly to the basis states, then states of different Brillouin-zone symmetry will be mixed. The solution is to first apply the space-group projection operators, thereby obtaining basis states of well-defined Brillouin-zone symmetry. The point-group projection operators can then be applied to these symmetrized basis functions. The resulting states, presented in Table A.6, now have well-defined space-group *and* point-group symmetries.

With the *one-particle* valence states now fully symmetrized, we turn to the question of symmetrizing the *many-body* basis functions. For this, we must know how to couple basis states of definite symmetry to obtain coupled basis states of another definite symmetry. This task can be accomplished by means of the point-group coupling coefficients [99], which may be regarded as "generalized" Clebsch-Gordan coefficients; just as the Clebsch-Gordan coefficients give the appropriate linear combinations of $|l, m_l>$ and $|l', m_l'>$ required to form new basis states for $l \otimes l'$, the coupling coefficients give the appropriate linear combinations of two point-group symmetries required to form new states of definite point-group symmetry.

As an example, consider the coupling of two sets of orbital wavefunctions, both of symmetry E. To distinguish these, we label them by E^α and E^β, although we also allow for the possibility that $\alpha = \beta$. The direct product is given by:

$$E^\alpha \otimes E^\beta = A_1 \oplus A_2 \oplus E \ . \tag{A.6}$$

Let e_1^α (e_1^β) and e_2^α (e_2^β) be functions transforming according to the first and second rows of E^α (E^β), respectively. Let a_1, a_2, e_1 and e_2 be functions transforming according to the new representations. The coupling coefficients [99] tell us that these states are given by:

$$\begin{aligned} a_1 &= \sqrt{1/2}[e_1^\alpha e_1^\beta + e_2^\alpha e_2^\beta] \\ a_2 &= \sqrt{1/2}[e_2^\alpha e_1^\beta - e_1^\alpha e_2^\beta] \\ e_1 &= \sqrt{1/2}[-e_1^\alpha e_1^\beta + e_2^\alpha e_2^\beta] \\ e_2 &= \sqrt{1/2}[e_2^\alpha e_1^\beta + e_1^\alpha e_2^\beta] \,. \end{aligned} \tag{A.7}$$

As they stand, these coupled wavefunctions are neither symmetric nor antisymmetric. The many-body wavefunction, including spin, must of course be antisymmetric with respect to particle exchange. If $\alpha \neq \beta$, then the above functions can be either symmetrized or antisymmetrized, and then coupled to singlet or triplet spinnors respectively, thereby yielding antisymmetric states with respect to particle exchange. If $\alpha = \beta$, however, then a_2 is necessarily antisymmetric and must be coupled to a spin triplet, while the other three are necessarily symmetric and so must be coupled to a spin singlet. In other words, including spin

$$^2E^\alpha \otimes {}^2E^\alpha = {}^1A_1 \oplus {}^3A_2 \oplus {}^1E \tag{A.8}$$

$$^2E^\alpha \otimes {}^2E^\beta = {}^1A_1 \oplus {}^1A_2 \oplus {}^1E \oplus {}^3A_1 \oplus {}^3A_2 \oplus {}^3E \quad (\alpha \neq \beta), \tag{A.9}$$

where the left superscript refers to the $2s+1$ spin multiplicity.

Every orbital symmetry in Eq. (A.4) must be coupled to every other orbital symmetry to form the two-hole symmetrized orbital basis states. These states are then coupled to the appropriate spinnor, as in the above example. In this way, the 780 many-body wavefunctions in the initial-state manifold are systematically generated, and decompose

with the following point-group symmetries:

$$15\ {}^1A_1 \oplus 7\ {}^1A_2 \oplus 22\ {}^1E \oplus 22\ {}^1T_1 \oplus 26\ {}^1T_2 \oplus \tag{A.10}$$
$$6\ {}^3A_1 \oplus 10\ {}^3A_2 \oplus 15\ {}^3E \oplus 26\ {}^3T_1 \oplus 22\ {}^3T_2\ .$$

The above decomposition is perfectly adequate for describing valence states with no spin-orbit coupling. However, these states must eventually be coupled to the core hole, for which spin-orbit cannot be ignored. Therefore, the spin and orbital parts of Eq. (A.10) must be appropriately coupled. A single spin transforms according to the double-group representation Γ_6. Therefore, two coupled spins transform according to

$$\Gamma_6 \otimes \Gamma_6 = A_1 \oplus T_1, \tag{A.11}$$

with A_1 being the spin singlet, and T_1 being the spin triplet. The coupled decomposition is determined by the direct product. For example,

$${}^3E \rightarrow T_1 \otimes E = T_1 \oplus T_2\ . \tag{A.12}$$

The decomposition of the fully-coupled many-body basis states in the initial-state manifold is therefore given by:

$$41A_1 \oplus 29A_2 \oplus 70E \oplus 91T_1 \oplus 99T_2\ . \tag{A.13}$$

Assuming (correctly) that X_5 is the highest-energy Bloch state, the many-body ground state can be determined by inspection. The one-hole ground state is formed by placing the hole in any of the six X_5 Bloch states. In general, however, putting *two* holes in X_5 Bloch states will lead to charge fluctuations that place both holes on the same site. The Coulomb interaction then mixes Bloch states of different symmetry in a complicated way, and so the ground-state wavefunction can only be determined numerically. However, for the problem at hand, it is fortunately possible to place *both*

holes in states of X_5 symmetry with zero probability of having the holes on the same site. The ground state can therefore be written analytically:

$$\begin{aligned} |GS_1> &= c^\dagger(g_9)c^\dagger(g_{18})|0> \\ |GS_2> &= c^\dagger(g_{10})c^\dagger(g_{19})|0> \\ |GS_3> &= c^\dagger(g_{11})c^\dagger(g_{20})|0> \ . \end{aligned} \tag{A.14}$$

With the valence states now fully symmetrized, we may couple them to the core wavefunction. A p-electron has orbital symmetry T_1 and spin symmetry Γ_6. Therefore, the core states decompose as

$$T_1 \otimes \Gamma_6 = \Gamma_6 \oplus \Gamma_8 \ . \tag{A.15}$$

The $j = 1/2$ level transforms according to Γ_6, and $j = 3/2$ has symmetry Γ_8.

Using the coupling coefficients, the $j = 1/2$ and $j = 3/2$ core levels can be coupled to the 780 basis states in Eq.(A.13), yielding the 4680 fully symmetrized many-body basis functions:

$$392\Gamma_6 \oplus 388\Gamma_7 \oplus 780\Gamma_8 \ . \tag{A.16}$$

By symmetrizing the basis functions in this systematic way, the Hamiltonian matrices for the different rows of a given irreducible representation are identical. Therefore, rather than diagonalize a single matrix of dimension 4680, we can obtain all the eigenstates by diagonalizing only three matrices of dimension 392, 388, and 780. Furthermore, it turns out that the spectra obtained by considering only Γ_6 and Γ_7 symmetries are *visually indistinguishable* from those obtained by including Γ_8, for all cases examined. This fortuitous result implies that $\Gamma_6 \oplus \Gamma_7$ spans a large enough portion of the Hilbert space to accurately describe all of the eigenstates, and so the spectra can be determined by diagonalizing only these two matrices. Assuming that diagonalization time scales

as $\sim n^3$, the group-theoretical approach therefore saves approximately *three orders of magnitude* in computational time. This makes possible efficient sampling in parameter space. Also, because the ground state (Eq. (A)) contains only a few components, only those few components of the final eigenstates need be written out and saved. Using brute force, 4680^2 numbers are required to define the projection of the $N-1$ eigenstates onto the N electron ground state. Using the group theoretical approach, therefore, we save nearly *four orders of magnitude* in hard disk space.

Table A.1: Point-group character table, Group O.

Class ID:	1	2	3	4	5	6	7	8
Elements:	1	3/3	6	6/6	8	1	8	6
Rotation:	E	$C_4^2/\bar{C}_4{}^2$	C_4	$C_2/\bar{C}_2$	C_3	$\bar{E}$	$\bar{C}_3$	$\bar{C}_4$
A_1	1	1	1	1	1	1	1	1
A_2	1	1	-1	-1	1	1	1	-1
E	2	2	0	0	-1	2	-1	0
T_1	3	-1	1	-1	0	3	0	1
T_2	3	-1	-1	1	0	3	0	-1
Γ_6	2	0	$\sqrt{2}$	0	1	-2	-1	$-\sqrt{2}$
Γ_7	2	0	$-\sqrt{2}$	0	1	-2	-1	$\sqrt{2}$
Γ_8	4	0	0	0	-1	-4	1	0

Table A.2: Transformation of sites 1-4 and coordinates x, y, z, point-group O.

Rotation	Site 1	Site 2	Site 3	Site 4	x	y	z
E	1	2	3	4	x	y	z
C_{3a}	1	4	2	3	y	z	x
C_{3b}	1	3	4	2	$-z$	$-x$	y
C_{3c}	1	3	4	2	z	$-x$	$-y$
C_{3d}	1	4	2	3	y	$-z$	$-x$
C_{3a}^{-1}	1	3	4	2	z	x	y
C_{3b}^{-1}	1	4	2	3	$-y$	z	$-x$
C_{3c}^{-1}	1	4	2	3	$-y$	$-z$	x
C_{3d}^{-1}	1	3	4	2	$-z$	x	$-y$
C_{4x}	1	3	2	4	x	z	$-y$
C_{4y}	1	4	3	2	$-z$	y	x
C_{4z}	1	2	4	3	y	$-x$	z
C_{4x}^{-1}	1	3	2	4	x	$-z$	y
C_{4y}^{-1}	1	4	3	2	z	y	$-x$
C_{4z}^{-1}	1	2	4	3	$-y$	x	z
C_{4x}^{2}	1	2	3	4	x	$-y$	$-z$
C_{4y}^{2}	1	2	3	4	$-x$	y	$-z$
C_{4z}^{2}	1	2	3	4	$-x$	$-y$	z
C_{2e}	1	2	4	3	y	x	$-z$
C_{2f}	1	2	4	3	$-y$	$-x$	$-z$
C_{2g}	1	3	2	4	$-x$	z	y
C_{2h}	1	3	2	4	$-x$	$-z$	$-y$
C_{2i}	1	4	3	2	z	$-y$	x
C_{2j}	1	4	3	2	$-z$	$-y$	$-x$

Table A.3: Transformation of basis functions under the action of point group O.

Rotation	f_1	f_2	f_3	f_4	f_5
E	f_1	f_2	f_3	f_4	f_5
C_{3a}	$1/2(-f_1+\sqrt{3}f_2)$	$1/2(-f_2-\sqrt{3}f_1)$	f_4	f_5	f_3
C_{3b}	$1/2(-f_1-\sqrt{3}f_2)$	$1/2(-f_2+\sqrt{3}f_1)$	$-f_5$	$-f_3$	f_4
C_{3c}	$1/2(-f_1-\sqrt{3}f_2)$	$1/2(-f_2+\sqrt{3}f_1)$	f_5	$-f_3$	$-f_4$
C_{3d}	$1/2(-f_1+\sqrt{3}f_2)$	$1/2(-f_2-\sqrt{3}f_1)$	f_4	$-f_5$	$-f_3$
C_{3a}^{-1}	$1/2(-f_1-\sqrt{3}f_2)$	$1/2(-f_2+\sqrt{3}f_1)$	f_5	f_3	f_4
C_{3b}^{-1}	$1/2(-f_1+\sqrt{3}f_2)$	$1/2(-f_2-\sqrt{3}f_1)$	$-f_4$	f_5	$-f_3$
C_{3c}^{-1}	$1/2(-f_1+\sqrt{3}f_2)$	$1/2(-f_2-\sqrt{3}f_1)$	$-f_4$	$-f_5$	f_3
C_{3d}^{-1}	$1/2(-f_1-\sqrt{3}f_2)$	$1/2(-f_2+\sqrt{3}f_1)$	$-f_5$	f_3	$-f_4$
C_{4x}	$1/2(-f_1-\sqrt{3}f_2)$	$1/2(f_2-\sqrt{3}f_1)$	$-f_3$	$-f_5$	f_4
C_{4y}	$1/2(-f_1+\sqrt{3}f_2)$	$1/2(f_2+\sqrt{3}f_1)$	f_5	$-f_4$	$-f_3$
C_{4z}	f_1	$-f_2$	$-f_4$	f_3	$-f_5$
C_{4x}^{-1}	$1/2(-f_1-\sqrt{3}f_2)$	$1/2(f_2-\sqrt{3}f_1)$	$-f_3$	f_5	$-f_4$
C_{4y}^{-1}	$1/2(-f_1+\sqrt{3}f_2)$	$1/2(f_2+\sqrt{3}f_1)$	$-f_5$	$-f_4$	f_3
C_{4z}^{-1}	f_1	$-f_2$	f_4	$-f_3$	$-f_5$
C_{4x}^{2}	f_1	f_2	f_3	$-f_4$	$-f_5$
C_{4y}^{2}	f_1	f_2	$-f_3$	f_4	$-f_5$
C_{4z}^{2}	f_1	f_2	$-f_3$	$-f_4$	f_5
C_{2e}	f_1	$-f_2$	$-f_4$	$-f_3$	f_5
C_{2f}	f_1	$-f_2$	f_4	f_3	f_5
C_{2g}	$1/2(-f_1-\sqrt{3}f_2)$	$1/2(f_2-\sqrt{3}f_1)$	f_3	$-f_5$	$-f_4$
C_{2h}	$1/2(-f_1-\sqrt{3}f_2)$	$1/2(f_2-\sqrt{3}f_1)$	f_3	f_5	f_4
C_{2i}	$1/2(-f_1+\sqrt{3}f_2)$	$1/2(f_2+\sqrt{3}f_1)$	$-f_5$	f_4	$-f_3$
C_{2j}	$1/2(-f_1+\sqrt{3}f_2)$	$1/2(f_2+\sqrt{3}f_1)$	f_5	f_4	f_3

Table A.4: Space-group character table.

Class ID:	1	2	3	4	5	6	7	8	9	10
Elements:	1	3	6/6	6/6	8/24	3	3	6	12	12
Rotation:	E	C_4^2	C_4	C_2	C_3	E	C_4^2	C_4	C_2	C_3
Translation:	0	0	$0/\tau_\perp$	$0/\tau_{\|\|}$	$0/\tau_>$	τ	$\tau_\perp$	$\tau_<$	$\tau_<$	$\tau_<$
Γ_1	1	1	1	1	1	1	1	1	1	1
Γ_2	1	1	-1	-1	1	1	1	1	-1	-1
Γ_{12}	2	2	0	0	-1	2	2	2	0	0
Γ'_{15}	3	-1	1	-1	0	3	-1	-1	1	-1
Γ'_{25}	3	-1	-1	1	0	3	-1	-1	-1	1
X_1	3	3	1	1	0	-1	-1	-1	-1	-1
X_2	3	3	-1	-1	0	-1	-1	-1	1	1
X_3	3	-1	-1	1	0	-1	3	-1	1	-1
X_4	3	-1	1	-1	0	-1	3	-1	-1	1
X_5	6	-2	0	0	0	-2	-2	2	0	0

Table A.5: Compatibility relations.

Γ			X		
Γ_1	$\rightarrow$	A_1	X_1	$\rightarrow$	$A_1 \oplus E$
Γ_2	$\rightarrow$	A_2	X_2	$\rightarrow$	$A_2 \oplus E$
Γ_{12}	$\rightarrow$	E	X_3	$\rightarrow$	T_2
Γ'_{15}	$\rightarrow$	T_1	X_4	$\rightarrow$	T_1
Γ'_{25}	$\rightarrow$	T_2	X_5	$\rightarrow$	$T_1 \oplus T_2$

Table A.6: Fully symmetrized one-electron basis functions. The N_i are the appropriate normalization constants, and $f_i(j)$ corresponds to d-orbital f_i on site j.

Function	Pt. Sym.	Sp. Sym.	Basis State
g_1	A_1	X_1	$N_1[2f_1(2) - f_1(3) - f_1(4) - \sqrt{3}f_2(3) + \sqrt{3}f_2(4)]$
g_2	A_2	X_2	$N_2[\sqrt{3}f_1(3) - \sqrt{3}f_1(4) + 2f_2(2) - f_2(3) - f_2(4)]$
g_3	$E(1)$	Γ_{12}	$N_3[f_1(1) + f_1(2) + f_1(3) + f_1(4)]$
g_4	$E(2)$	Γ_{12}	$N_4[f_2(1) + f_2(2) + f_2(3) + f_2(4)]$
g_5	$E(1)$	X_1	$N_5[3f_1(1) + f_1(2) - 2f_1(3) - 2f_1(4)$
			$+\sqrt{3}f_2(3) - \sqrt{3}f_2(4)]$
g_6	$E(2)$	X_1	$N_6[\sqrt{3}f_1(3) - \sqrt{3}f_1(4) + 3f_2(1) - 3f_2(2)]$
g_7	$E(1)$	X_2	$N_7[3f_1(1) - 3f_1(2) - \sqrt{3}f_2(3) + \sqrt{3}f_2(4)]$
g_8	$E(2)$	X_2	$N_8[-\sqrt{3}f_1(3) + \sqrt{3}f_1(4) + 3f_2(1) + f_2(2)$
			$-2f_2(3) - 2f_2(4)]$
g_9	$T_1(1)$	X_5	$N_9[f_3(2) - f_3(3)]$
g_{10}	$T_1(2)$	X_5	$N_{10}[-f_4(2) + f_4(4)]$
g_{11}	$T_1(3)$	X_5	$N_{11}[f_5(3) - f_5(4)]$
g_{12}	$T_2(1)$	Γ'_{25}	$N_{12}[f_3(1) + f_3(2) + f_3(3) + f_3(4)]$
g_{13}	$T_2(2)$	Γ'_{25}	$N_{13}[f_4(1) + f_4(2) + f_4(3) + f_4(4)]$
g_{14}	$T_2(3)$	Γ'_{25}	$N_{14}[f_5(1) + f_5(2) + f_5(3) + f_5(4)]$
g_{15}	$T_2(1)$	X_3	$N_{15}[f_3(1) - f_3(2) - f_3(3) + f_3(4)]$
g_{16}	$T_2(2)$	X_3	$N_{16}[f_4(1) - f_4(2) + f_4(3) - f_4(4)]$
g_{17}	$T_2(3)$	X_3	$N_{17}[f_5(1) + f_5(2) - f_5(3) - f_5(4)]$
g_{18}	$T_2(1)$	X_5	$N_{18}[f_3(1) - f_3(4)]$
g_{19}	$T_2(2)$	X_5	$N_{19}[f_4(1) - f_4(3)]$
g_{20}	$T_2(3)$	X_5	$N_{20}[f_5(1) - f_5(2)]$

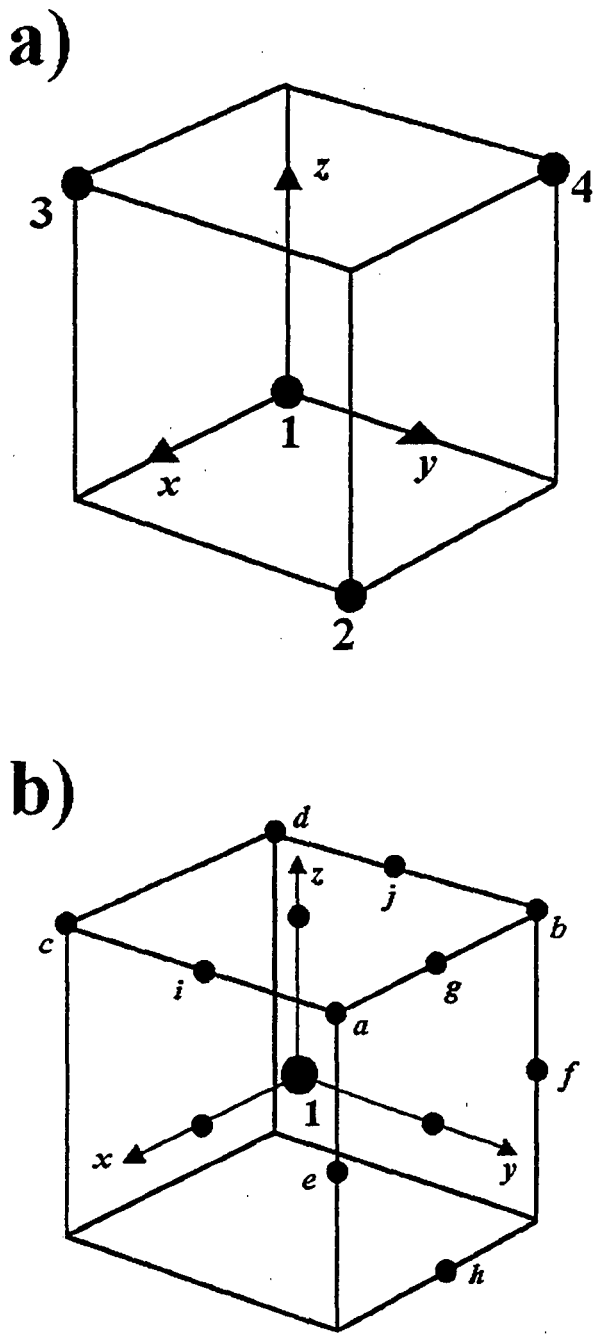

Figure A.1: The model. (a) Tetrahedral cluster of four atoms. Periodic boundary conditions are imposed to generate the full *fcc* lattice. (b) The set of all proper rotations about atom 1 that map the lattice onto itself (point group O).

Bibliography

[1] For a brief history of the development of photoemission, see G. Margaritondo: *Physics Today*, 66 (April 1988).

[2] For a detailed history of photoemission from its beginnings until 1960, see J.G. Jenkin, R.C.G. Leckey, and J. Liesegang, J. Electron Spectr. **12**, 1 (1977).

[3] H. Hertz, Ann. Phys. (Leipzig) **68**, 983 (1887). Translated in H. Hertz, *Electric Waves*, McMillan, London (1900).

[4] J.J. Thomson, Philosophical Magazine, (5), **44**, 293 (1897).

[5] P. Lenard, Wien. Ber. **108**, 1649 (1899); P. Lenard, Ann. Phys. (Leipzig) **2**, 359 (1900); P. Lenard, Ann. Phys. (Leipzig) **8**, 149 (1902).

[6] A. Einstein, Ann. Phys. (Leipzig) **17**, 132 (1905).

[7] R.A. Millikan, Physical Review **7**, 362 (1916).

[8] A. Sommerfeld, Z. Physik **47**, 1 (1928).

[9] For nonzero temperatures, the Fermi-Dirac distribution says that there always exists a finite probability of finding some of the electrons in states above the Fermi level. If these states are sufficiently high in energy (i.e., above the vacuum level), then they will be spontaneously emitted by the metal.

[10] When two conductors are brought into physical contact, the Fermi energies become equal. This results in a "contact potential" between the conductors, which in turn can be related to their work functions.

[11] E. Wigner and J. Bardeen, Physical Review **48**, 84 (1935).

[12] M. de Broglie, J. Phys. 2 (1921) 265.

[13] R.G. Steinhardt and F.J. Serfass, Anal. Chem. **25**, 697 (1953).

[14] K. Siegbahn *et al.*, *ESCA: Atomic, Molecular, and Solid State Structure Studied by Means of Electron Spectroscopy*, Almqvist and Wiksells, Uppsala (1967).

[15] C.S. Fadley, S.B.M Hagstrom, J.M. Hollander, M.P. Klein, and D.A. Shirley, Science **157**, no. 3796, 1579 (1967); C.S. Fadley, S.B.M Hagstrom, M.P. Klein, and D.A. Shirley, J. Chem. Phys. **48**, 3779 (1968).

[16] C.N. Berglund and W.E. Spicer, Phys. Rev. A **136**, 1044 (1964).

[17] C. Guillot, Y. Ballu, Y. Paigne, J. Lecante, K.P. Jain, P. Thiry, R. Pinchaux, Y. Petroff, and L.M. Falicov, Phys. Rev. Lett. **39**, 1632 (1977).

[18] N.V. Smith, Phys. Rev. Lett. **23**, 1452 (1969).

[19] E. Kisker, K. Schroder, W. Gudat, and M. Campagna, Phys. Rev. B **31**, 329 (1985).

[20] C.S. Fadley and D.A. Shirley, Phys. Rev. A **2**, 1109, (1970).

[21] L. Baumgarten, C.M. Schneider, H. Petersen, F. Schafers, and J. Kirschner, Phys. Rev. Lett. **65**, 492 (1990).

[22] Ch. Roth, F.U. Hillebrecht, H.B. Rose, and E. Kisker, Phys. Rev. Lett. **70**, 3479 (1993).

[23] F.U. Hillebrecht and W.D. Herberg, Z. Phys, B **93**, 299 (1994).

[24] F.U. Hillebrecht, R. Jungblut and E. Kisker, Phys. Rev. Lett. **65**, 2450 (1990); R. Jungblut, Ch. Roth, F.U. Hillebrecht and E. Kisker, J. Appl. Phys. **70**, 5923 (1991).

[25] D.G. Van Campen, R.J. Pouliot, and L.E. Klebanoff, Phys. Rev. B **48**, 17533 (1993).

[26] L.E. Klebanoff, D.G. Van Campen, and R.J. Pouliot, Phys. Rev. B **49**, 2047 (1994).

[27] A.K. See and L.E. Klebanoff, Phys. Rev. B **51**, 11002 (1995).

[28] C.S. Fadley, Surface Science Reports 19 (1993) 231-264; C.S. Fadley in *Synchrotron Radiation Research: Advances in Surface Science*, R.Z. Bachrach (Ed.), (Plenum Press, New York, 1993).

[29] L.G. Petersson, S. Kono, N.F.T. Hall, C.S. Fadley, and J.B. Pendry, Phys. Rev. Lett. **42**, 1545 (1979).

[30] A. Fischer, R. Fasel, J. Osterwalder, A. Krozer, and L. Schlapbach, Phys. Rev. Lett. **70**, 1493 (1993).

[31] J.J. Barton, Phys. Rev. Lett. **61**, 1356 (1988).

[32] A. Szöke, in *Short Wavelength Coherent Radiation: Generation and Applications*, D.T. Attwood and J. Bokor (Eds.), AIP Conference Proceedings No. 147 (AIP, New York, 1986).

[33] A.P. Kaduwela, Z. Wang, S. Thevuthasan, M.A. Van Hove, and C.S. Fadley, Phys. Rev. B **50**, 9656 (1994).

[34] A. Fanelsa, R. Schellenberg, F.U. Hillebrecht, E. Kisker, J.G. Menchero, A.P. Kaduwela, C.S. Fadley, and M.A. Van Hove, Phys. Rev. B **54**, 17962 (1996).

[35] See, for instance, E. Merzbacher, *Quantum Mechanics*, (Wiley, New York, 1970).

[36] J.J. Barton and D.A. Shirley, Phys. Rev. B **32**, 1892 (1985); J.J. Barton and D.A. Shirley, Phys. Rev. B **32**, 1906 (1985).

[37] G. van der Laan and B. T. Thole, J. Phys. Condens. Matter **4**, 4181 (1991).

[38] J.G. Menchero, Phys. Rev. Lett. **76**, 3208 (1996).

[39] J.G. Menchero, Phys. Rev. B **55**, 5505 (1997).

[40] H. Ebert, L. Baumgarten, C.M. Schneider, and J. Kirschner, Phys. Rev. B **44**, 4406 (1991).

[41] G. Rossi, F. Sirotti, N.A. Cherepkov, F. Combet Farnoux, and G. Panaccione, Solid State Comm. **90**, 557 (1994).

[42] F.U. Hillebrecht, H.B. Rose, Ch. Roth, and E. Kisker, J. Magn. Magn. Mat. **148**, 49 (1995).

[43] C.M. Schneider, U. Pracht, W. Kuch, A. Chasse, and J. Kirschner, Phys. Rev. B **54**, R15618 (1996).

[44] N.A. Cherepkov and V.V. Kuznetsov, J. Phys. B **22**, L405 (1989).

[45] N.A. Cherepkov, Phys. Rev. B **50** 13813 (1994); J. Phys. Condens. Matter **8**, 4971 (1996).

[46] J.D. Jackson, *Classical Electrodynamics*, (Wiley, New York, 1975).

[47] S.M. Goldberg, C.S. Fadley and S. Kono, J. Electron Spectrosc. **21**, 285 (1981).

[48] Gerrit van der Laan, Phys. Rev. B **51**, 240 (1995).

[49] D. Venus, Phys. Rev. B **49**, 8821 (1994).

[50] D.E. Eastman, F.J. Himpsel, and J.A. Knapp, Phys. Rev. Lett. **40**, 1514 (1978).

[51] A. Liebsch, Phys. Rev. Lett. **43**, 1431 (1979).

[52] L.A. Feldkamp and L.C. Davis, Phys. Rev. B. **22**, 3644 (1980).

[53] R.H. Victora and L.M. Falicov, Phys. Rev. Lett. **55**, 1140 (1985).

[54] S. Hüfner and G.K. Wertheim, Phys. Lett. **51A**, 299 (1975).

[55] A.K. See and L.E. Klebanoff, Phys. Rev. Lett. **74**, 1454 (1995).

[56] C.S. Wang and J. Callaway, Phys. Rev. B **15**, 298 (1977).

[57] N.A. Cherepkov, J. Phys. B **12**, 1279 (1979).

[58] H.B. Rose, F.U. Hillebrecht, E. Kisker, R. Denecke, and L. Ley, J. Magn. Magn. Mat. **148**, 62 (1995).

[59] Ch. Roth, H.B. Rose, F.U. Hillebrecht, and E. Kisker, Solid State Commun. **86**, 647 (1993).

[60] L.M. Falicov, *Recent Progress in Many-Body Theories*, Vol 1, edited by A.J. Kallio, E. Pajanne, and R.F. Bishop, (Plenum, New York, 1988), p. 275.

[61] C. Herring, *Magnetism: A Treatise on Modern Theory and Materials*, edited by G.T. Rado and H. Suhl (Academic, New York, 1966), Vol. 4.

[62] M. Tinkham, *Group Theory and Quantum Mechanics*, (McGraw Hill, New York,1964).

[63] See, for instance, Mitchel Weissbluth, *Atoms and Molecules*, Ch 11-12, (Academic Press, New York, 1978).

[64] G. van der Laan *et al.*, Phys. Rev. B **46**, 9336 (1992).

[65] R.D. Cowan, *The Theory of Atomic Structure and Spectra*, (University of California Press, Berkeley, 1981).

[66] B.T. Thole and G. van der Laan, Phys. Rev. Lett. **67**, 3306 (1991).

[67] T. Jo and G.A. Sawatzky, Phys. Rev. B **43** 8771, (1991).

[68] We emphasize here that, for a general choice of parameters in the Hamiltonian, the spectra derived from Γ_8 symmetry are not *identical* to those derived from $\Gamma_6 + \Gamma_7$ symmetries. Such a result would imply the existence of additional "hidden" symmetries.

[69] S. Doniach and M. Šunjić, J. Phys. C **3**, 285 (1970).

[70] A.K. See and L.E. Klebanoff, Surf. Sci. **341**, 142 (1995).

[71] The $2p_{1/2}$ Lorentzian broadening is slightly larger due to L_2L_3V Coster-Kronig decay mechanisms, which are not possible for $2p_{3/2}$ core holes.

[72] G. Schönhense, A. Eyers, U. Friess, F. Schäfers, and U. Heinzmann, Phys. Rev. Lett. **54**, 547 (1985).

[73] B.T. Thole and G. van der Laan, Phys. Rev. B **49**, 9613 (1994).

[74] A. Tanaka, T. Jo, and G.A. Sawatzky, J. Phys. Soc. Jpn. **61**, 2636 (1992).

[75] G. van der Laan, M.A. Hoyland, M. Surman, C.F.J. Flipse, and B.T. Thole, Phys. Rev. Lett. **69**, 3827 (1992).

[76] Y. Liu, Z. Xu, P.D. Johnson, and G. van der Laan, Phys. Rev. B **52**, R8593 (1995).

[77] K. Starke, A.P. Kaduwela, Y. Liu, P.D. Johnson, M.A. Van Hove, C.S. Fadley, V. Chakarian, E.E. Chaban, G. Meigs, and C.T. Chen, Phys. Rev. B **53**, R10544 (1996).

[78] F.U. Hillebrecht, H.B. Rose, T. Kinoshita, Y.U.Idzerda, G. van der Laan, R. Denecke, and L. Ley, Phys. Rev. Lett. **75**, 2883 (1995).

[79] G. van der Laan, Phys. Rev. **B51**, 240 (1995).

[80] E. Tamura, G.D. Waddill, J.G. Tobin, and P.A. Sterne; Phys. Rev. Lett. **73**, 1533 (1994).

[81] M. Getzlaff, Ch.Ostertag, G.H. Fecher, N. A. Cherepkov, and G. Schönhense; Phys. Rev. Lett.**73**, 3030 (1994).

[82] F. Sirotti, G. Panaccione, and G. Rossi, Phys. Rev. **B52**, R17063 (1995).

[83] M.J. Freiser, IEEE Transactions on Magnetics, vol MAG-4, 152 (1968).

[84] B. T. Thole, P. Carra, F. Sette, and G. van der Laan, Phys. Rev. Lett. **68** , 1943 (1992); P.Carra, B. T. Thole, M. Altarelli, and X. Wang, Phys. Rev. Lett. **70**, 694 (1993).

[85] C.T. Chen, Y. U. Idzerda, H.-J.Lin, N.V. Smith, G. Meigs, E. Chaban, G.H. Ho, E. Pellegrin, and F. Sette; Phys. Rev. Lett. **75**, 152 (1995)

[86] F.U. Hillebrecht, Ch. Roth, H.B. Rose, W.G. Park, E. Kisker, and N.A. Cherepkov; Phys. Rev **B53**, 12182 (1996).

[87] F. U. Hillebrecht, J. C. Fuggle, P.A. Bennet, Z. Zolnierek, Ch. Freiburg, Phys. Rev. **B27**, 2179 (1983); R. Raue, H. Hopster, and R. Clauberg. Phys. Rev. Lett. **50**, 1623 (1983).

[88] O. Eriksson, G. W. Fernando, R. C. Albers, A. M. Boring, Solid State Commun. **78**, 801 (1991).

[89] D. Pescia, M. Stampanoni, G. L. Bona, A. Vaterlaus, R. F. Willis, F. Meier, Phys. Rev. Lett. **58**, 2126 (1987).

[90] J. Vogel and M. Sacchi, Phys. Rev. **B53**, 3409 (1996).

[91] C. Westphal, A.P. Kaduwela, C.S. Fadley, and M.A. Van Hove, Phys. Rev. **B50**, 6203 (1994).

[92] A. Fanelsa, R. Schellenberg, F.U. Hillebrecht, and E. Kisker, Solid State Commun. **96**, 291 (1995).

[93] A.P. Kaduwela, H. Xiao, S. Thevuthasan, C.S. Fadley, and M.A. Van Hove, Phys. Rev. B **52**, 14297 (1995).

[94] G. van der Laan and B.T. Thole, Solid State Commun. **92**, 427 (1994); B.T. Thole and G.van der Laan, Phys. Rev. B **50**, 11474 (1994).

[95] W. Kuch, M.T. Lin, W. Steinhogl, C.M. Schneider, D. Venus, and J. Kirschner, Phys. Rev. B **51**, 609 (1995).

[96] D.J. Friedman and C.S. Fadley, J. Electron Spectrosc. **51**, 689 (1990).

[97] A.P. Kaduwela, D.J. Friedman, and C.S. Fadley, J. Electron Spectrosc. **57**, 223 (1991).

[98] A. Reich and L. M. Falicov, Phys. Rev. B **37**, 5560, (1988).

[99] G. Koster, John Dimmock, Robert G. Wheeler, and Hermann Statz, *Properties of the Thirty-two Point Groups*, (MIT Press, Cambridge, Massachusetts, 1963).

Ernest Orlando Lawrence Berkeley National Laboratory
One Cyclotron Road | Berkeley, California 94720

Prepared for the U.S. Department of Energy under Contract No. DE-AC03-76SF00098